CENTRO DE INVESTIGACIONES
EN OPTICA, A.C.

"OPTICAL THERMAL CHARACTERIZATION OF A HIGH FLUX SOLAR SIMULATOR FOR THE DEVELOPMENT OF SPECTRAL ABSORPTION APPLICATIONS"

Thesis that to obtain the degree of Doctor of Science (optics)

Presents: Leopoldo Martínez-Manuel

Advisor: Dr. Manuel I. Peña-Cruz

Final version including modifications suggested by reviewers

León · Guanajuato · México

April 2021

MANUEL I PEÑA CRUZ

revised
2021-04-26

Abstract

Solar technologies, such as concentrating solar power (CSP) systems, are one of the most promising technologies for covering the future global energy demand, achieving a low-carbon economy and mitigating environmental problems (greenhouse effect). Typically, outdoor solar facilities are implemented for evaluating solar receivers and prototypes, but the intermittent nature of solar radiation and weather constrains are the main challenges in offering stable testing environments. Solar simulators have been identified as key facilities for carrying out high-quality indoor assessments under a controlled lab-scale environment. This PhD thesis is aimed to the optical design and characterization of a high flux solar simulator (HFSS) for researching solar-thermal and thermochemical processes. To do so, a 17.5 kW_e HFSS was developed along with a calorimetric test bench for the assessment of solar-thermal materials. The design of the 7 xenon lamps based solar simulator was numerically analyzed through the Monte Carlo ray-tracing method and characterized with the indirect flux mapping technique, an optical technique that involves the use of a high resolution camera and a diffusely reflective flat target plate. Characterization results showed a total peak flux of up to 1327 ± 58 kW/m^2 having an intercepted radiative power of 5.11 ± 0.22 kW over a flux spot distribution of 120 mm in diameter, and conversion efficiency of 33%. Regarding the calorimetric test bench, its design was based on a flat-plate calorimeter which provides the versatility to replace test samples as interchangeable cartridges. By coupling the test bench with the HFSS, solar-thermal assessments of 4 different commercial solar absorber coatings and a new soot of forest biomass based coating were experimentally evaluated and compared under the same operating conditions. The presented approach for evaluating commercial and new solar-thermal materials provides critical information about their optical-thermal capabilities. Accordingly, the flux acceptance of suitable materials for their usage in solar-based industrial process heating can be effectively determined, and further progress in the improvement of solar-thermal technologies can be accomplished.

Key words: High flux solar simulator; Concentrating solar power; Ray-tracing analysis; Calorimetric test bench; Solar absorber coatings.

Acknowledgements

First of all, I would like to thank the Consejo Nacional de Ciencia y Tecnología (CONACYT) for the financial support granted to carry out this doctoral project, grant number 299966. I also acknowledge the financial support received from Fondo Sectorial CONACYT-SENER-Sustentabilidad Energética through Grant 207450, "Centro Mexicano de Innovación en Energía Solar (CeMIE-Sol)", within strategic project No. 120 "Tecnología solar para obtención de productos con valor agregado mediante procesamiento hidrotermal". Likewise, I acknowledge Centro de Investigaciones en Óptica, A.C. (CIO), for giving me the opportunity to continue my professional career at the highest educational level in the field of optics.

I would like to express my gratitude to my thesis advisor, Dr. Manuel Peña, who more than an advisor, is a good friend; for his infinite patience, advice, and motivation to work in the most professional way possible. Furthermore, I would like to thank my follow up committee that provided me with ideas and quite valuable constructive criticism during these 4 years of doctoral studies: Dr. Carlos Pineda, Dr. Daniel May and Dr. Gonzalo Carrillo. Without your supervision, the development of this doctoral project would not have had the excellent results that were achieved. In addition, I would like to express my gratitude to the Solara Industries company, especially to Miguel Villa. Due to their collaboration, the construction of the solar simulator was carried out in a timely manner while managing to conduct a large number of experiments.

Many thanks to my colleagues and friends both during my period at CIO León and at CIO Aguascalientes, who made my stay at both places more pleasant and full of good experiences. Likewise, I would like to thank the CIO staff who helped me throughout my doctoral studies, all their support, friendship and advice were valuable for the completion of this thesis; Dr. Iván Salgado, Lupita Ibarra, Dra. Nancy Gonzales, Gustavo Acevedo, Juan Sarabia, Maestro Gil, Martha Campos, Eduardo Licurgo, Dr. Sergio, Cristian and Don Sote. As well, I would like to thank my supervisor Dr. Wujun Wang for all his advice and support during my PhD internship at the Royal Institute of technology in Sweden.

Last but not least, I want to give my immense gratitude to my family and closest friends. Many thanks to my sisters-in-law and their respective families who have given me their sincere friendship. Thanks a lot to my parents Elodia Manuel and Pedro Martínez who have always believed in me, encouraging me to continue in difficult moments and enjoying successes with me during my doctoral studies and throughout my life. I also say thanks to my brothers, Rodolfo and Pedro Reynaldo, who have encouraged and advised me, and who have supported me in every single aspect, as much as a noble and disinterested person can do for their brother, thank you very much, you are the bests.

Nomenclature

Acronyms	
BRDF	Bidirectional reflectance distribution function
CCD	Charge-coupled device
CSP	Concentrating solar power
CPC	Compound parabolic collector
HCFL	High concentrating flux level
HFSS	High flux solar simulator
HTF	Heat transfer fluid
LCFL	Low concentrating flux level
LFC	Linear Fresnel collector
MCRT	Monte Carlo ray-tracing
PDC	Parabolic dish collector
PTC	Parabolic trough collector
SPT	Solar power tower
SHIP	Solar heat for industrial processes
SAC	Solar absorber coating
SC	Shutter curtain
SF	Solar furnace
SFB	Soot of forest biomass
SSAC	Selective solar absorber coating

Latin Characters	
A, B, g	Fit parameters of the BRDF equation
a	Semi-major axis of the ellipse
A_{tg}	Flux spot area on the target, m^2
b	Semi-minor axis of the ellipse

$B(\lambda, T)$	Black body spectrum, W/srm^3
c	Middle distance between focal points, mm
c, c_2	First and second Planck's constants, Wm^2, mK
C_{pw}	Specific heat capacity of water, J/kgK
D_{axis}	External cutting distance, mm
e	Eccentricity
f_1	First focal point of the ellipse
f_2	Second focal point of the ellipse
I_{dark}	Dark current
I_{lamp}	Electric current of the lamp, A
I_{max}	Maximum irradiance measured on a point during a nominated time, kW/m^2
I_{min}	Minimum irradiance measured on a point during a nominated time, kW/m^2
l_{cut}	Internal cutting distance, mm
l_{cyl}	Cylinder length, mm
m	Mass flow rate, kg/s
M_{pix}	Maximum grayscale pixel value
N	Number of recorded images
$Pix_{(i,j)}$	Averaged grayscale pixel value
$pix_{i,j}$	Grayscale value from the n^{th} image
$Q_{(i,j)}$	Radiative flux on the target, kW/m^2
$q_{(x,y)}$	Flux measured on the target, kW/m^2
Q_{abs}	Absorbed thermal power, W
Q_{cond}	Conduction losses, W
Q_{conv}	Convection losses, W
Q_{in}	Incident radiative power, W
Q_{loss}	Total heat losses, W

Q_{rad}	Radiation losses, W
Q_{ref}	Reflection losses, W
Q_{sr}	Radiant energy leaving the light source, W
Q_{tg}	Energy reaching the target, W
$\overline{q}$	Mean flux distribution, W/m^2
R	Target radius, mm
R_{in}	Internal radius of the ellipse, mm
r_{cyl}	Cylinder radius, mm
S	Spectral solar irradiance, W/m^2
$S(\lambda)$	Spectral solar terrestrial irradiance, W/m^{2}nm
T_a	Room temperature, °C
T_i	Inlet water temperature, °C
T_o	Outlet water temperature, °C
TR	Total reflectance
T_s	Receiver surface temperature, °C
V_{lamp}	Input voltage of lamp, V

Greek characters	
α	Absorptivity
α_{abs}	Coating absorptivity
α_{ideal}	Ideal absorptivity of 1
α_c	Truncation angle, °
ΔT	Temperature difference in calorimeter, °C
ε	Emissivity
ε_{ideal}	Ideal emissivity of 0
η	Radiative transfer efficiency
η_{abs}	Instantaneous thermal absorption efficiency

η_{carnot}	Carnot heat engine efficiency
$\eta_{coating}$	Coating efficiency
η_{max}	Maximum test bench efficiency
λ	Wavelength of radiation, nm
ρ	Reflectance
$\rho(\lambda, \phi)$	Spectral directional reflectance
ρ_w	Water density, kg/m^3
σ	Stefan-Boltzmann constant, 5.67x10^{-8}W/ m^2K^4

Contents

Index of Figures

Index of tables

Chapter 1. Introduction

One of the biggest challenges that civilization currently faces is the climate change (greenhouse effect) caused by the release of carbon dioxide emissions from fossil fuel resources such as coal, natural gas and oil. In recent decades, with the increase in world population, global energy demand has also increased, and with it, the excessive use of fossil fuels, particularly in the industrial sector, so intensifying the environmental issue [1-3]. In order to ensure energy security and sustainability, several international commitments and climate initiatives, such as the Paris agreement in 2015 or Kyoto protocol agreement, have been taken for achieving a sustainable low-carbon economy [4,5]. Therefore, sustainable technologies for industrial applications operating with clean energy such as the solar radiation are required.

Solar radiation is defined as the radiant energy emitted by the sun in the form of electromagnetic energy. This radiant energy results from the continuous thermonuclear fusion processes that transform hydrogen atoms to helium. The total radiant energy emitted by the sun has been estimated in approximately $3.8\,x10^{23}$ kW, which is radiated outwards in all directions [6]. Accordingly, the solar radiation incident over the earth is estimated to be around $1.7\,x10^{14}$ kW. The transmitted solar energy passing through the atmosphere and reaching the earth surface is about $1.1\,x10^{14}$ kW; the rest is reflected/absorbed by the atmosphere. This quantity of solar energy falling over the earth has been appraised to cover the whole-year world energy demand in only 1 hour, approximately [6-8].

Solar energy is a plentiful, limitless and non-polluting source of energy that mainly provides light and heat, which not only is involved in numerous processes for life on earth (photosynthesis), but also contributes with the generation of various renewable energy sources such as wind, biomass, tidal energy, among others [1]. Therefore, in recent years, technologies for harnessing solar energy have been widely investigated and developed for improving their production, cost-effectiveness and efficiency.

Currently, one of the most potential technologies for harnessing of the solar resource is the concentrating solar power (CSP) technology [9]. This solar technology is based on optical arrangements of reflective materials, geometrically designed for focusing solar beam irradiance

over a smaller area. Consequently, the direct normal irradiance (DNI) of the sun (1000 W/m^2) can be increased, generating a higher level of temperature and flux density. With this sustainable technology, solar irradiance is converted into heat and transferred to a working fluid. Then, this heat can be used in a wide variety of applications, e.g.: solar heat for industrial processes (SHIP), electricity generation or the production of solar fuels (thermochemical) [10]. Furthermore, CSP systems can also introduce thermal energy storage (TES) and backup systems. These storage systems provide continuous and stable energy supply, avoiding hourly dependences and providing the main advantage of CSP which is dispatchability [11].

According to the international renewable energy agency (IRENA), cumulative CSP installed capacity grew five-fold, globally, between 2010 and 2019, to reach around 6.3 GW. IRENA also reports that the weighted average costs for electricity of CSP plants fell by 47% between 2010 and 2019, from USD 0.346/kWh to USD 0.182/kWh [12]. In this context, renewable power generation costs have dropped drastically over the past decade, driven by steadily improving technologies, more competitive supply chains and the growing experience of project developers.

In general, CSP systems can be classified in two groups based on the optical arrangement by which the sunlight is concentrated: line-focusing and point-focusing systems. Line-focusing systems utilize a linear receiver for absorbing the concentrated solar irradiance along a single axis (Fig. 1.1a), whereas point-focusing systems concentrate the radiation on a single point (Fig. 1.1b). Line-focusing CSP systems are: parabolic trough collector (PTC), linear Fresnel collector (LFC) and compound parabolic collector (CPC); while point-focusing systems are: parabolic dish collector (PDC), solar power tower (SPT) and solar furnace (SF). Typically, PDC and SPT can reach higher efficiencies due to the higher concentration ratios, but at a higher cost in comparison with line-focusing systems [10]. Concentration ratios of line-focusing CSP can offer temperature ranges of 60-400 °C, while the temperature range for point-focusing can cover 100-2000 °C [6].

Typically, for line-focusing CSP, the solar receiver (the absorber) is composed of a metallic tube, mainly manufactured with materials such as copper, aluminum or stainless steel which are commonly covered with a solar absorber coating (SAC) for improving the solar flux absorption [13]. For point-focusing CSP, solar receivers can be categorized in external and cavity receivers. In external receivers, the active area (absorber) slightly matches the receiver surface, while cavity

receivers are enclosures that trap the solar irradiation by multi reflection, increasing the absorption efficiency. For SPT systems, numerical analyses on the effect of the optical properties of SACs have been conducted by comparing external and cavity receivers [14]. Results showed that, for external receivers, SACs with a higher solar absorptance can contribute to achieve a higher system's efficiency. Therefore, SACs play a fundamental role on solar receivers because they can increase the absorption level of the sunlight spectrum, improving the optical efficiency of the system.

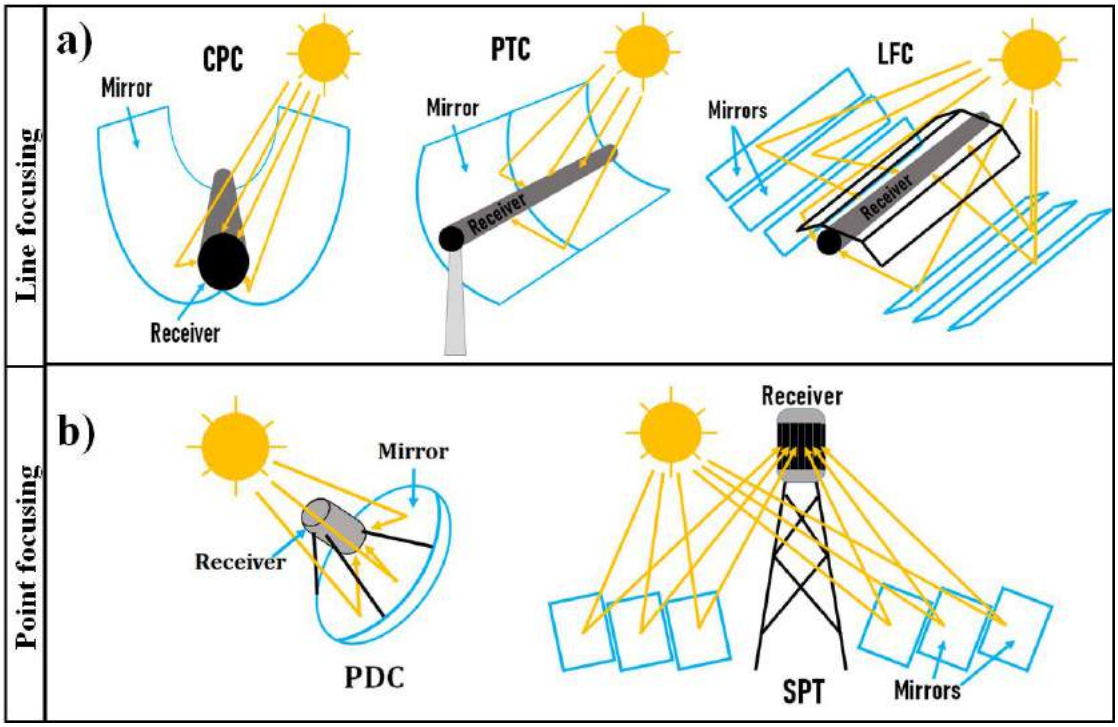

Fig. 1.1. Schematic of the CSP technologies: a) line-focusing and b) point-focusing systems.

In order to design reliable CSP technologies, great attention must be paid on critical properties of the tandem solar receiver-coating, such as photo-thermal properties (absorptivity, emissivity), due to the fact that the system efficiency mainly depends on their heat transfer capabilities. When solar receivers are exposed to intense cyclic thermal stress, these properties are change due to material aging, producing physical and chemical receiver degradation [15]. Therefore, assessments under concentrated solar irradiance in continuous and controlled conditions are needed to reproduce accelerated degradation and evaluate solar materials performances through all the processes. Consequently, optical-thermal properties of the receiver-coating can be investigated and a suitable design can be achieved. However, one of the greatest challenges in the usage of the solar resource

is the intermittent nature of the solar radiation. This, due to the fact that the solar energy is a function of many factors, such as geographical position, month of the year, day and time, as well as atmospheric conditions [9]. Therefore, an excellent alternative for testing solar thermal technologies is with the aid of a high-flux solar simulator (HFSS) and a controlled lab-scale environment.

The development of the HFSS technology started at the beginning of the 1990′s when more sophisticated high-discharge arc lamps were commercially available such as xenon arc lamps. These types of lamps can offer a color temperature of about 6000 K which approaches the terrestrial solar spectrum [16]. Currently, the DLR Institute, in Germany, has developed the largest HFSS worldwide, called "SynLight". This facility is comprised of 148 x 7 kW_e xenon short-arc lamps delivering a peak flux of 12.5 MW/m^2. HFSSs provide an excellent testing environment for full-scale solar reactors and CSP technologies [17]. Besides offering controllable light flux levels without weather constrains, the main advantage of constructing a HFSS is the possibility to carry out novel solar thermal researches by studying the effects of high-flux concentrations on CSP technologies for their further progress.

1.1 Motivation

Currently, one of the sectors with the highest global energy demand is the industrial sector for applications such as food, wine and beverage, textiles, manufacturing, electricity generation, transport equipment, and chemical industries, among others [18,19]. In general terms, industry consumes about 32% of the total demanded energy worldwide. Specifically, 74% of this demanded energy is used for meeting the industrial process heating operations, of which ~55% is required in the range of 60-400 °C, and 45% is needed above 400 °C [19,20]. Currently, solar heat for industrial processes (SHIP) is one of the most important application fields where CSP technologies can be integrated for applications such as: dehydration processes, preheating of input and raw materials, pasteurization and sterilization, desalination and distillation, among others [21-23].

In order to meet the SHIP temperature requirements, both linear-focusing and point-focusing CSP systems, can be ideal candidates, offering low-medium (60-400 °C) and medium-high (400-1000 °C) temperature levels, respectively. Accordingly, various strategies have been widely investigated for integrating CSP systems within the industry [24-28]. Therefore, an alternative to

the fossil fuel based energy sources can be attained, as well as an attractive way for achieving a sustainable low-carbon economy [2,22]. Nevertheless, the common barrier of these applications is the economic competitiveness, which is partially due to the relatively low solar system efficiency [27].

1.2 Justification

The solar receiver is the critical part of any solar thermal system and is considered one of the main bottlenecks in improving the CSP performances. Solar receivers have to withstand high flux levels and thermal stress, and work in a high-temperature oxidation environment while they absorb and convert solar irradiation into thermal power with minimal optical and thermal losses [13]. In order to develop high-efficient and low-cost solar technologies, new designs of solar receivers, material testing and accelerated aging tests under a stable assessment environment are required for improving their optical-thermal efficiency and optimal service life.

HFSSs are identified as key facilities for solar thermal and thermochemical research, offering artificial concentrated solar irradiance for conducting high-quality indoor assessments and emulating the operation of solar systems such as; SF, PDC or SPT [29]. The development of an HFSS contributes to the research and optimization of efficient solar absorber receivers, so improving the performance and competitiveness of solar technologies. SACs are of great interest to the industry, since they improve the capabilities of CSP systems in terms of solar-to-heat conversion efficiency; with the potential to generate a significant impact on the national market by the use of this clean energy and allowing migration towards a more sustainable model of society.

1.3 Objectives

The main objective of this PhD thesis is the optical design and characterization of an HFSS for the development of a well-controlled experimental platform for researching solar-thermal materials for low, medium and high-temperature applications; specifically, solar absorber coatings. Particular objectives are described as follows:

- HFSS design: Determine the suitable lamp-reflector design and the whole optical array of the HFSS by performing a numerical analysis through the use of the Monte Carlo ray-tracing technique.

- HFSS characterization: Implement an optical method for measuring the radiative flux characteristics of the HFSS (flux map).
- Radiative flux modulation of the solar simulator: Defining a strategy for providing controllable light flux levels to adjust the proper output power for a particular testing assessment.
- Experimental platform for solar-thermal research: Development of a calorimetric test bench for the evaluation of commercial and experimental solar absorber coatings.

Chapter 2. State of the art

2.1 Solar simulators

The solar simulator can be defined as an artificial solar radiation facility comprised of optical reflecting materials coupled with specialized high discharge arc lamps for offering a controllable light source with spectral output quite similar to that of the terrestrial solar spectrum.

In general, solar simulators can be classified in two main groups according to the output irradiance level on their target: low flux solar simulator (LFSS) and high flux solar simulator (HFSS) [30]. In the first case, the LFSS, also called non-concentrating solar simulator, delivers collimated, homogeneous solar irradiance for approaching the terrestrial Direct Normal Irradiance (DNI) with a flux density of about 1 sun (1 sun = 1000 W/m^2) in average. On the other hand, HFSSs are facilities which particular characteristic is the highly concentrated flux density into a common focal point, mimicking CSP systems and offering from hundreds to thousands of suns [29].

2.1.1 Low flux solar simulator

At the beginning of the 1960's LFSSs were firstly developed for thermal-vacuum space chamber testing and space environment simulation for Earth satellites and spacecraft assessments [31]. These LFSSs utilized carbon-arc and mercury-xenon lamps delivering intensities of up to 1500 W/m^2. In parallel with this investigations, new series of programs were sponsored in order to develop low-cost high-efficient facilities to simulate the space solar radiation in ground-test chambers [32]. A decade later, standard methods for solar terrestrial applications such as solar photovoltaic (PV) cells and solar thermal collectors were addressed in order to determine procedures for solar indoor assessments. From these established procedures, a solar irradiance of 1000 W/m^2 with an air mass AM1.5 of spectral composition (see Fig. 2.1) were chosen for standardizing indoor tests with solar simulators; since important solar installations and industries are located at mid latitudes with a zenith angle of approximately 48° [33].

Currently, commercial and custom-made LFSSs are utilized for terrestrial solar research, including PV cells, solar-thermal collectors and solar steam generators. Typical designs of LFSS for PV solar cell characterization are based on only one xenon arc lamp, due to the requirement of high collimation of light and the reduced target area (<10 cm^2), simplifying the design [34]. For instance, a xenon flash light LFSS was developed for the characterization of PV cells, delivering

an adjustable irradiance of 800-1000 W/m^2 and offering a spatial flux uniformity of ±95% over a target area of 9 cm^2 [35].

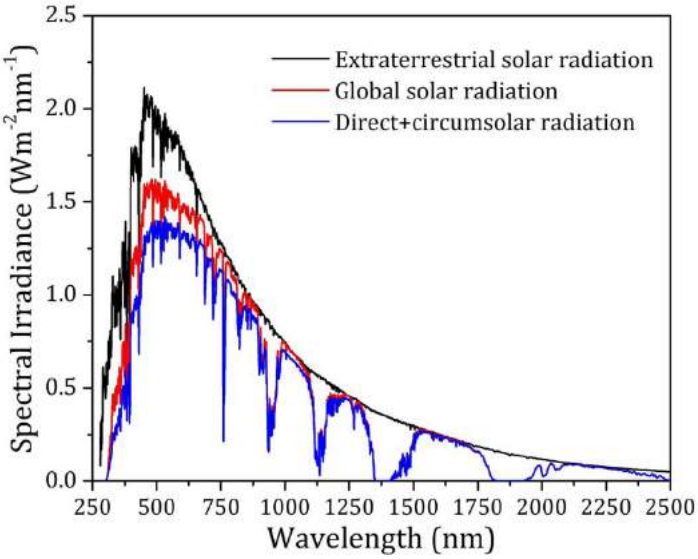

Fig. 2.1. ASTM G-173-03 reference spectra.

Another type of non-concentrating solar simulator, is the multi-lamp (or large-scale) LFSS. Unlike single-lamp LFSSs for PV cell applications, this type of solar simulator requires a greater number of lamps for covering larger testing areas, and they are usually employed for testing the performances of PV and photovoltaic thermal modules (PVT), as well as flat plate thermal collectors (FPTC) [36-38]. An example of this kind of facility is the multi-lamp LFSS comprised of 35 × 575 W_e Metal Halide (MH) lamps which was constructed for testing PV modules and solar-thermal applications [39]. This facility delivers a mean flux of 791 W/m^2 on a target area of 2200 mm × 1500 mm, offering a flux uniformity of 94.3%.

Currently, one of the main challenges in improving the requirements of solar energy research is the suitable optical design of solar simulators for conducting indoor efficiency tests with uniform and reliable radiative flux outputs. An inadequate solar simulator design can introduce uncertainties in the indoor thermal efficiency assessment, resulting in an inaccurate evaluation of the solar collectors [40]. In this context, new methodologies for the optical designs of non-concentrating solar simulators can provide further progress in enhancing the performances of these facilities.

2.1.2 High flux solar simulator

High-Flux Solar Simulators (HFSSs) are facilities used for researching and developing efficient thermodynamic cycles which demand high temperatures and high flux levels [30]. Similar to LFSSs, HFSSs can be classified in single-lamp and multi-lamp depending on the design purposes and applications. HFSSs were firstly developed in the 1990´s for the study of high-temperature solar thermochemical processes with absorbing gas-particle mixtures along with a solar reactor [16]. This solar simulator was developed with only one high pressure xenon arc lamp of 20 kW_e delivering 16 MW/m^2 over a target area of 7 cm x 7 cm. Later, at the ETH-Zurich a single-lamp HFSS was principally designed for investigating solar-thermal and thermochemical processes at temperatures up to 3000 K such as the production of solar fuels (solar hydrogen). This solar simulator was designed with a high-pressure 200 kW_e argon arc lamp which delivers a radiative power up to 75 kW with a peak flux exceeding 4.25 MW/m^2 [41]. This is the highest power consuming light-source implemented for a single-lamp HFSS that is reported in the literature to date.

At the mid 2000's, great advances in PV cells gave rise to new investigations with Concentrating Photovoltaics (CPV) [35]. The CPV technology is comprised of optical arrays for focusing the beam radiation onto the solar cell, making them cost-effective due to the reduced area of these cells, higher electricity production, as well as being more suitable for larger installation [42]. Therefore, new designs of single-lamp HFSSs for solar-thermal, thermochemical processes and CPV applications were developed [43]. For instance, a pulsed solar simulator was developed and characterized for CPV cell calibration, obtaining a radiative flux range from 7 to 1500 kW/m^2 by using a single Xenon arc lamp [44].

Multi-lamp HFSSs are mainly designed for mimicking linear and point-focusing CSP technologies such as PTC, CPC, PDC, SPT [45-47]. The design objective is to achieve the directional, spatial and spectral distributions of those systems principally for testing solar materials and components for high temperature and thermochemical applications. At the Paul Scherrer Institute (PSI), a HFSS capable of reaching a peak flux of 11 MW/m^2 and 50 kW of radiative power over a target diameter of 60 mm was developed for thermochemical process research and advance high-temperature materials [29]. A truncated ellipsoidal reflector along with a 15 kW_e high discharge xenon arc lamp were optically analyzed for constructing each of the units of the solar simulator. Fig. 2.2

shows the layout of the 10 lamp-reflector array where the radiation is delivered to the target within a rim angle of 40.6° horizontally and 27° vertically. The HFSS equipment includes ten rectifiers, electrode cooling and control systems. The flux level is adjusted by individually switching on/off the required lamps, as well as by varying the electric current between 70% and 100%. From the front view of the arrangement showed in Fig. 2.2a, it can be observed different reflector geometries. This is carried out in order to achieve more defined Gaussian flux distribution profiles on the focal plane and reduce spillage losses from the entrance of cavity receivers [29].

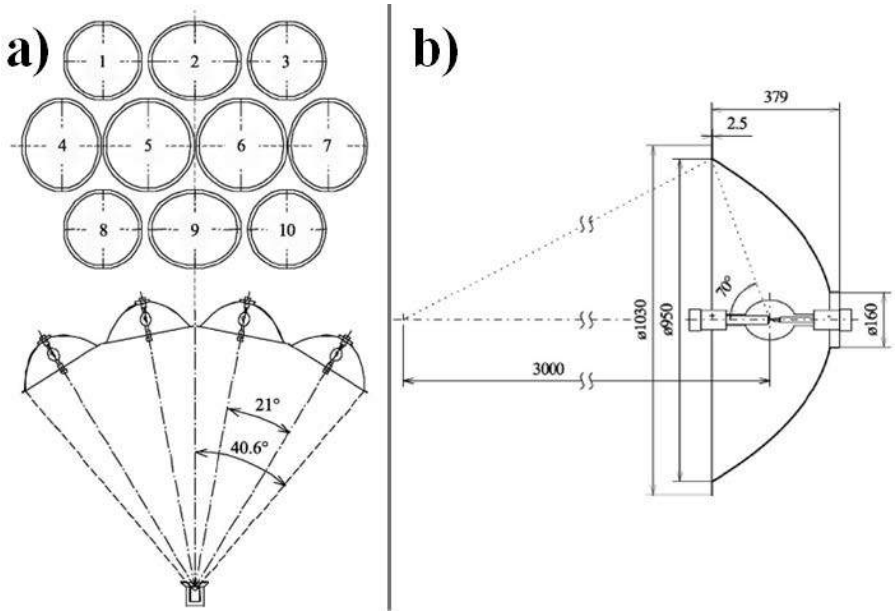

Fig. 2.2. a) Optical layout of 10 lamp-reflector units; b) Ellipsoidal reflector geometry coupled with a xenon short arc lamp, elaborated from [29].

Similarly, at the German Aerospace Center (DLR), the same methodology was implemented by using a 10 lamp-reflector unit array, each unit comprised of a xenon arc lamp coupled with a truncated ellipsoid of revolution [48]. In this design, the input power per lamp of 6 kW_e was lower than the PSI HFSS of 15 kW_e per lamp. Later, new methodologies for multi-lamp HFSSs were described for a suitable optical design of the facility by optimizing the lamp arrangement through ray-tracing techniques [49]. Nowadays, HFSSs that utilize up to 18 short arc lamps have been constructed as a result of those schematic approaches, delivering flux peaks of about 21.7 MW/m^2 [50]. In order to develop a high efficient solar simulator, with suitable radiative flux characteristics similar to those of CSP systems, the selection of the main components needs to be determined in advance.

2.1.2.1 Light source

The most critical part in designing a solar simulator is the selection of the light source. This important component determines the spectral quality of the concentrated artificial sunlight over the target and imposes limits on the optical design of the concentrating system. Traditionally, high discharge arc lamps of xenon, argon and metal halides (MH) are the light sources used for the development of HFSSs [30].

The xenon lamp is a high discharge arc lamp that produces light by applying a DC current through its electrodes. Then, an electric arc is formed between the anode and cathode by means of the ionization of the high pressure xenon gas (≤40 bar). Fig. 2.3 shows the emission spectrum of a xenon arc lamp in comparison with a blackbody of 6000 K and with the G173-03 reference solar spectrum [49]. Xenon arc lamps are the most widely light sources used for solar simulator applications due to its major advantages such as a spectrally stable output, spectral range close to that of the terrestrial solar spectrum, in addition to offering a shorter and brighter arc light (point source) in comparison with similar arc lamps [51]. This last advantage is due to the fact that xenon lamps provide a smaller electrode gap, generating a smaller magnification of the arc light and producing a more defined Gaussian flux distribution. Nevertheless, the main disadvantages of this discharge arc lamp are: the strong emission peaks in the spectral band of 800-1000 nm (see Fig. 2.3), the high power consumption and cost-maintenance, as well as the short useful lifetime (≤1000 hrs.). Furthermore, when higher flux levels of power output are required such as in HFSS applications (≥6kW$_e$ per lamp), a more complex cooling system and expensive power supply become mandatory, resulting in a high-cost system. Despite these disadvantages, xenon lamps are the main option for solar simulator applications because they have been well characterized and validated through the years for solar-thermal, thermochemical and PV cells research [33,51].

The argon arc lamp is another kind of high discharge arc lamp implemented for solar simulator applications. This lamp generates radiant power outputs with spectral composition similar to the natural sunlight with a blackbody spectrum of about 6500 K. This kind of lamp utilizes argon gas at high pressure (7-10 bar) and its emission is in the spectral range of 275-1525 nm [30,41]. Similar to xenon lamps, argon lamps emit strong peaks in the infrared spectrum and produce higher output power in the ultraviolet band compared with xenon lamps.

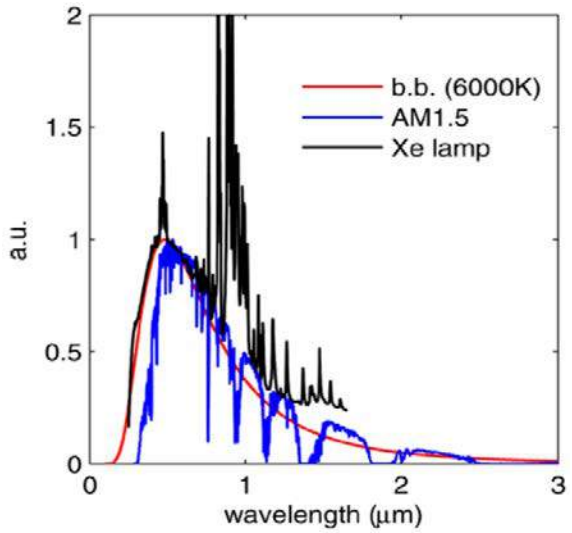

Fig. 2.3. Emission spectrum comparison of a xenon arc lamp, a blackbody radiation of 6000 K and the G173-03, elaborated from [49].

Metal halide (MH) lamps have recently increased their usage for solar simulator applications due to advances in their design quality. MH lamps offer: higher energy conversion efficiency than xenon and argon lamps; provide a longer period of service life and relative low cost; offer a good spectral match to the natural solar output and have a lower explosion risk, due to their double envelope inside the bulb [33,51]. Furthermore, MH lamps can provide a higher light intensity due to the lumen per Watt conversion rate over 100 lm/W [30,52].

Fig. 2.4 shows the power emission level of the xenon, argon and MH lamps compared with the natural sunlight in the spectral range of 300-1000 nm [30]. It can be clearly seen that MH lamps matches better with the solar spectrum, while xenon and argon lamps emit higher level of IR radiation. On the other hand, MH lamps have a longer electrode gap, resulting in a higher magnification of the arc light and making difficult a proper concentrated irradiance distribution. Moreover, the radiative power output can result spectrally unstable due to oscillations produced in the AC power supply [53]. Despite this fact, HFSSs have recently been developed with the help of modern MH lamps [51,52,54]. Currently, there is not an HFSS designed with a combination of these type of lamps (xenon, argon and MH lamps), which could imply a more complex optical design for each lamp type in the system. Other light sources that have been employed to design solar simulators, particularly LFSSs, are: carbon arc lamps, quartz-tungsten halogen lamps, mercury-xenon lamps, light emitting diode (LED) and super continuum laser [51]. Currently, all

this kind of light sources have not been implemented for HFSSs due to the light intensity is quite low for concentrating solar power applications [32].

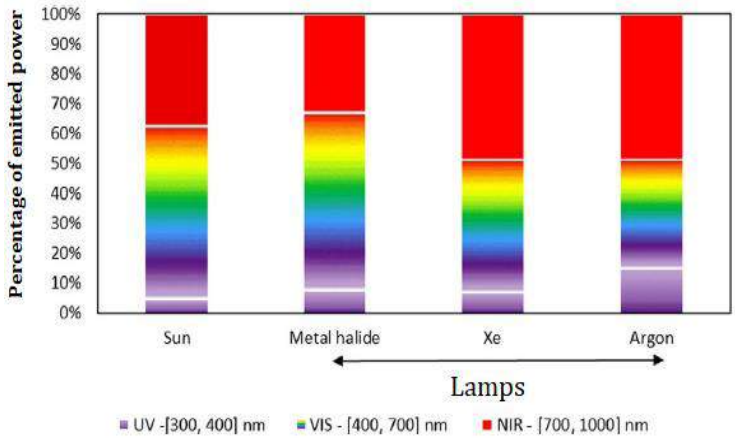

Fig. 2.4. Comparison of light sources and the G173-03 reference spectra in the band of 300-1000 nm, taken from [30].

2.1.2.2 Concentrator

The other critical component for designing a solar simulator is the concentrator. Typically, the concentrator is an optical reflector manufactured with aluminum and with the shape of an ellipsoid of revolution as illustrated in Fig. 2.5. The ellipse geometry is based on a closed curve with focal points (F_1, F_2) equidistant from the center along the semi major axis a. Eq. (2.1) depicts the mathematical representation of an ellipse with semi-major axis (a) and semi minor axis (b) on the coordinates x and y, respectively:

$$\frac{x^2}{a^2} + \frac{y^2}{b^2} = 1 \tag{2.1}$$

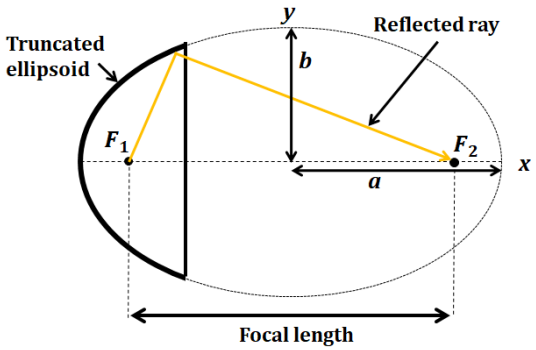

Fig. 2.5. Schematic of a truncated ellipsoidal reflector (solid part) with respect to an ellipse (short-dotted line).

Based on the geometry of an ellipsoid, a light beam coming from one of the focal points, when it impinges the reflective surface, the beam will reflect off and pass through the other focal point, see Fig. 2.5. In general, HFSSs have been widely designed with ellipsoidal reflectors due to its major advantage of providing efficient radiative transfer between the light source and the target [49].

A parabola is another geometry implemented for designing solar simulators, especially in LFSSs [38,39,55]. At the Royal Institute of Technology (KTH), a HFSS comprised of 12 xenon-arc lamps close coupled with parabolic concentrators (400 mm in diameter) was design for the testing of solar cavity receiver prototypes [56]. As well, this HFSS was designed with specialized Fresnel lenses made of silicon-on-glass (SOG) materials for concentrating the artificial sunlight with a focal length of 1500 mm, achieving a peak flux of 7.22 $\mathrm{MW/m^2}$.

The compound parabolic concentrator (CPC) has also been used in HFSSs as a secondary concentrator for increasing the heat flux density on the focal plane. For instance, the ETH-Zurich single-lamp HFSS introduced a 2D-CPC with its entrance coincident with the HFSS's focal plane for enhancing the mean heat flux [41]. Furthermore, a water-cooled 3D CPC coupled with a multi-lamp HFSS was designed for improving the flux uniformity inside a solar reduction reactor [57]. Moreover, bundles of optical fiber are another optical component implemented in HFSSs for achieving a more uniform flux distribution [58]. Bundles have a diameter of 10 mm containing 28,100 optical fibers (each of 55 μm in diameter), offering the flexibility to deliver flux distributions in 2D and 3D surfaces by transmitting the flux output of 500 $\mathrm{kW/m^2}$ to the target. Due to the flat absorption characteristics of the fiber in different bands, the spectral output is practically the same as its incident spectrum, as explained in [58].

Most of the developed HFSSs implement xenon arc lamps and ellipsoidal reflectors as the main design components. Moreover, concentrators of different geometries and specialized optical materials can be used as a complement for improving the optical efficiency. In the present study, xenon arc lamps coupled with ellipsoidal reflectors are chosen for designing a HFSS which has the versatility to regulate the flux density in a mechanical form (detailed in Chapter 3 and 4). Once the critical components have been chosen, theoretical analysis are carried out for predicting the radiative flux characteristics and performances that the optical system can deliver, which is discussed in the next section.

2.1.3 Ray-tracing analysis for HFSSs

In energy transfer studies, radiative properties changing with direction and geometrical shapes could make of the analysis a more complex issue when applying conventional numerical techniques. Consequently, statistical approaches can be implemented through sampling techniques. These type of sampling methods are commonly called Monte Carlo (MC) techniques [59], and their prediction accuracy depends mainly on the sample size. Accordingly, thermal-radiation analyzes can be approached with MC techniques because light beams travel in discrete packages throughout relatively long distances along a straight path until interacting with matter. This involves tracking the history of statistically relevant photon packages from the emission point to the absorption point. Therefore, one of the main useful tool to perform optical designs for concentrating solar power technologies is the Monte Carlo ray-tracing (MCRT) method. It is used to simulate and predict, in a precise way, the irradiance flux distribution in the focal plane of the concentration system [60].

In general, a multi-lamp HFSS comprises: a set of illumination sources (e.g. xenon arc lamps) and reflectors that concentrate the radiation delivered by the lamps toward a unique focal point. Traditionally, the concentrator is designed with a truncated ellipsoid of revolution. Multi lamp-reflector arrays are configured with such a geometry that all units share a common focal point (see Fig. 2.2a). Previous studies have clearly explained that, placing an arc lamp in one of the foci of the ellipsoid and a target in the other one shall result in a good radiative transfer between both [61]. The radiative transfer efficiency η can be defined as the fraction of radiant energy coming from the light source Q_{sr} and the energy incident on the target Q_{tg}, as described by the Eq. (2.2):

$$\eta = \frac{Q_{tg}}{Q_{sr}} \tag{2.2}$$

In order to obtain a high radiative transfer efficiency and reduce radiative losses, specific geometrical parameters have to be taken into consideration in the design of an ellipsoidal concentrator. The modification and selection of design parameters such as truncation diameter, ellipse´s eccentricity, concentrator height, focal length, as well as semi-major and minor axes, *a* and *b* (see Eq. 2.1) will be involved in achieving good performance in radiative transfer efficiency. For instance, a large eccentricity can lead to a large focal length, implying that the ellipsoidal concentrator will no longer focus radiation efficiently due to the scattered of light by larger radiation path lengths.

With the development of multi-lamp HFSSs, MCRT codes have been generated for modeling the radiative exchange between arbitrarily arranged surfaces such as a light source and a target. For instance, a free and open-source MCRT code (VEGAS) was developed for provide radiative boundary conditions for CSP modeling as well as HFSSs [62]. The PSI HFSS, comprised of 10 xenon lamps (see Fig. 2.2), was optimized by means of the VEGAS code, computing the transfer efficiency with $5x10^6$ rays per run for ten independent runs. The electrodes of the xenon lamp (15 kW_e) were modeled as cylindrical rods and the arc light as a sphere of 9 mm in diameter positioned at the main focus F_1. The concentrators were set as specular gray surfaces, with a directional-hemispherical total reflectivity of 90%. The transfer efficiency η was presented as a function of the focal distance, reporting that η reaches a maximum value of 34% by implementing a focal distance of 3000 mm, truncation diameter of 950 mm and eccentricity of 0.87 [29].

Similarly, the 45 kW_e HFSS designed at the University of Minnesota was optimized with the aid of the VEGAS code [63]. By using the MCRT analysis, the optimal reflector shape, dependent on the eccentricity, was determined by improving the transfer efficiency at reasonable uniformity levels of the flux distribution on the target. Since the xenon lamps do not emit as an ideal point source, the arc light was modeled as a cylindrical arc of 2 mm in radius and 6.3 mm in length, corresponding to the arc light of the lamp and assuming isotropic and uniform emission. Theoretical results showed a radiative power of 7.5 kW delivered over a circular disk of 60 mm in diameter, reaching a transfer efficiency of 30%.

Based on the concept of identical lamp-reflector units configured in concentric rows, a systematic methodology for designing a set of multi-lamp HFSSs was performed by generating an MC ray-tracing simulation [49]. The modeling consisted on 18 x 2.5 kW_e xenon arc lamps uniformly emitting with the shape of a cylindrical arc light source with length and radius of 4.5 mm and 0.75 mm, respectively. For every ray, pseudorandom numbers were generated and used to determine the coordinates of the emission point, and the azimuthal and polar angles describing the direction of emitted rays. A cumulative distribution function CDF was implemented for the polar angles to random numbers. The ray-tracing results for the HFSS with all 18 lamps in operation presented a radiative power of 10.6 kW, a mean flux of 3.8 MW/m^2, a peak flux of 9.5 MW/m^2 and a transfer efficiency of 56% over a target diameter of 60 mm.

Commercial ray-tracing software have also been used for the design and optical improvement of solar simulators of high concentrated flux. OptiCAD® is a flexible, optical analysis, and visualization program that models many optical solid components, including lenses, mirrors, light pipes and imported CAD surfaces. This software was implemented for the assessment of the radiative flux distribution at the focal plane of the DLR HFSS [48]. Consequently, it was possible to compare in detail the simulation results with measured data to estimate the flux distribution achieved by the complete assembly.

Another software that applies the MCRT method for enhancing the performances in optical systems is TracePro® by Lambda Research. This commercial software has been commonly used in solar simulator applications [46,54,64,65]. For instance, TracePro was utilized for optimizing a 7 lamps HFSS where a concept of non-coaxial deflection angle was integrated to the typical ellipsoidal reflector for improving the spatial flux uniformity [65]. By comparing simulations and experiments, the relative deviation of total radiative power was reported in 4.9%.

In this doctoral thesis, TracePro is used as the main tool for the analysis of the optical design of the HFSS due to its great capability to predict radiative flux characteristics with complex 3D optical system models.

2.1.4 Radiative flux characterization of HFSSs

In order to carry out research on concentrated solar energy by using a solar simulator, it is necessary to determine accurately the optical-thermal performances of the system. Therefore, measurements of the radiative flux distribution in the focal plane (flux map) are required for defining the boundary conditions established by the concentrating optical system. Then, suitable radiative power inputs can be set based on the research applications of the solar simulator. Typically, the characterization of the radiative flux distribution of a concentrating solar system is performed by using direct or indirect flux mapping techniques [66]. Direct flux mapping techniques are those in which one or more solar flux gauges are installed in the focal plane to directly measure the level of radiative flux delivered by the solar simulator [47,52]. The direct flux mapping is the most accurate of the methods implemented for characterizing HFSSs. The heat flux gauge typically used and widely characterized for usage in concentrating solar applications is the Gardon type gauge [67]. When using a single flux gauge, it is necessary to scan over the area of interest for fully mapping the flux distribution. The disadvantage of this method is the low spatial

resolution, which makes it less efficient. Increasing the number of sensors to map the flux distribution can contribute to better resolution and lower measurement uncertainty. However, the complexity in cost and maintenance, in addition to the cooling system required to protect the flux gauge from the high concentrated flux, increases with the number of used sensors [66]. For example, an 130 kW_e HFSS was characterized by using a Gardon gauge coupled with a copper plate covered with black paint, both Gardon and plate, cooled with water [68]. The flux spot was scanned at a diameter of 200 mm with a 20 mm of displacement distance, a total flux mapping time of 2642 s was required and a measurement uncertainty of 7.46% was obtained.

The indirect flux mapping method consists of using a high-resolution camera such as a charged coupled device (CCD) camera or a complementary metal oxide semiconductor (CMOS) camera to spatially capture, in the pixels, all the information of the concentrated light brightness. In this method, the intensity levels of the pixels are related to the levels of solar irradiance, where a linear relationship has been widely demonstrated [43,50]. Furthermore, a Gardon flux sensor is usually used along with a target covered with a diffusely reflective material to simulate a Lambertian distribution of light [69]. The indirect flux mapping method is typically used in CSP systems due to: it is low cost compared to the direct method as it requires only one flux sensor, it is faster in acquiring data, in addition to offering high spatial resolution [70]. Regarding solar simulators, the indirect flux mapping method has been implemented using two Lambertian targets; a static target, where the flux gauge is installed, and a mobile one for recording the concentrated flux spot [69,71]. However, the mobile target is displaced in front of the static one to capture the concentrated brightness, causing the flux map to be captured outside the focal plane. To reduce this problem and reduce measurement errors, the moving target must be reduced in thickness as much as possible. However, by reducing its thickness, the interval time in which the mobile target is placed on the focal point is reduced due to possible damage from the high concentrated flux. In this sense, the use of a single Lambertian target contributes not only to eliminate this error, but also to keep the target the needed time to take the appropriate number of images of the flux spot. Abuseada et al. [72] determined the minimum threshold of captured images to obtain a more accurate flux characterization by calculating the root mean square error (RMSE) for the total power and maximum deviation. Accordingly, the RMSE value is reduced by increasing the number of captured images, showing that after 30 images the reduction of RMSE is negligible.

Calorimetric techniques have also been used in the characterization of solar simulators [43]. For instance, Codd et al. reported the characterization of an HFSS by quantifying the thermal balance between the incident flux on an instrumented receiver and the increase in temperature, assuming steady state conditions [73]. An alternative for using a heat flux gauge together with the indirect method is the use of a cavity-type calorimeter for HFSS calibration [74]. In this way the irradiance absorption is maximized and the spectral dependencies are decreased. Another technique reported in the literature is the use of a calibrated thermographic (IR) camera to determine the incident heat flux. The flux map is calculated by relating the temperature measurements captured with the IR camera together with flux measurements with a Gardon gauge [75].

In this study, the indirect flux mapping method (camera-diffuse target) is implemented for the characterization of the proposed solar simulator. Additionally, a Gardon radiometer is used to take measurements of radiative flux over the focal plane. The implemented flux characterization methodology is presented in the Chapter 3.

2.2 Solar absorber coatings

Solar receivers are key components in CSP systems, since their photo-thermal conversion performance is related to the final efficiency of the whole system. Metallic surfaces are commonly used as receiver materials for low-to-medium temperature CSP applications. For high temperature CSP such as SPT, ceramic materials or austenitic alloys (Inconel) are used. These types of materials are implemented due to their high melting point, corrosion resistance and high level of thermal conductivity [76]. In both cases, these materials are combined with coatings specially designed to maximize the absorption of solar radiation, reduce losses due to reflection, in addition to protecting the metal base from high levels of oxidation produced by the high thermal load. These optical-thermal materials are known as solar absorber coatings (SAC), which can be classified in selective and non-selective coatings.

2.2.1 Description of solar absorbers

By analyzing in detail the radiative properties of a surface with finite thickness on which a radiative flux is incident; part of the radiation will be reflected, part will be absorbed and part will be transmitted through the surface [59]. If the object is thick enough, it can be considered opaque, meaning that radiation cannot be transmitted through it. On the basis that all radiation must be

absorbed or reflected according to the conservation of energy, the following equation, Eq. (2.3), can be established:

$$\alpha + \rho = 1 \tag{2.3}$$

where α is the absorptance, defined as the ratio of the absorbed solar radiation to the incident solar radiation; and ρ, the reflectance, defined as the ratio between the reflected part of the incident radiation to the total incident radiation [77]. Therefore, a SAC can be referred to a material whose main property is the high level of absorptance in the solar spectrum, maximizing the photo-thermal conversion process in solar-thermal applications. However, during the radiation absorption process, the material's temperature can increase to such an extent that the energy is re-emitted in the form of heat according to Kirchhoff's law of thermal radiation [59].

Since all materials emit thermal radiation due to the movement of subatomic particles, thermal emittance can be defined as the fraction of radiant energy emitted by an object as a function of its temperature and wavelength, to the radiation emitted by an ideal black body at the same temperature. Taking into consideration one of the variants of Kirchhoff's law for an opaque object, the thermal emittance will be equal to the absorptance of the object, meaning, the surface will emit as much energy as it is absorbed, as a function of the temperature of the object. This implies energy losses due to emission of thermal radiation. In this sense, a selective solar absorber coating (SSAC) is one that absorbs the maximum amount of solar radiation in the spectral range of 250-2500 nm (UV-Vis-NIR, see Fig. 2.1), but reflects the amount of thermal energy from the absorber at wavelengths longer than 2500 nm, so avoiding the re-emission of thermal energy.

2.2.2 Selective and non-selective SACs

In general, selective and non-selective SACs can be categorized based on their design and optical absorption mechanisms as: semiconductor-metal tandems, dielectric-metal composites, multilayer coatings, textured surfaces and absorber paints [78]. Several techniques for producing coatings are implemented depending on materials and complexity of the design. Some of these techniques are: chemical vapor deposition (CVD), physical vapor deposition (PVD) by magnetron sputtering (DC, RF), electro-deposition, anodization, spin coating, air-plasma thermal spray, spraying deposition, among others. Characteristics of SACs are presented as follows [78-80]:

Coatings based on semiconductor-metal tandems are selective absorbers in the spectral band of the visible and near infrared, with a band gap interval between 0.4-1.3 eV. Materials such as silicon or germanium are typically used and applied by CVD.

Textured surface absorbers (e.g., ZnO-Ag, Cu-Ni) are needle-like or dendritic-shaped geometric structures designed on micro or nano-scale by lithography, CVD, or PVD. The rough surface absorbs solar radiation by optical trapping through multi-reflection.

The metal-dielectric composite (cermet), consists of metallic particles within a dielectric matrix which is deposited on a reflective metallic substrate such as copper or steel [81]. Application techniques such as electroplating, inorganic pigmentation, CVD, PVD, can be used to produce this coating. The selectivity of these materials depends on design parameters (size, orientation and shape of particles) and can reach absorptance levels of ~0.92 with thermal emittance of 0.16.

Multilayer coatings consist of the union of semi-transparent metallic layers (e.g., Cu, Ni) alternated with dielectric layers (SiO_2, Al_2O_3), mounted on a substrate to which an anti-reflective layer is applied. In this configuration, solar radiation is absorbed by the dielectric layers, while thermal emittance is reflected by the metallic layers, so obtaining great selectivity.

In general, the advantage of using SSACs is the low emittance value that they have at certain temperatures, providing a reduction in thermal losses. Furthermore, due to the mentioned application techniques, SSACs have better adherence to the substrate compared with techniques such as spray deposition. However, the low emittance requirement typically leads to quite complex and expensive deposition techniques, such as magnetron sputtering. Moreover, SSACs commonly present alterations in their structures when high cyclic thermal loads are applied (low thermal stability) and are sensitive to abrasion [79]. Currently, there are no commercial SSACs that can be used at elevated temperatures in open environments (oxidation); they are mainly implemented for CSP applications at low-medium temperature in evacuated environments. Due to the size and shape of the substrate, and the complex techniques to produce SSACs, re-coating methods are not easy to implement in the CSP plant and dismantling operations are not planned in the solar plant in case of coating failure [14].

Solar absorber paints are another type of coatings (usually non-selective) and represent a less expensive alternative to selective coatings due to the less complex fabrication and application

techniques. An important advantage of absorber paints is the ability to re-coat in a practical form on large-scale receiver surfaces. These coatings are made from synthetic pigments which are combined with solvents for applying over metallic substrates. These materials are commonly manufactured with metal oxides such as FeMnCuOx, where polymers such as silicone, siloxane resin or phenoxy resins (also called polyhydroxyl ethers) are used as binders [82]. However, binders also absorb infrared radiation, increasing thermal emittance.

Commercial absorber paints such as Solariselect, Solarect-Z, SolkoteHI/SORB-II, Thurmalox250 are spray deposited SSACs for CSP applications at low-to-medium temperatures. For high temperature CSP applications, Pyromark2500 is a silicone-based non-selective black paint, with a temperature resistance of >1000 °C. Currently, Pyromark is the standard coating for CSP plants and is widely used as a reference for many coating designs. This commercial coating offers a measured solar absorptance of 0.96, while its level of thermal emittance at 600 °C has been reported at 0.86, which implies losses due to thermal radiation [83].

2.2.2.1 SACs based on residual biomass

Recently, researches on SACs report that, novel materials based on carbon allotropes (graphite, fullerenes, graphene) have been implemented in solar-thermal applications. This, on the grounds that their amorphous graphitic structures are well-known for offering great light absorption qualities [84,85]. These new carbon-based materials for SACs have been evaluated for solar-thermal applications at low temperature levels. Such as, a bulk graphene based SAC was reported by Alami et al. [86] for the light absorption enhancement of flat-plate collectors. Results reported a maximum radiative-to-heat transfer efficiency of 69.4% as the best performance achieved when using the graphene-clad copper oxide collector compared with the commercial coating Thurmalox250 as the reference (39.5% efficiency). Recently, carbon nanoparticles have been identified in Soot of Forest Biomass (SFB), a byproduct of combustion waste. In the present PhD project, an absorber coating based on SFB has been employed as SAC for its assessment [87,88]. Although carbon nanostructured materials have been used in solar absorption applications [89], none has been developed from waste materials. The development of SACs based on biomass residual is an important unexploited market sector to date. Furthermore, it is an interesting research field due to the fact that waste materials usage helps reducing environmental impacts. Therefore, this type of coating is a promising material for solar thermal applications due to its major

advantages, such as: high solar absorptance, sustainability, low cost, easy preparation and safe application [88].

2.2.3 Methods for performance assessment of SACs

In applications with flat-plate solar collectors, standardized methods have been developed using mathematical models that take into account the degradation induced by thermal load, humidity and pollutants. In this type of analysis, important degradation parameters such as diffusion and oxidation are calculated to estimate the durability of the coating over a useful life of 25 years [79]. However, similar criteria for evaluating SACs for high temperature CSP applications are very limited. Although coatings are used in evacuated environments, they must be stable in the air in case the vacuum is breached.

2.2.3.1 Degradation assessments by thermal treatments

For CSP applications, the optical-thermal performances of solar absorber coatings are usually assessed after annealing the sample in muffle furnaces at high temperatures (~400-800 °C) for prolonged periods [90-92]. This thermal treatment has been extensively implemented to evaluate thermal fatigue and degradation in both open (oxygen) and evacuated environments [93]. Results of these studies have demonstrated that oxidation is one of the principal factors of degradation after exposing the coating to high thermal cyclic loads. These types of heat treatments are implemented to estimate firstly temperature resistance and stability. Parameters required for the testing are the selection of a proper annealing time and temperature. Then, optical properties such as absorptance are measured to calculate the optical efficiency.

2.2.3.2 Degradation assessments by accelerated aging cycles

During operation, SACs are subjected to high levels of cyclic thermal loads by sudden climatic changes (solar intermittency), so producing thermal shocks. Hence, coating can begin to degrade, causing micro-cracks and the eventual detachment from the receiver. Accelerated aging tests have been carried out using solar furnaces together with air-cooling systems to cyclically heat and cool the material and generate thermal shocks. For instance, accelerated aging tests were conducted with 4 different SACs and the Pyromark coating (reference) for SPT applications with a concentrated solar facility at PROMES-CNRS laboratory, France [94]. The objective was to observe the evolution of the optical properties of SACs through quick changes of solar input for simulating cloudy weather. After 200 cycles with temperature ranges of 450-600 °C and 450-800

°C, no significant degradation on the optical properties were observed. Furthermore, accelerated aging tests ranged from 100-850 °C were carried out by Boubault et al. for quantifying the cost-effectiveness of SACs in the CSP industry [95]. For this purpose, 3 different SACs were used: Pyromark2500, lanthanum strontium manganite oxide (LSM), and cobalt oxide (Co3O4). Though Pyromark exhibited a higher emissivity than LSM and Co3O4 coatings, it achieved a better performance in durability and thermal efficiency.

Published literature on the evaluation of SACs indicate that; currently there is no appropriate SSAC for CSP applications at high temperature that can operate in contact with oxygen. Furthermore, comparisons between selective and non-selective coatings indicate that the solar absorptance is the most important factor due to the fact that the absorbed solar irradiation is the predominant external heat input to the receiver [14]. Outcomes have also shown that the most accessible option for enhancing the performances of SACs is the development of a highly absorptive ultra-black non-selective coating [95]. In order to continue with a further progress of this technologies in terms of solar-thermal conversion efficiency, research on concentrated solar energy at laboratory-scale can be an excellent alternative for SAC assessments.

2.3 Calorimetric test bench

The solar energy performances of a CSP system depends mainly on the ability to convert concentrated solar irradiance into thermal power carried by the heat transfer fluid (HTF) such as liquids or gases. Therefore, a fundamental research subject in CSP applications is the improvement of the radiative-to-heat transfer performances and optimal service life of SACs [96]. The thermal functionality of SACs is strongly dependent on their optical-thermal properties, which are aged by cyclic thermal loads, causing physical chemical degradation. In order to perform solar thermal research with SACs, a well-controlled laboratory environment needs to be developed.

Methods for evaluating the degradation-resistance of SACs and the mechanisms that accelerate the aging have been developed based on heat treatments in ovens at high temperatures and also with high flux solar furnaces for producing thermal shocks. The drawback of thermal treatments in ovens is the unrealistic conditions for a proper photo-thermal conversion at high solar flux. In the case of solar furnaces, the main advantage is the real condition of concentrated solar irradiance for conducting suitable outdoor solar investigations. Nevertheless, the solar resource is hourly

dependent and is also conditioned by the weather. Moreover, solar furnaces require of a large space and involve high costs [30].

One of the particular objectives of this PhD project is the development of an experimental platform for solar thermal research that include the construction of a HFSS. A solar simulator offers the advantage of controlled and continuous high flux levels without weather constrains. For the assessment of selective and non-selective SACs, the development of a test bench is proposed in order to accomplish this assignment. The calorimetric test bench based on the calorimetric measuring principle is coupled with the HFSS, which is used as the radiative flux input.

In CSP research, a calorimeter is a practical instrument for measuring the concentrated solar irradiance and thermal power at the concentrator focal plane [97]. In typical calorimeters, the concentrated solar flux is intercepted, absorbed and converted into heat by the solar receiver. Subsequently, the heat is transferred through a thin wall by conduction. Lastly, the heat is taken away by an HTF by forced convection. By measuring the inlet and outlet temperature of the HTF and calculating the energy balance, the thermal power incident over the receiver can be quantified [59].

Theoretical analyses developed in the 60's have clearly explained the heat transfer process when a flat plate heat exchanger is coupled to solar concentrators of PDC and PTC [98,99]. Currently, flat-plate calorimeters have been developed to characterize the radiative flux performances of CSP systems by using copper as the absorber receiver, which is covered with a solar absorber coating. In the published literature, calorimetric efficiencies have been reported up to 90%.

Unlike flat-plate calorimeters, cavity calorimeters are enclosures designed with an orifice by which the radiation enters through, and then, radiation is absorbed by the cavity wall [100]. Commonly, absorber coatings are applied (black matte paints) inside the cavity in order to achieve high apparent absorptivity [77]. For instance, a high flux conical cavity calorimeter was developed at the DLR Solar Research Institute for purposes of characterizing the DLR Solar Furnace [100].

Table 1 shows some of the calorimeters reported in the literature that have been implemented in solar-thermal applications.

Table 2.1. Overview of calorimeters for the characterization of solar-thermal technologies.

Institute	Calorimeter Type	Calorimeter body	Material of receiver	Aperture diameter (mm)	Incident flux / power	Measuring campaign of
Institute of Solar Research (DLR)	Conical cavity	Copper	Copper	20	5000 kW/m^2 / 382W	High solar flux of the DLR Solar Furnace [100].
IER-UNAM	Conical cavity	Stainless steel-Copper	Copper	32.4	1162 kW/m^2 / 958W	Thermal power of a CSP device DEFRAC [101].
IER-UNAM	Flat plate	Stainless steel	Copper	90	50.9 kW/m^2 / 324W	Concentrated energy of the DEFRAC system [102].
Stellenbosch University	Flat plate	Nylon PA6C	Copper	90	- / 931W	Performance of small-scale heliostat field [103].
Indian Institute of Technology	Hyperboloidal cavity	Copper	Copper	20	850 kW/m^2 / 267W	Concentrated solar thermal systems in arid deserts [104].

In this study, a flat plate calorimeter-based test bench is proposed for the flux absorption efficiency assessment of different SACs along with the HFSS as the concentrated light source. The main characteristic of the proposed calorimeter design is the possibility to remove its active area (absorber element) as an interchangeable cartridge. With this approach, the absorption efficiency can be evaluated and compared by inserting different selective and non-selective SACs in the test bench. Besides, indoor testing under the same conditions of controlled irradiance level, room temperature and mass flow rate of the HTF can be accomplished. Accordingly, the performances of suitable materials for its usage in SHIP can be effectively determined. Furthermore, new low-cost, environmentally friendly SACs can be experimentally evaluated and compared with commercial coatings for a further progress in the development of this solar technology.

Chapter 3. Development and characterization of the high flux solar simulator

In this Chapter, the development of the proposed high flux solar simulator is presented. First, the optical design of the system is numerically analyzed through the use of the Monte Carlo ray-tracing (MCRT) method. Subsequently, the construction of the optical system, the main components, as well as the acquisition and control systems are described. Finally, the flux characterization of individual lamp-reflector units is carried out by means of the indirect flux mapping technique. In addition, a heat flux experiment is conducted in order to demonstrate the thermal capability that the solar simulator can achieve with a characterized material.

3.1 Optical design and physical model

3.1.1 Light source

High intensity discharge arc lamps of xenon and metal halides (MH) are widely used light sources in both HFSSs and LFSSs, due to the fact that this type of lamps offer the best approximation to the natural sunlight at high output power [30]. Some of the advantages and disadvantages that both of the lamps provide have been explained in Chapter 2. In this study, xenon short-arc lamps were selected as the light source on the grounds that the spectral output of this high-discharge arc lamp is quite comparable to that of the terrestrial solar irradiation with AM1.5, see Fig. 2.3 [49]. Moreover, the plasma ball coming from the cathode (arc light) can be approximated to an ideal point source for practical effects, due to the smaller electrode gap of the lamp. Accordingly, a more defined Gaussian flux distribution can be achieved, which is useful in point-focusing CSP applications. Therefore, an ozone-free xenon short arc lamp (XBO®2500W/HS) was chosen for the HFSS design. On the one hand, the spectral distribution of the xenon lamps does not match the solar terrestrial spectrum effectively. On the other hand, solar receivers in CSP applications are design to absorb as much concentrated solar flux as possible in the wavelength range of 300-2500 nm for producing thermal energy. As the research purposes of this study are addressed to achieve high temperature levels for heat production, similar to CSP systems, the mean radiative flux on the target plays a major role regardless of the wavelength dependence. Therefore, an accurate matching with the solar spectrum is not as significant as the flux intensity [30].

3.1.2 Reflector design

In this study, truncated ellipsoidal reflectors were selected for concentrating the radiative energy coming from the xenon lamps on a focal flux spot of approximately 100 mm with a focal distance of 2000 mm. Fig. 3.1a shows the ellipsoidal reflector model with the main design parameters, and the Fig. 3.1b shows the xenon lamp model, having 5.5 mm electrode gap and 60 mm bulb diameter. From Fig. 3.1a, $2c$ is the distance between the focal points f_1 *and* f_2 (focal length); α_c is the truncation angle subtended by the internal radius (R_{in}) of the ellipse to the point source disposed in the focus f_1 on the optical axis. The length from the focus f_1 to the internal cut radius, along the optical axis, is described as l_{cut}. The distance from the second focus f_2 to the edge of the concentrator through the optical axis is given by D_{axis}. Geometrical associations between these design parameters are described in Equations 3.1-3.5.

$$tan(\alpha_c) = \frac{R_{in}}{l_{cut}} \tag{3.1}$$

$$D_{axis} = 2c - l_{cut} \tag{3.2}$$

$$c = \frac{D_{axis}}{2} + \frac{1}{e^2 - 1}\left[\frac{D_{axis}}{2}(1 + e^2) - e\sqrt{{D_{axis}}^2 + {R_{in}}^2}\right] \tag{3.3}$$

$$a = \frac{c}{e} \tag{3.4}$$

$$b = \sqrt{a^2 - c^2} \tag{3.5}$$

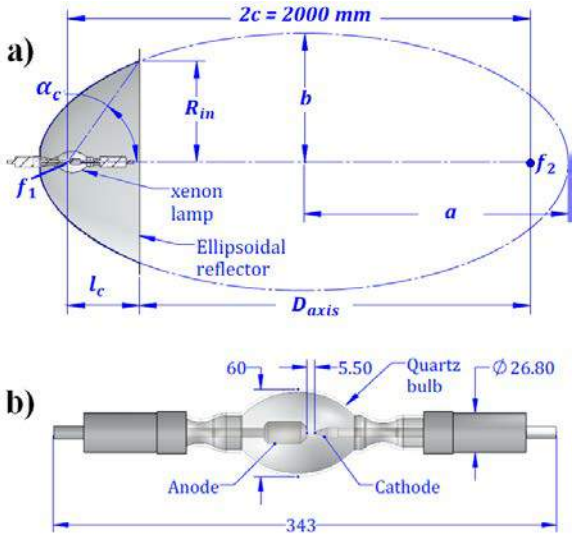

Fig. 3.1. a) Truncated ellipsoidal reflector model with the main design parameters; b) xenon arc lamp model presenting an electrode gap of 5.5 mm (units in millimeters).

First, to ensure enough space between the optical system and the focal plane, and according to restrictions of our application requirements, a distance of 2000 mm ($2c$) was chosen as the focal distance (see Fig. 3.1a). Then, the maximization of the source-to-target radiative transfer efficiency η was assessed by modifying the truncation angle α_c and the truncation radius R_{in} in the range of 25-75° and 175-325 mm, respectively. Furthermore, different values of the eccentricity e were analyzed in the same ranges for determining the optimum design, which results are presented in Section 3.4.

For the transfer efficiency analysis (Eq. (2.2)), the radiative output energy Q_s generated by the arc emitter is typically estimated to be approximately 60% of the total electric power input [49]. This is due to the imperfect electrical to radiative conversion, power losses in the form of heat and energy consumption of the power electronic components. Taking a more conservative value of 50% from the nominal input power (2.5 kW_e), the radiative output power Q_s was established for considering degradation losses and adding a safety factor into the design accuracy.

3.1.3 Solar simulator array

For the HFSS assembly, 7 xenon arc lamps were implemented in a matrix arrangement positioned onto a virtual sphere with a radius of 1846 mm measured from the center of the sphere (focal plane) to the truncation of the reflectors D_{axis} as depicted in Fig. 3.2. This matrix array is comprised of 2 lamps in the upper row, 3 lamps in the middle row and 2 lamps in the lower row, and all the lamp-reflector units share a common focus f_2 for increasing the heat flux density on the focal plane. In this configuration, the central lamp-reflector unit (1) is placed in the origin of the coordinate system and the radiative flux is concentrated towards the positive direction of the z axis. This lamp-reflector unit forms an angle with the normal of the target of about 19.46° (yz plane). In this form, a high resolution camera can be installed with its optical axis perpendicular to the target surface in order to apply the indirect flux mapping technique for characterization. This configuration allows to add 2 more lamps for achieving higher flux levels (if necessary), one on the upper section of the middle column and the other one on the lower section, forming a 3x3 matrix. Moreover, this lamp array offers the possibility to introduce different shutter curtain (SC) designs for adjusting the irradiance level and, as a consequence, obtaining different ranges of temperature. The integration and designs of SCs will be explained in detail in Chapter 4.

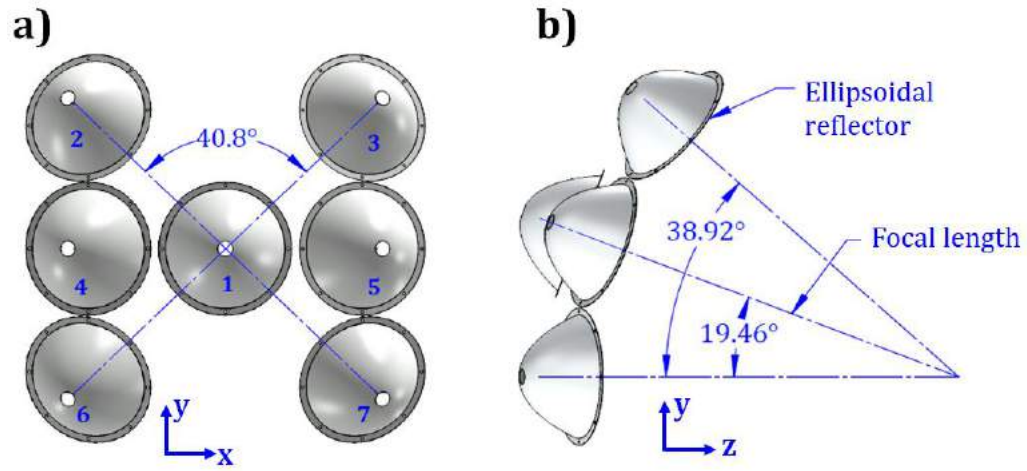

Fig. 3.2. Layout of the seven lamp high flux solar simulator assembled in a matrix array: a) front view; b) lateral view.

3.2 Ray-tracing analysis

An important and valuable tool for conducting the optical design of CSP systems and solar simulators is the Monte Carlo ray tracing (MCRT) technique, which offers assistance for enhancing optical modeling by allowing the selection of suitable design parameters [105]. In this study, the commercial software TracePro® (Lambda Research) is used for the optical design and the analysis of complex 3D geometries [106]. The software SolidWorks® was used to generate the computer-aided design (CAD) files of the lamp-reflector units and the solar simulator structure. Then, the designs were imported into TracePro for the ray-tracing analysis.

TracePro reports optical phenomena such as: light absorption, specular reflection, refraction, diffraction, and radiation scattering by following the radiative flux related with each ray. In the ray-tracing technique, the interaction between a light beam and a specular surface can be described by the Bidirectional Reflectance Distribution Function (BRDF), and it is defined as the scattered radiance per unit incident irradiance, and is described by Eq. (3.6) [107]:

$$BRDF(\theta_i, \varphi_i, \theta_r, \varphi_r) = \frac{dL_r(\theta_r, \varphi_r)}{dE_i(\theta_i, \varphi_i)} \tag{3.6}$$

where $dL_r(\theta_r, \varphi_r)$ is the unit of radiant energy per unit of solid angle $d\Omega_i$ ($\mathrm{W/m^2 sr}$); the irradiance $dE_i(\theta_i, \varphi_i)$ is the incident power flux density per unit area ($\mathrm{W/m^2}$). The angles $\theta_i, \varphi_i, \theta_r, \varphi_r$ are the polar and azimuth incident angles and polar and azimuth reflected angles,

respectively, as depicted in Fig. 3.3a. The BRDF model is independent of the incident direction. This refers to the fact that reflectance function only depends on the difference between the specular and diffuse reflection direction (scattering by rough surfaces). Fig. 3.3b shows the representation of the BRDF function of a reflective surface; $\vec{\beta}0$ is the projection of the unit vector $\hat{v}0$ in the specular direction; $\vec{\beta}$ is the projection of the unit vector $\hat{v}$ in the scattering direction; the magnitude $|\vec{\beta} - \vec{\beta}0|$ is the BRDF argument. Here, $\vec{\beta}$ and $\vec{\beta}0$ are vectors with values less than or equal to 1. This method offers an excellent model of the behavior of optical surfaces such as specular and diffusing surfaces.

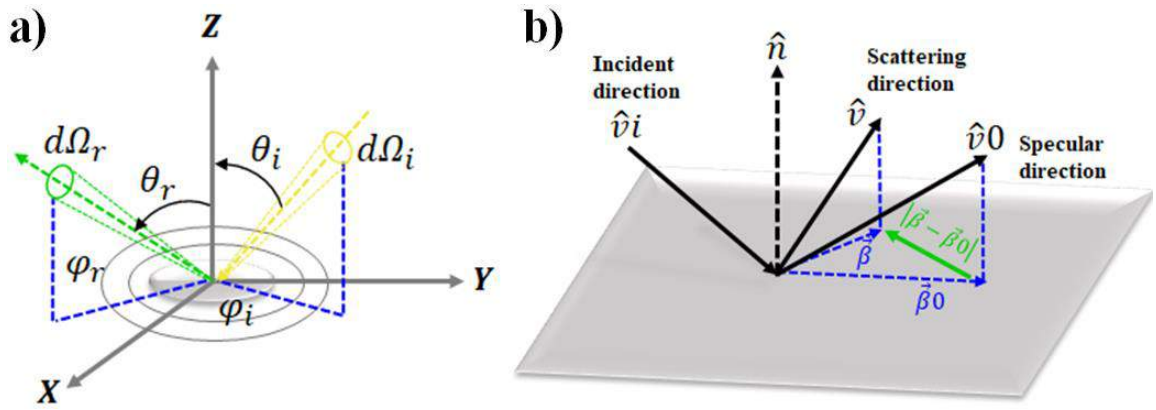

Fig. 3.3 a) Radiation reflection behavior determined by the BRDF function; b) scatter of a light beam describing the BRDF function.

The BRDF model used in TracePro is called the *ABg* model, which is a quasi-inverse-power-law model, described by the Eq. (3.7):

$$BRDF = \frac{A}{B + |\vec{\beta} - \vec{\beta}0|^{g}} \tag{3.7}$$

In this function, A, B and g are fit parameters describing the angular shape of scattering based on the optical surface properties. *B* must be greater than zero; otherwise, *g* must be zero. If *g* is zero, the surface becomes a Lambertian surface. The total reflectance *TR* is given by the integral of the BRDF function over all angles as shown in Eq. (3.8):

$$TR = \int_0^{2\pi}\int_0^{\frac{\pi}{2}} BRDF(\theta_i, \varphi_i, \theta_r, \varphi_r)\, cos\,\theta\, sin\,\theta\, d\theta d\varphi \tag{3.8}$$

Where θ and φ are angles referred to the normal vector of the surface under analysis. The sum of the absorptance, specular reflectance and diffuse reflectance for the incident irradiation on the receiver surface must be equal to unity according to the law of energy conservation.

In the determination of the BRDF, optical surface properties of the reflector were established according to the values of A= 0.018, B= 0.015 and g= 2, which are the parameters typically used in specular surfaces [106]. Therefore, the parabolic reflector surface was configured with a specular reflectance coefficient of 94.86%, absorptance of 5%, and BRDF of 0.14%. This specular reflectance value is selected in order to estimate the maximum possible performance of the solar simulator when a high reflective coating layer is applied over the surface of the concentrators. In addition, the specular reflectance will be established based on the reflectance measured on the concentrators for a proper comparison with the model.

In previous studies, the emitter arc of the high intensity discharge arc lamps was considered as a cylinder with a diffusely and uniformly distributed light emission [108]. In this study, a cylindrical shape arc emitter was modeled with a radius of $r_{cyl} = 2.3$ mm and length of $l_{cyl} = 5$ mm, the same length as the electrode gap showed in Fig. 3.1b. The cylindrical light source was positioned at the focal point f_1 inside the reflector, along the optical axis of symmetry. Results are presented in section 3.4.

3.3 Characterization methodology of the HFSS

3.3.1 Indirect flux mapping technique

In order to carry out the characterization of the HFSS the indirect flux mapping method was employed through the use of a high resolution camera and a flat target plate, which diffusely reflects the concentrated irradiance. First, pictures of the flux spot incident on the flat plate are captured, and measurements with a heat flux gauge are taken as well. Subsequently, by relating the pixel intensity level (grayscale) of the images with the radiative flux values, the mapping of the irradiance distribution over the target can be calculated [43,50,69]. The processing data of recorded images is performed by using the software MATLAB. This technique is used to obtain the spatial information of the radiative flux, as well as the total radiative power intercepted by the target. Furthermore, it is used to corroborate that the Gaussian flux distribution does not present irregularities such as undesirable peaks.

Fig. 3.4a shows the experimental configuration of the flux mapping method by taking radiative flux measurements for each radiation unit individually. A water-cooled Gardon type radiometer was employed to take irradiance flux measurements at the HFSS's focal plane, as shown in Fig. 3.4b. The TG1000-0 sensor, manufactured, calibrated and certificated by the Vatell company, can measure heat flux densities of up to 1.08 MW/m^2 with a calibration constant of 108.2 kW/m^2/mV and accuracy of ±3% [109]. The measured heat flux is proportional to the temperature difference between the center and the foil disk circumference (constantan), which is bonded to a cylindrical heat sink (made of copper). Previous studies have shown that Gardon gauges of this type may exhibit calibration errors when are used for measuring concentrated natural or simulated sunlight, specially up to 3500 kW/m^2, due to differences in the calibration blackbody source [110]. In this context, a comparison of the in-house calibration performed by CIEMAT and that of Vatell for concentrated solar irradiance measurements has shown an error agreement within the 3.6% for both calibrations [72,111]. Consequently, the sensor scale factor provided by Vatell is considered accurate enough for concentrated flux measurements in this study.

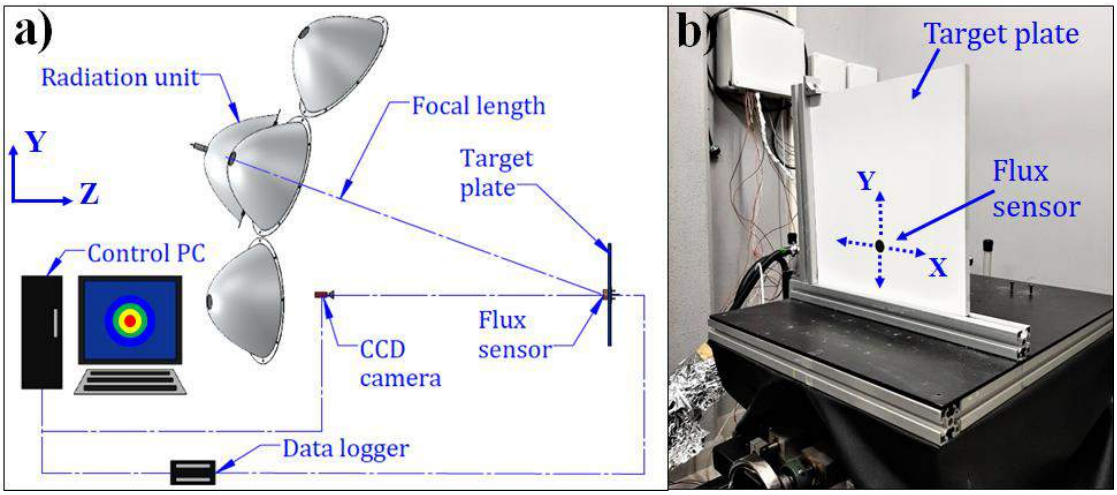

Fig. 3.4. a) Experimental setup of the indirect flux mapping method; b) heat flux sensor embedded on a flat target plate for generating the flux mapping.

A CR1000 data logger, ±0.06% analog voltage accuracy, from Campbell Scientific, was utilized to measure the output signal of the heat flux gauge. This flux gauge works by the principle of the thermopile that transmits a voltage signal proportional to the flux density over the sensor. In the data logger, this voltage signal is converted into kW/m^2 by means of the calibration factor provided by the manufacturer. Furthermore, a 406.4 × 406.4 mm AA-6061-T651 aluminum plate,

with 12.7 mm thickness, was used as a Lambertian target to record images of the flux spot concentrated over its surface. This plate was covered with a high temperature resistant white matte commercial coating (650 °C), Comex® [112] for diffusely reflecting the light concentrated on the target, and was combined with the Gardon gauge for taking flux measurements. A three-axes dynamic test bench with displacing error of ±1 mm was utilized to displace the target for taking measurements with the heat flux sensor.

A CCD camera, Allied Vision AVT-MK5054, 12-bit depth, with 1292×964 pixel resolution, was used to capture images of the concentrated flux on the target. In order to attenuate the bright of the concentrated light for avoiding saturation, the camera was set with an HR Varifocal Zoom Lens ½", and filters for this purpose. The camera was located with its optical axis parallel to the normal of the target, 2240 mm in front of it, avoiding perspective corrections for this position, see Fig. 3.4a. The sensor cell of the CCD camera has dimensions of 3.75 μm x 3.75 μm giving a target resolution of 0.4 mm at the focal plane. The camera was set in monochrome mode with an average exposition time between 20-40 ms, depending on the peak flux level of the lamp-reflector unit under characterization. In this way, the grayscale value is kept at 78% of the maximum level (255) for capturing the flux spot of the 7 lamps separately and avoiding overexposure. To calculate the flux maps, 30 images per flux map were recorded and averaged for obtaining a more accurate flux characterization, as reported in [113]. The images were taken after the lamps reached steady output for avoiding flux fluctuations (≥10 minutes). The dark current was also measured by recording unexposed images, and was subtracted from the averaged grayscale image. The grayscale image, which is the base of the flux map, was obtained with Eq. (3.9); where $Pix_{(i,j)}$ is the averaged grayscale pixel value in the *(i,j)* position; $pix_{i,j}$ is the grayscale value from the n^{th} image; *N* is the number of recorded images; and I_{dark} is the dark current.

$$Pix_{(i,j)} = \left[\frac{1}{N}\sum_{n=1}^{N} pix_{i,j}\right] - I_{dark} \tag{3.9}$$

By relating the intensity level of pixels and the measured radiative flux, the flux maps were obtained implementing the Eq. (3.10); where $Q_{(i,j)}$ is the radiative flux on the target, $q_{(x,y)}$ is the flux measured in the focal plane, $Pix_{(i,j)}$ is obtained from Eq. (3.9) and M_{pix} is the maximum grayscale pixel value in the averaged image.

$$Q_{(i,j)} = \frac{1}{M_{pix}} \sum_{1}^{i} \sum_{1}^{j} q_{(x,y)} * Pix_{(i,j)} \tag{3.10}$$

By quantifying the flux distribution on the target, the mean flux can be obtained and then used to calculate the electrical to radiative conversion efficiency described by the Eq. (3.11) [30]; where $\overline{q}$ is the mean radiative flux, A_{tg} is the flux spot area on the target and their multiplication provides the intercepted radiative power; I_{lamp} and V_{lamp} are the electric current and voltage that energize the lamps (2.5 kW_e per lamp).

$$\eta_{elc} = \frac{\overline{q} * A_{tg}}{I_{lamp} * V_{lamp}} \tag{3.11}$$

In this study, each of the radiation units (lamp-reflector units) is characterized individually and the total flux map is presented as the algebraic sum (superposition) of the individual flux maps. The reason for adopting this approach is that the target plate is not water-cooled, so it can reach high temperature levels when more than one radiation unit is used simultaneously. This can lead to the emission of radiation, introducing more uncertainties in the measurements. This superposing flux mapping approach has been widely reported and validated with an agreement of 99.97% [50,108]. The validation of this assumption (radiative flux additivity) will be reported in Section 3.5.2.1.

3.3.2 Uncertainty analysis

In order to ensure high accuracy in the implemented flux measurement technique, an uncertainty analysis was conducted for this purpose. For flux mapping calculation, there are three main error sources to take into consideration; the target properties, the heat flux gauge accuracy, and the camera resolution. Typically, spatial errors associated with the target properties are mainly due to the unevenness of the surface, the applied reflective coating, as well as the alignment of the target. Then, the non-uniformity of the reflected light can introduce uncertainties caused by different view angles. In this study, the view angle of the diffusively reflecting flat target plate is considered relative to the view angle of the camera, because the camera is installed with the normal of its sensor parallel to the normal of the plate. Therefore, errors due to the view angle are not considered. On the other hand, the displacement of the linear bench along the horizontal ($\pm$1 mm) and vertical length ($\pm$1 mm) for a target movement within 200 mm introduces an alignment error of 1% for both vertical and horizontal displacements. Therefore, the error for the target alignment is estimated in 2%.

The Gardon sensor has an accuracy of ±3% provided by the manufacturer Vatell. As aforementioned, a comparison of the in-house calibration performed by CIEMAT and that of Vatell for concentrated solar irradiance measurements has shown an error agreement within the 3.6% for both calibrations, as discussed in [72,111]. Therefore, the sensor scale factor of ±3% is considered for the flux measurements in this study.

The CCD camera was calibrated taking into account the optics and exposition times, so; neither glints nor random reflected beams were observed. Hence, for the applied optical filters and lens, it is assumed that the spatial relation from pixels to millimeters is not affected as long as the light entering the camera sensor arrives approximately parallel to the normal of the optics surface [108]. Furthermore, both the intrinsic noise of the camera sensor (chip temperature) and the light not delivered by the lamps are removed by taking into consideration the dark current, as explained in Eq. (3.9). Moreover, to ensure a linear chip response, flux measurements were taken at different locations of the flux spot and were compared with the pixel intensity levels for the same exposition time. Fig. 3.5 shows the comparison between radiative flux measurements and grayscale values presenting an agreement within an average error of 1.5% for a peak flux level of 420 $\mathrm{kW/m^2}$. In addition, the non-uniformity of the flux distribution, caused by flux oscillations and transient change of light, is reduced by taking a large number of images of the brightness spot on the plate, as explained in section 3.3.1 [113]. However, a non-uniformity error of 1.2% was estimated because the discretization of the active area of the sensor (25.4 mm) influences the conversion of the pixels into flux intercepted by the target over the analyzed area.

The known dimensions of the target plate and the Gardon sensor introduce uncertainties when they are related to the digital image for generating the coordinate system for the flux mapping. Accordingly, the scale factor error for the target area was calculated by analyzing the nominal distance of interest to the pixel size of an enlarged control image [114]. In this study, a line of 200 mm represents the nominal distance with uncertainty of ± 1 mm, leading to a relative error of 0.5%. Taking into account the horizontal and vertical axes, the total relative error leads to 1%. Besides, the pixel error for the scale factor is estimated in ± 0.5 pixel, and the nominal distance is covered by 377 pixels, resulting in a relative error of 0.13%. Therefore, the total relative error is estimated in 0.26%. By combining the error propagation, the scale factor error is estimated in 1%. Table 3.1

depicts the main sources of errors and the total error propagation calculated by the square root of the sum of the squares of the relative errors [115].

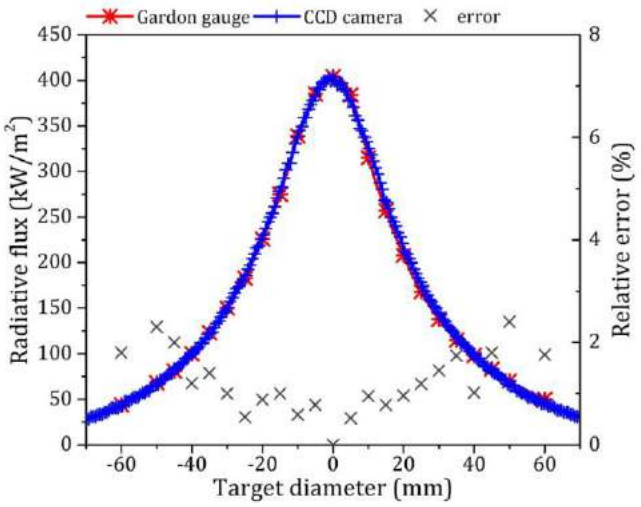

Fig. 3.5. Comparison between the flux measurements taken with the Gardon gauge and the grayscale values obtained by calibrating the CCD camera.

Table 3.1 Error sources introduced in the characterization technique.

Error source	Errors introduced in the flux mapping
Target properties and alignment	2%
Heat flux measurements	3%
CCD camera:	
Linearity	1.5%
Uniformity	1.2%
Scale factor for the target area	1%
Total	4.4%

3.3.3 Thermal analysis

Since the solar simulator is intended for use in low-to-medium and medium-to-high temperature applications, a temperature experiment was conducted by implementing only the central radiation unit for demonstrating the attainable thermal capability with a high temperature commercial paint. The testing material, a 12.7×304.8×304.8 mm carbon steel plate positioned at the focal point, was covered with a high temperature resistant (650 °C) black matte paint, Comex® [116]. Furthermore, an OPT-PI400, 382×288 pixel resolution, thermographic camera by Optris®, was utilized to measure the heat distribution. The IR camera was calibrated in advance by setting the emissivity of the material under analysis. Measurements on the testing plate were taken with calibrated Type-

K thermocouples (0.75% error) and served as a reference to adjust the configuration of the camera. Flux measurements from the Gardon gauge were also used for calibration due to the fact that thermal radiation from the bulb could introduce uncertainties to the measurements with the thermographic camera. It was noticed that when the lamp is turn off after the experimentation time the flux drops quickly from 200 ± 6 to 40 ± 1.2 $\mathrm{kW/m^2}$ in 5 s approximately, and stops completely after 80 s. In that interval, an average flux of 2.5 ± 0.1 $\mathrm{kW/m^2}$ was measured, representing the heat emitted by the bulb and electrodes. This represents the 1.25% of the total radiative flux; so, the thermal contributions of the light source elements are quite low. Therefore, the calibration factor of the camera was estimated in 1.5%, by taking the square root of the sum of the squares of individual uncertainties. The thermographic camera was located 2000 mm in front of the carbon steel plate.

3.4 Results and discussions

3.4.1 Ray quantity dependence

A ray-tracing analysis was carried out to estimate the proper ray number to provide not only sufficient accuracy but also minimum calculation cost. The ray quantity dependence analysis was performed by tracing rays for a single lamp-reflector unit in a range from $0.1x10^6$ rays to $4x10^6$ rays. Fig. 3.6a shows the normalized flux distribution obtained with the different quantity of launched rays. It can be appreciated that a high degree of convergence is reached after $1x10^6$ rays. However, the computational cost increases considerably when using a ray number up to $4x10^6$. Considering 4 million of rays as the best option, the relative error was calculated to determine the amount of rays that confers accuracy to the model and at the same time a fast convergence solution. From Fig. 3.6b it can be seen that the relative error is already within 2.5% for $2x10^6$ rays, so the accuracy improvement by increasing the ray number from $2x10^6$ rays to $4x10^6$ rays is very limited. Furthermore, considering that the solar simulator design counts with 7 lamps, a high number of rays would involve a relatively high computational cost. Therefore, the simulations were run with $2x10^6$ rays per lamp, which can offer a good balance in accuracy and computational cost.

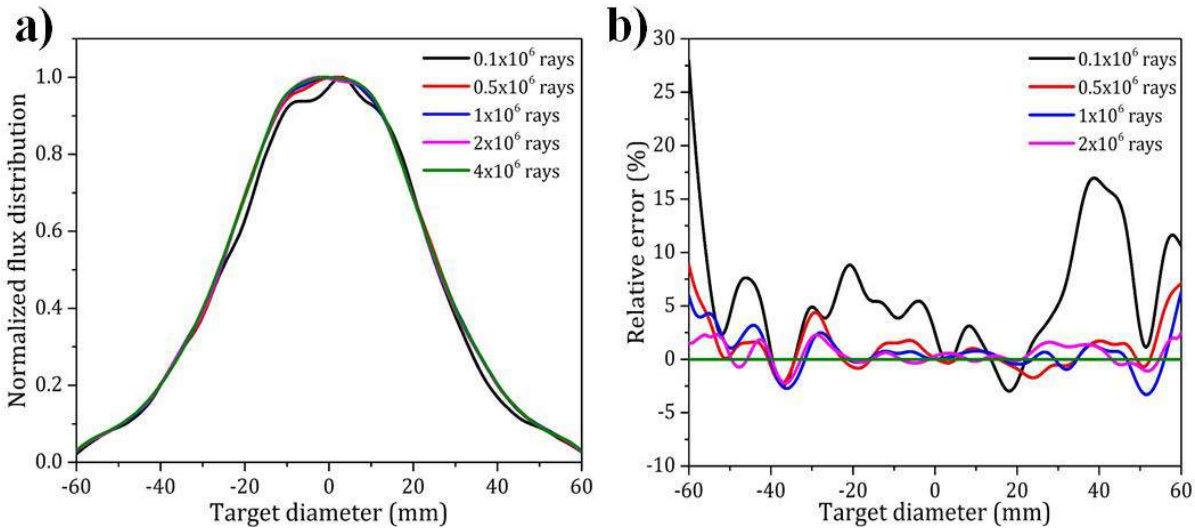

Fig. 3.6. a) convergence of the ray-tracing analysis when the number of rays is increased from $0.1x10^6$ to $4x10^6$ rays; b) relative error with respect to the best option of $4x10^6$ rays.

3.4.2 Analysis of the lamp-reflector design

Fig. 3.7a shows the variation of the eccentricity *e* as a function of the truncation angle α_c in a range of 25-75°, for different truncation radii R_{in} in a range of 175-325 mm. It can be observed that the lower the truncation angle and radius, the higher the eccentricity, reaching an eccentricity of 0.976 for angle and radius of 25° and 175mm, respectively. By increasing the truncation angle for a fixed truncation radius, the eccentricity presents an almost linear reduction until reaching the lowest value of 0.877 within the analyzed ranges. Fig. 3.7b shows the different estimated values of radiative transfer efficiency η as a function of the truncation angle and the truncation radius. It can be appreciated that an increment in transfer efficiency occurs between 25-55° for all truncation radii, and above this range, the efficiency is reduced. Furthermore, it can be seen that lower values of transfer efficiency are obtained with lower truncation radii. As reported in [29], having a low eccentricity of the ellipse, a short focal length, as well as large concentrator's diameter and large truncation angle, higher radiative transfer can be achieved, although, at the expense of having less surface area for reflecting more light beams. Consequently, a trade-off has to be made between the radiant energy intercepted by the reflector surface and the flux at the target. One reason for not obtaining higher transfer efficiencies with a larger truncation radius could be that the focal length was established at 2000 mm as the first design parameter, generating a restriction for the other parameters. Based on the sensitivity flux analysis, an ellipsoidal concentrator with truncation angle $\alpha_c = 55°$, truncation radius $R_{in} = 275$ mm, eccentricity e of 0.918, semi-major and minor axes

of 1082.25 mm and 413 mm, respectively and concentrator height of 274 mm, were selected in order to achieve the highest transfer efficiency of η = 42%. Fig. 3.8a shows the CAD design of the truncated ellipsoidal reflector selected from the ray-tracing analysis and Fig. 3.8b shows the HFSS designed with seven lamp-reflector units, a movable testing bench, and a shutter for regulating the level of the concentrated flux delivered onto the target. The implementation of the shutter will be explained in detail in Chapter 4.

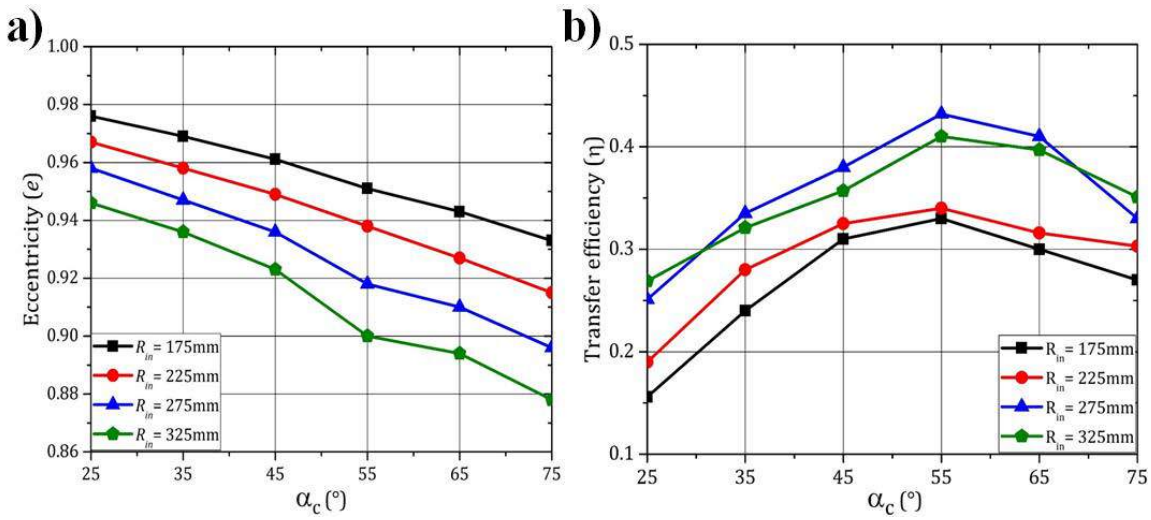

Fig. 3.7. Analysis of the ellipsoidal reflector design as a function of the truncation angle α_c and truncation radius R_{in} : a) analysis of eccentricity; b) analysis of transfer efficiency.

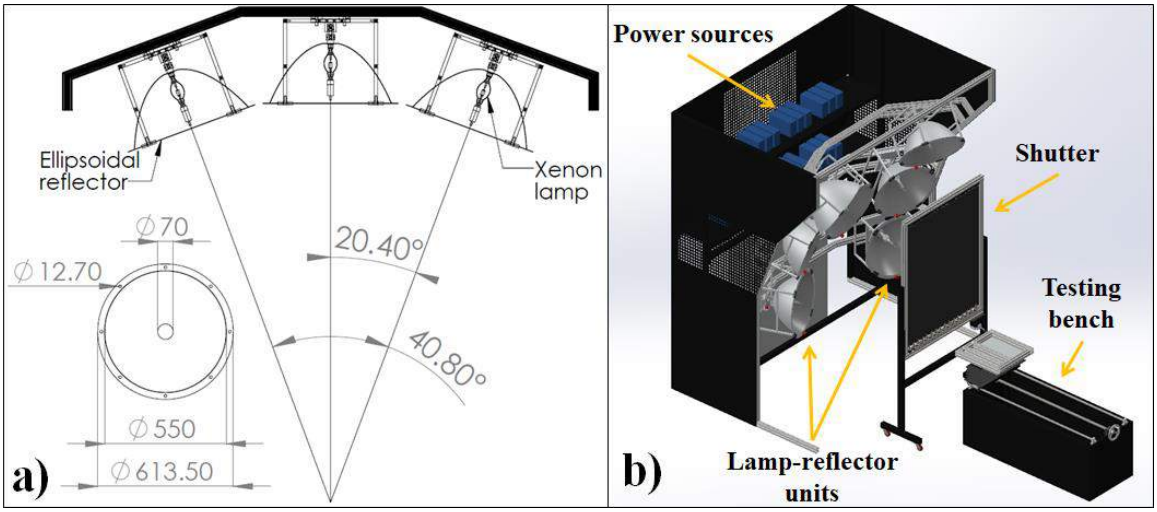

Fig 3.8. a) Layout of the ellipsoidal concentrators designed with the MCRT method (units in millimeters); b) complete HFSS design along with the shutter and the test bench.

3.4.3 Analysis of the flux characteristics of the HFSS design

As aforementioned, the optical performances of the designed HFSS were carried out with the aid of the software TracePro by launching 2 million of rays per run for a single lamp and configuring the reflectivity factor at 94% in order to determine the maximum achievable performance. Fig. 3.9 shows the flux distributions estimated with the ray-tracing analysis for each individual lamp. Fig. 3.9a describes the flux distribution of the central lamp, defined as the number 1, see Fig. 3.2. This radiation unit reaches a theoretical peak flux of about 254 $\mathrm{kW/m^2}$ with a radiative power of 820 W over a target diameter of 120 mm. The lamp-reflector unit number 6 (Fig. 3.9f) reaches the highest peak flux of up to 258 $\mathrm{kW/m^2}$ with an incident power over the target of about 833 W. Units number 2, 3, 4, 5, and 7 reach theoretical flux peaks of 215, 219, 243, 244, and 257 $\mathrm{kW/m^2}$, shown in Fig. 3.9b, c, d, e, and g, respectively. The algebraic sum of the individual flux peaks and the radiative power are estimated as 1690 $\mathrm{kW/m^2}$ and 5857 W, respectively.

Fig. 3.10a shows the predicted flux distribution when all the 7 lamp-reflector units are modeled and Fig. 3.10b shows the flux profiles of the vertical and horizontal distribution over the target. Accordingly, the estimated peak flux reaches 1690 $\mathrm{kW/m^2}$ and a total power of 5858 W over a target diameter of 120 mm. In order to reduce the computational cost, the ray number was set to $1.5x10^6$ rays per lamp when the 7 lamps were analyzed together (Fig. 3.10). The relative error between the algebraic sum of the individual radiation units and the total peak flux predicted with the 7 lamps together is about 0% for the peak flux and 0.02% for the intercepted power. This outcome implies that either a ray number of $1.5x10^6$ or the algebraic sum of the radiative flux per lamp can be applied when the system is analyzed with all the lamps together (additive assumption). By applying the Eq. (3.11), the theoretical electrical-to-radiative conversion efficiency is estimated as 33.5% for the designed HFSS.

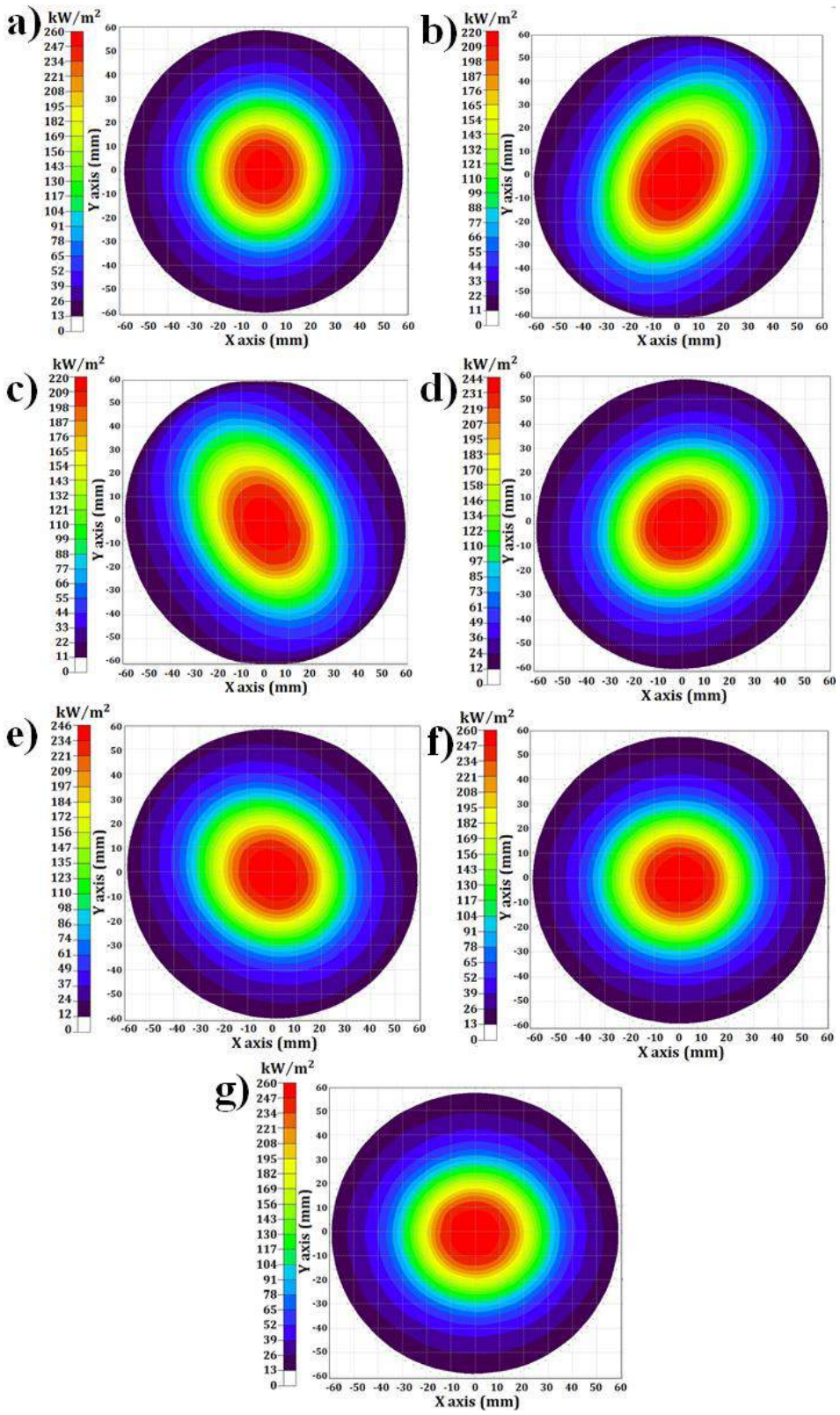

Fig. 3.9. Predicted flux maps of the lamp-reflector units: a) unit 1 (central); b) unit 2; c) unit 3; d) unit 4; e) unit 5; f) unit 6; g) unit 7.

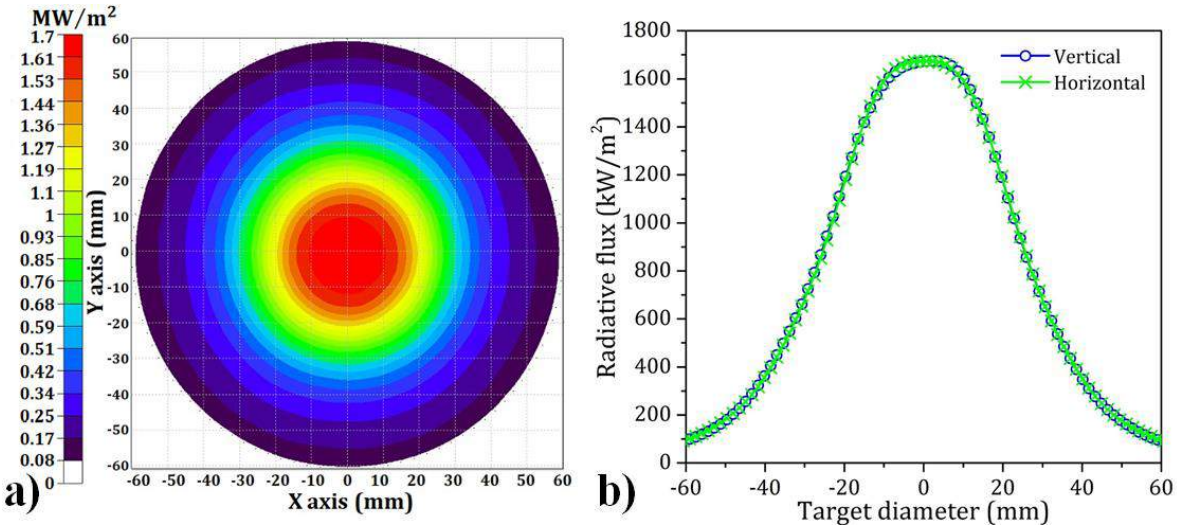

Fig. 3.10. a) Total radiative flux distribution with a peak of 1690 kW/m^2 on a target diameter of 120 mm; b) Flux distribution profiles along the horizontal and vertical position over the target.

3.5 Construction and characterization of the HFSS

3.5.1 Construction

The Centro de Investigaciones en Optica, A.C. (CIO), campus Aguascalientes, in collaboration with Solara Industries, S. A. of C. V., have designed and built a high flux solar simulator for solar-thermal and thermochemical research. Fig. 3.11 shows this facility composed of seven xenon short arc lamps coupled with aluminum reflectors, a dynamic test bench, and a shutter curtain. This facility was installed at the Laboratorio de Innovación y Caracterización de Sistemas Termosolares y Fotovoltaicos (LICS-TF), in the solar-thermal laboratory.

The HFSS utilizes 2.5 kW_e xenon short arc lamps, ozone-free (XBO®2500 W/HS) with a bulb diameter of 60 mm and an electrode gap of 5.5 mm [117]. In order to power a single xenon arc lamp, an array of three lamp power supplies connected in parallel were implemented; where a rated input voltage of 220 VAC single phase per power supply was required. The rated output current and voltage that the power supply array can provide is about 90 A and 28 V, respectively, so achieving the electrical input power of 2.5 kW_e per lamp. Furthermore, custom-made ellipsoidal reflectors have been fabricated by molded aluminum and have been polished on their internal surfaces to achieve high reflectivity. This particular lightweight reflector (~1 kg) offers high resistance to attrition and corrosion owing to its anodized finish. In order to cool the lamp-reflector units and prevent damage due to overheating, a set of 3 blowers were employed; 1 blower that

offers a rate of fresh air of up to 43 m^3/hr and two blowers of 32 m^3/hr. These blowers were connected to air distributors for dividing the mass flow rate of air to the lamp-reflector units equally. For security, the cooling system is turned on automatically when the lamps are triggered by the user.

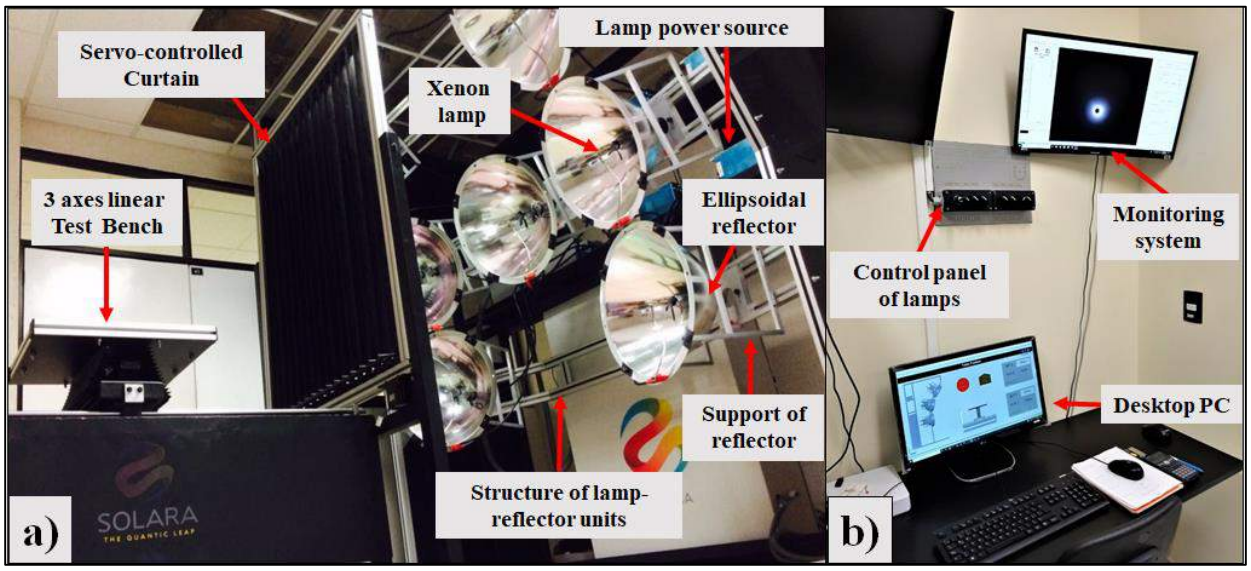

Fig. 3.11. a) Photograph of the 17.5 kW_e HFSS developed at the optical research center (CIO, Spanish acronym); b) control panel and desktop PC for controlling and monitoring the HFSS.

The structure that supports the lamp-reflector units is made of a 45 mm × 45 mm extruded-anodized aluminum profile. The secondary support is fabricated with 50.8 mm × 50.8 mm RHS (Rectangular Hollow Sections) steel with epoxy paint finish. The supports of concentrators are based on of machined-anodized aluminum AA-6061. The supports of the bulbs are manufactured with machined steel D2 covered in black oxide, which is produced by the chemical oxidation of steel. Black oxide offers a dark layer that adds corrosion resistance and reduces light reflection. 50.8 mm × 50.8 mm RHS steel was utilized to manufacture the 3-axes linear testing bench with epoxy paint finish. It is assembled by 45 mm × 45mm extruded aluminum profile anodized finish.

The housing of the bench is a black sheet gauge 14, epoxy paint finish. The shutter is fabricated with a 50.8 mm × 50.8mm RHS steel structure epoxy paint finish. Besides, axes and supports of the shutter were manufactured with D2 machined steel, in a black oxide finish. Both, the bench and the shutter are depicted in Fig. 3.11a. The frame that contains the shutter is a 45 mm × 45 mm

extruded aluminum profile with an anodized finish and the slats are constructed with 1/8” steel plate gauge with a black oxide finish.

The HFSS is installed inside an enclosure which consist in double sheetrock-based walls and concrete walls for housing the system and prevent damage to both, researchers and sophisticated equipment (high-discharge arc lamps). The enclosure is equipped with an air conditioning system and a ventilation system for regulating the temperature and extracting gases. Besides, a specialized electrical transformer box is installed behind the solar simulator for energizing the lamps.

The solar simulator can be effectively controlled from the outside of the HFSS housing by means of a control panel and a desktop PC, as depicted in Fig. 3.11b. The desktop PC is utilized to control the system units (lamps, blowers) and acquiring experimental data (flux measurements). Furthermore, a control panel located above the PC is implemented to manually turn on the blowers with a control key and turn on-off the lamps of the solar simulator. In addition, a computer monitor is installed for observing the flux distribution delivered by the solar simulator on the samples under test, see Fig. 3.11b. For turning the lamps on-off, opening-closing the SC and displacing the 3-axes linear bench, a data acquisition system was also developed based on National Instruments LabVIEW software with a NI-CompactDAQ-9178.

Fig. 3.12a shows the control system of the lamps, blowers and the shutter curtain where the number of required lamps can be turned on-off and the SC can be activated. Moreover, a CR1000 data logger (Campbell Scientific), ±0.06% analog voltage accuracy, ±3 min. per year real-time clock accuracy, was employed for data storage and control of the measurement instruments such as the Gardon gauge. The software Loggernet was utilized for collecting flux and temperature data from the experiments, as well as for controlling the shutter and the linear bench, as depicted in Fig. 3.12b. In this form, the flux gauge can be moved along the focal plane for taking measurements.

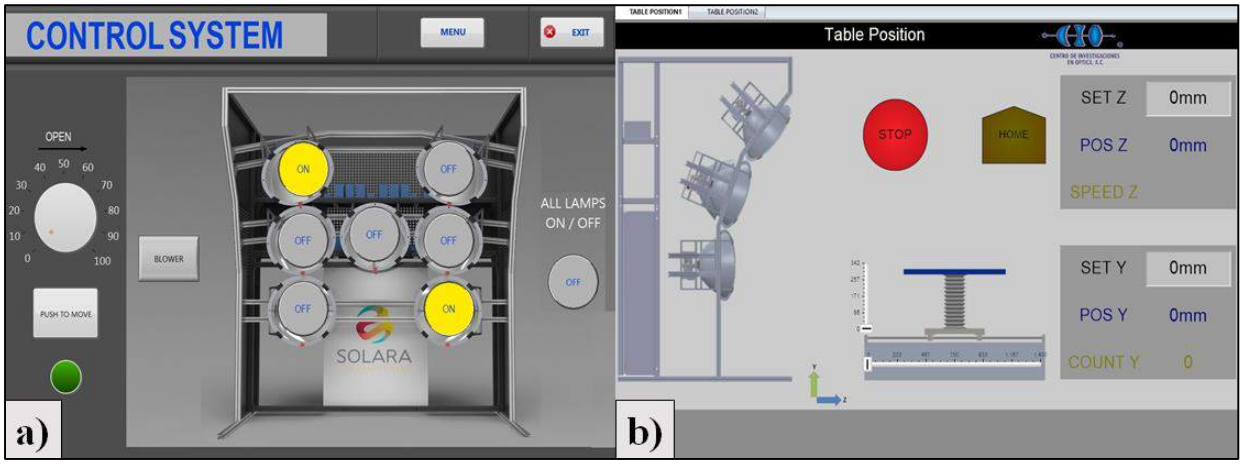

Fig. 3.12. a) Screenshot of the HFSS control system for turning the lamps on-off; b) control system for data storage and control of the linear bench.

3.5.2 Characterization of the HFSS

Once the solar simulator has been constructed, the reflectivity factor that the ellipsoidal reflectors provide was firstly measured with a UV–VIS-NIR Cary 5000 spectrophotometer, wavelength range of 175–3300 nm. Accordingly, an average reflectivity of approximatelly 80% was measured on the concentrator's surface. This level of specular reflectivity is thought to be reasonable considering that a reflective coating layer was not applied. According to the publised literature, this kind of coating has a high risk for cracking and detachment from the surface due to the high thermal load [48]. In this study, claiming for benefits in durability and resistance, a polished solid aluminum concentrator was selected, which reflectance is sufficient to conduct the desired experimentation. It is also light-weight (facilitating manipulation) and offers great resistance to corrosion and overheating, making this concentrator a suitable option to performe high concentrated flux testing with low maintenance and high durability.

In order to characterize the solar simulator, radiative flux measurements were taken with the heat flux gauge at the focal plane of the facility. Fig. 3.13a shows the maximum peak flux measured from each radiation unit individually in a lapse of 10 minutes (600 s). It can be observed that the measurements exhibit weak flux oscillations at the start-up of the lamps, which begin to stabilize after ~300 s, according to these results. These oscillations occur due to the reactions of the electrical discharge in the xenon gas and the stabilization of the power supply as well. After 7 minutes, the lamps reach the 95% of the final output value, achieving a quite steady flux output

after this warm-up lapse. From Fig. 3.13a, it can be clearly observed that the radiation unit with the lowest peak flux is the unit #2, with a peak flux up to 152±7 kW/m^2, followed by the unit #3 with 170±7 kW/m^2. This is thought to happen because lamps 2 and 3 are located at the upper row of the solar simulator array, so the tilt angle with respect to the normal of the Gardon sensor is larger compared with the rest of the lamps. This inclination produces a larger distribution of the concentrated irradiance over the target plane, reducing the peak flux and increasing the spot. The highest peak flux was achieved by the lamp-reflector unit #6 with a peak flux up to 211±9 kW/m^2. From Fig. 3.13a, units 1, 4, 5 and 7 attained a peak flux of 210±9 kW/m^2, 189±8 kW/m^2, 200±9 kW/m^2 and 195±9 kW/m^2, respectively. In addition, the temporal instability of the radiative output was analyzed for each of the radiative units. Fig. 3.13b shows flux measurements of the radiation unit #7 during a time of 3 minutes (180 s) at two different positions; at the focal point of 195±9 kW/m^2 and at 10 mm away from the peak (145±6 kW/m^2). Measurements were taken each second after the lamps reached the steady output (720 seconds). It can be appreciated that the flux oscillations in the analyzed time are between 1-6.2 kW/m^2. The temporal instability can be calculated by implementing the Eq. (3.12) described by:

$$Temporal\ instability = \left|\frac{(I_{max} - I_{min})}{(I_{max} + I_{min})}\right| \times 100 \tag{3.12}$$

where I_{max} and I_{min} are the maximum and minimum irradiance measured on the selected point during the nominated time [55]. Based on this equation, the temporal instability is within ≤2%. Furhermore, for all the 7 lamp-reflector units, similar instabilities were measured, observing that; the lower the radiative flux, the higher the flux instability.

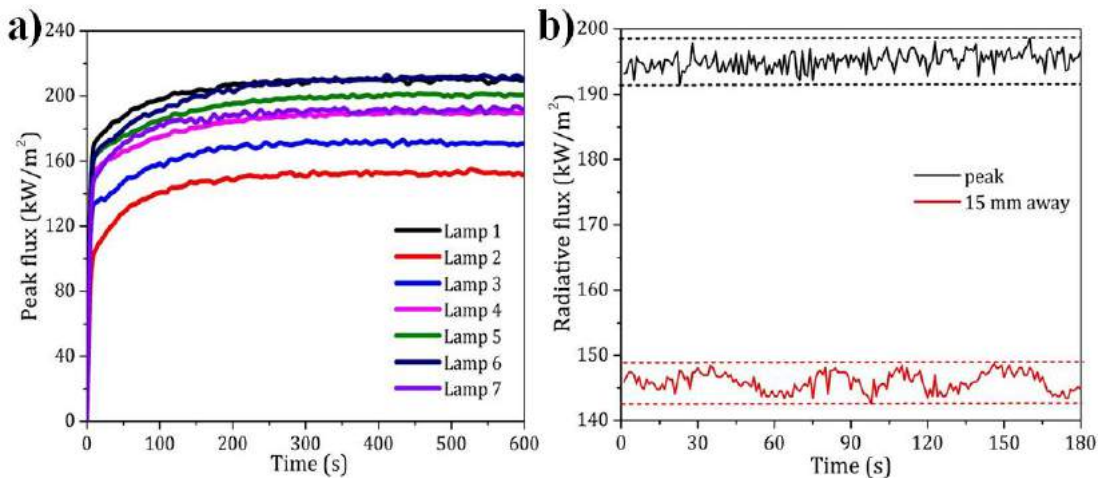

Fig. 3.13. a) Peak flux measured for each of the 7 radiative units at the focal plane; b) flux measurements in a span of 180 s with the lamp 7 for analyzing temporal flux oscillations after the lamp reached the steady output (720 s after).

3.5.2.1 Flux mapping technique

Individually, the radiative flux distribution of the lamp-reflector units was measured with the Gardon gauge along the focal plane in steps of 5 mm over a diameter of 120 mm. Subsequently, the target plate was positioned for capturing photographs of the concentrated irradiance. The use of the AVT-MK5054 CCD camera and the diffusively reflecting flat target plate allowed to obtain the flux map in mm, in accordance with the description presented in Section 3.3.1. Fig. 3.14 shows the flux maps of the 7 lamp-reflector units over a target area of 200 mm x 200 mm. From this results, each of the 7 lamp-reflector units achieve a mean flux ranging from 62-65.6 kW/m^2 with a radiative power between 701-742 W over a target diameter of 120 mm. Fig. 3.14b depicts the flux distribution with the lowest mean flux of about 62 ± 3 kW/m^2 and a total radiative power of 701 ± 30 W over a target diameter of 120 mm. As aforementioned, the effect of the incident angle with respect to the normal of the focal plane is a reduction of impinging peak energy due to the distribution of the flux. Accordingly, when the lamps 2 and 3 hits the target, the flux spot results in a more spread distribution, generating a elliptical-like shape, as shown by the Fig. 3.14b and 3.14c, which is in accordance with the MCRT simulations (see Fig. 3.9b and 3.9c). The mean flux provided by the radiation units 1, 3, 4, 5, 6 and 7 are 65.4 ± 2.8 kW/m^2, 63.2 ± 2.7 kW/m^2, 65 ± 3 kW/m^2, 65.2 ± 2.8 kW/m^2, 65.6 ± 2.8 kW/m^2 and 65.4 ± 2.8 kW/m^2, respectively. In order to ensure that the radiative power output of each lamp have good response to the ray-tracing results, the electrical imput power of each lamp was measured, observing that the 7 lamps are energyzed

with an electrical input power in a range of 2.1 to 2.3 kW_e. Therefore, the total electrical input power is about 15.54 kW_e, resulting in 88% of the maximum input power for energyzing the lamps.

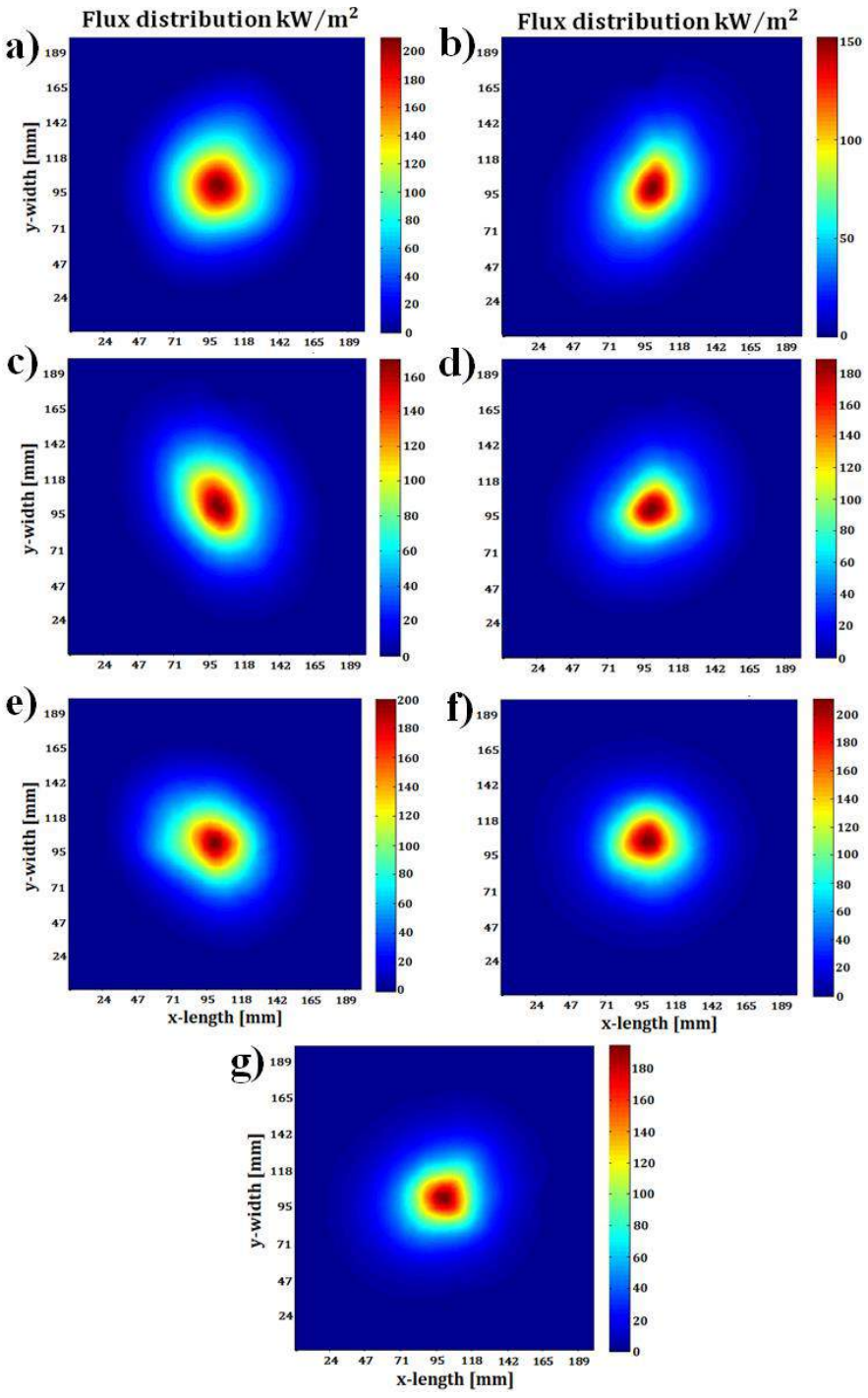

Fig. 3.14. Flux maps of the lamp-reflector units: a) unit 1 (central); b) unit 2; c) unit 3; d) unit 4; e) unit 5; f) unit 6; g) unit 7.

The flux maps obtained by the indirect flux mapping technique show quite similarity in distribution compared with the flux distributions predicted with the ray-tracing analysis, see Fig. 3.9. The main difference between simulations and measurements is clearly observed in the higher peak flux levels obtained by the MCRT method. This is attributed to the lower reflectivity factor offered by the manufactured concentrators of 80% compared to the 94% configured in the simulations.

In order to analyze the level of agreement between simulations and measurements, the MCRT technique was implemented adjusting the reflectivity factor to 80%, similar to that exhibited physically by the concentrators. Table 3.2 shows the comparison between both simulations and experimental results having a reflectivity factor of 80%. It is worth mentioning that the electrical input power configured for simulations was adjusted with that of the electrical input power measured for energizing each of the lamps. Besides, the radiative power from the arc emitters was kept at 50% of the radiant power for simulations as explained in section 3.1.2.

Table 3.2. Comparison of the radiative flux characteristics between simulations and experimental results with a reflectivity factor of 80%.

Lamp reflector unit	Measurements (80% reflectivity)		Measured electric input power kW_e	Electrical-to-radiative conversion efficiency η_{e-r} (%)	Simulations (80% reflectivity)		Relative error between peak flux (%)
	Peak flux (kW/m^2)	Power (W)			Peak flux (kW/m^2)	Power (W)	
1	210±9	740±32	2.25	32.8	209	725	0.5
2	152±7	701±30	2.24	31.3	160	679	5
3	170±7	715±31	2.2	32.5	162	680	5.8
4	189±8	736±32	2.3	32	196	710	3.5
5	200±9	738±32	2.15	34.3	198	710	1
6	211±9	742±33	2.25	33	212	730	0.5
7	195±9	740±32	2.15	34.4	211	725	7.5
Total	1327±58	5112±226	15.54	32.9	1348	4959	1.5% (from total)

From Table 3.2, it can be observed that the electrical to radiative conversion efficiency calculated with the Eq. (3.11) ranges from 31.3% to 34.4% over a target diameter of 120 mm, which is in accordance with simulations at 80% reflectivity. Furthermore, the peak flux in both, simulations (80% reflectivity) and experimental measurements have good agreement for lamp-reflector units 1, 5, and 6 with a relative error within 0.5-1%. On the other hand, a disagreement occurs for the lamp-reflector units 2, 3, and 7, with a relative error in peak flux of about 5%, 5.8%, and 7.5%, respectively. The outcomes show that the peak flux of the lamp-reflector unit 2 is lower than simulations, while the intercepted power over the target diameter of 120 mm is higher in the same comparison. These inconsistencies are attributed to the fact that the radiative flux is focused on the target in such a way that the flux distribution has a higher level of concentrated energy in the middle and edges of the flux spot. This effect results in a lower peak flux, but with higher energy within the distribution area. This effect is observed in the lamp-reflector units 2, 4, and 7, where the peak flux is lower than the flux estimated by simulations, but the intercepted power is higher.

Fig. 3.15 shows the comparison of the flux distribution profile measured and simulated with the lamp-reflector unit 1. It can be clearly seen that the predicted flux distribution has a wider peak flux than the measured flux has, between 0 to 15 mm in radius. It can also be seen that the measured radiative flux is slightly wider than the estimated flux at a target radius between 30 to 60 mm. The full width at half maximum (FWHM) defines the radial distance from the center (peak flux) to the point at which the distribution drops to half its maximum value. From Fig. 3.14 the half width was calculated from measurements and simulations, obtaining a distance of 32 mm and 26 mm, respectively. Based on these results, it can be inferred that, the larger the half width, the more the intercepted power for the same target diameter; effect observed for all the lamp-reflector units. In addition, the relative error was calculated for both flux distributions, obtaining an error of 13% for a target diameter of 120 mm, 9% for a diameter of 100 mm, 6% for 80 mm and a relative error of 4% for a target diameter of 60 mm.

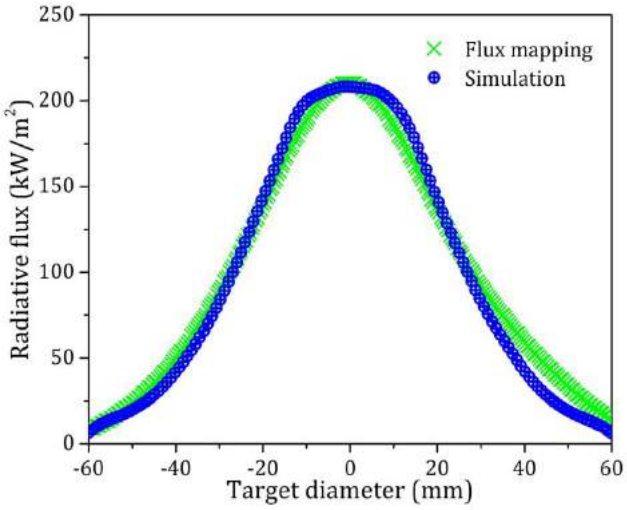

Fig. 3.15. Comparison between the experimental and theoretical flux distribution profile of the lamp-reflector unit 1 over a target diameter of 120 mm.

Disagreements between predicted radiative flux properties and measurements can also be generated by manufacturing and mechanical installation of the optical system. In this context, one of the main causes of discrepancies of theoretical and experimental results for solar simulators is the optical alignment of the arc emitter inside the reflector [108,113]. The alignment of the bulb on the focal point of the ellipse f_1 has a great influence in the final optical performance of the solar simulator. In order to align the whole radiative units with their flux spots onto the focal plane, the alignment of the central lamp-reflector unit (unit #1) is utilized for this purpose. Fig. 3.16a shows the flux distribution obtained with the radiation unit #1 when the bulb is moved (manually) 2 ± 0.5 mm away from the ideal position and Fig. 3.16b shows the flux distribution when the bulb is adjusted at the designed location of f_1. As a result of the displacement of the bulb 2 mm from the focal point, the peak flux is reduced up to 162 ± 7 kW/m^2 (48 kW/m^2 lower) and the intercepted power is also diminished up to 540 ± 23 W (25% less power). It is worth mentioning that the alignment of the xenon lamps inside the reflectors was carried out manually, which implies that the optical performance of the solar simulator can be improved; for instance, by implementing a precisely alignment system driven by a stepping motor [64].

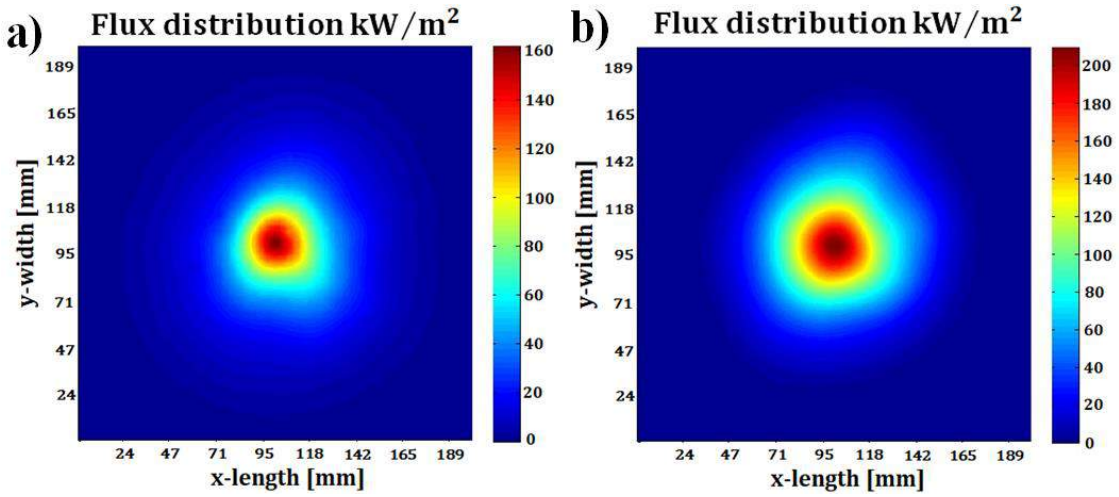

Fig. 3.16. a) Flux distribution of the central radiation unit (#1) when the bulb is moved 2 mm away from the ideal position; b) flux distribution when the bulb is adjusted at the designed location.

In order to demonstrate the additivity of the individual flux maps described in section 3.3.1, radiative flux measurements were taken with pairs of radiation units together and by superimposing flux maps of individual units. Table 3.3 depicts the comparison of radiative flux by measuring radiation units together and by summing two single radiation units. It can be observed that the flux reached with a pair of units leads to the same result by doing the algebraic sum. In addition, the relative error between the superposed and measured flux is within the repeatability of the implemented technique (95.6% bounds). Therefore, this results validate the implemented superposing flux mapping approach.

Table 3.3 Comparison between the superposed and measured flux for the validation of the superposing flux mapping approach.

Radiation units (#)	Superimposing(kW/m^2)	Together (kW/m^2)	Error (%)
1-7	405	410	1.24
2-4	341	344	0.87
5-6	406	411	1.22

Fig. 3.17 shows the flux map produced by superimposing individual radiation unit measurements demonstrating the flux delivered on the focal plane when the 7 lamp-reflector units are employed. Fig. 3.17a depicts the map of the irradiance distribution over a target area with dimensions of 200 mm x 200 mm, delivering a total peak flux of 1327 ± 58 kW/m^2. It can be observed that the flux distribution on the target is highly axisymmetric, which agrees with the results obtained from the ray-tracing analysis. Fig. 3.17b shows the horizontal and vertical flux distribution profiles over a

120 mm target diameter. As a final result, the complete facility is capable of delivering an average flux density of 455±20 kW/m^2 with a radiative power of 5.14±0.22 kW intercepted within a target diameter of 120 mm. Accordingly, the total mean flux level corresponds to a theoretical black body stagnation temperature of approximately 1680 K ($\overline{q} = \sigma {T_b}^4$). This value is the maximum theoretical temperature that a blackbody receiver would reach for a given flux input with no losses [108]. By applying Eq. (3.11), the electrical-to-radiative conversion efficiency was calculated at 33% by using the total input electrical power data measured from the energy sources of 15.54 kW_e.

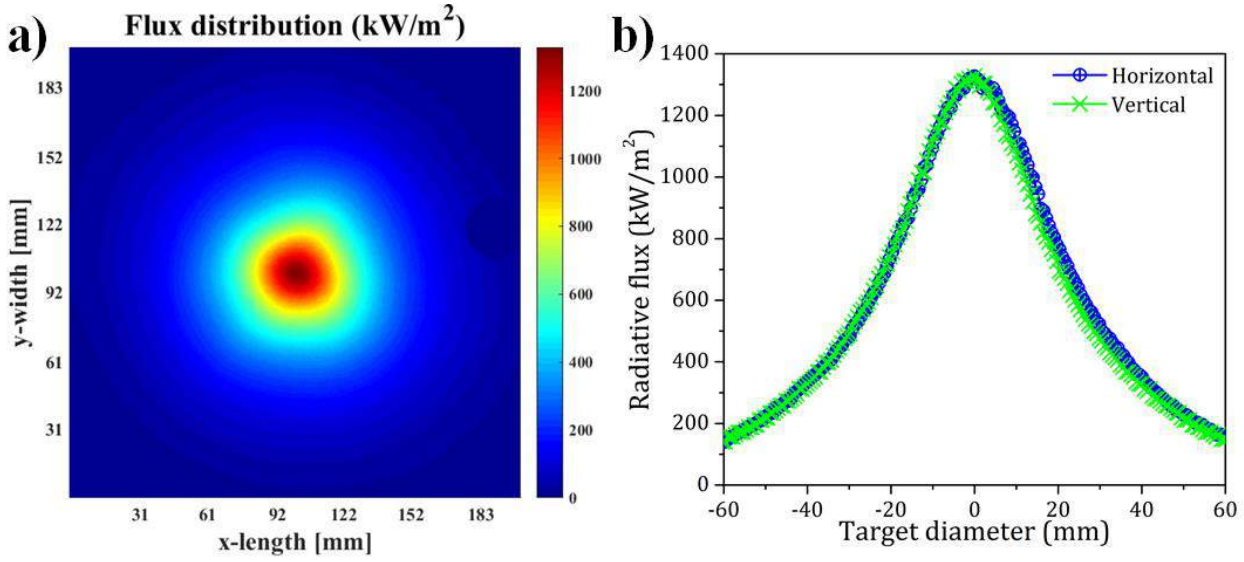

Fig. 3.17. a) Total flux map of the developed HFSS over a target area of 200 mm x 200 mm, delivering a total peak flux of 1327±58 kW/m^2; b) horizontal and vertical flux distribution profiles showing high symmetry on both axes.

3.5.2.2 Thermal measurement

To demonstrate the attainable thermal capability with a high temperature commercial paint, a heat flux experiment was conducted by implementing only the central radiation unit (#1) irradiating a carbon steel plate with a peak flux of 210±9 kW/m^2, as explained in section 3.3.3. In this case, only a single radiation unit was used in order to avoid saturation or damage to the thermographic camera sensor. Furthermore, this thermographic camera was implemented due to the fact that it is a more versatile method for measuring temperature, finding variations and localizing hot spots in a robust manner than with the use of thermocouples. Fig. 3.18a shows the heat flux distribution over the carbon plate and Fig. 3.17b the temperature profile over 200 mm in length, respectively.

The results show a maximum measured temperature of approximately 480±7 °C over the carbon steel plate covered with a black matte paint. Furthermore, it can be appreciated that the temperature distribution has a Gaussian shape and the flux distribution does not present local "hot spots" over the plate. The measurement was taken 45 minutes after the lamp was turned on and the room temperature did not exceed 25 °C. Accordingly, it can be inferred that a single lamp-reflector unit can be used for low-medium temperature applications using a commercial thermal paint, which is in accordance with the application purposes of the designed system.

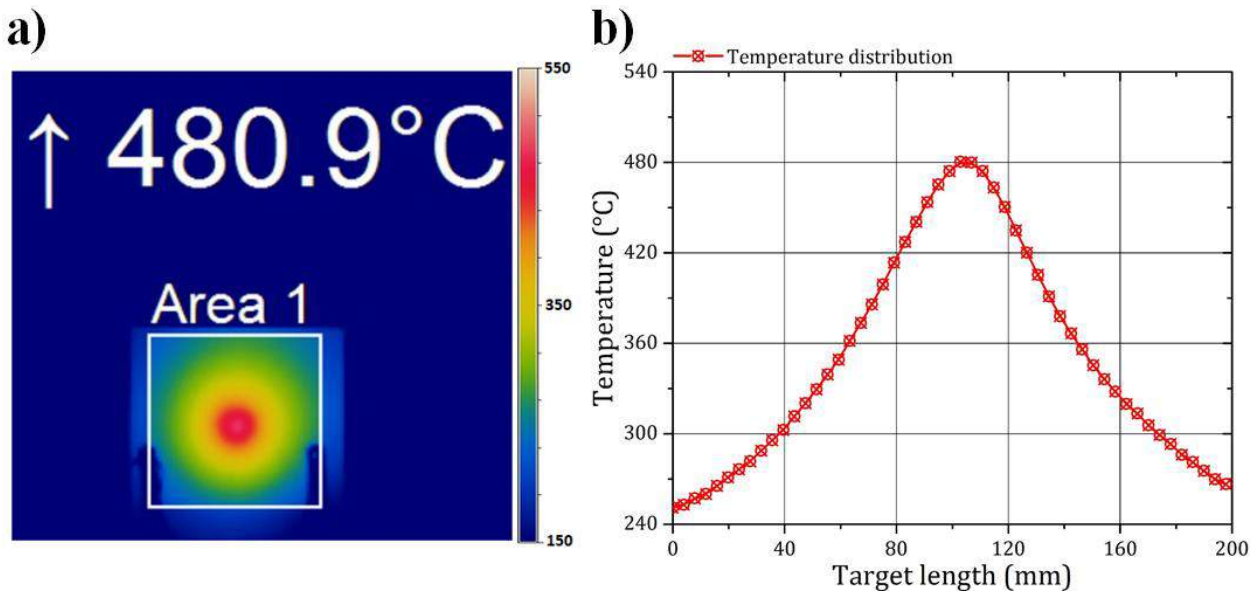

Fig. 3.18. Thermal analysis with a single radiation unit: a) Temperature distribution on a carbon steel plate covered with a black paint; b) temperature profile on a length of 200 mm, presenting a peak of about 480 °C.

3.6 Summary

In this Chapter, the design and characterization of a 17.5 kW_e HFSS has been reported. The design of the 7 xenon lamps solar simulator has been numerically analyzed through the MCRT method. In order to determine the best lamp-reflector assembly, the radiative transfer efficiency was optimized by modifying design parameters such as the reflector radius and eccentricity. As a result, the theoretical peak flux was predicted to achieve up to 1635 kW/m^2 with a total radiative power of approximately 6 kW over a target diameter of 120 mm, when a reflectivity factor of 94% (standard mirror) is employed. Based on the theoretical results, the construction of the HFSS was

carried out, presenting a technical report of the main components, instrumentation and acquisition systems used to fully control the facility in a remote manner.

The characterization of the HFSS was conducted by implementing the indirect flux mapping technique. For this methodology, a CCD camera and a water-cooled Gardon gauge embedded with a diffusely reflective target plate were utilized for obtaining the flux distribution delivered by the solar simulator on the focal plane. Therefore, a total peak flux of up to 1327 ± 58 kW/m^2 and a total mean flux of 452 ± 19 kW/m^2 was measured over a uniformly rounded spotlight distribution of 120 mm, having an intercepted radiative power of 5.11 ± 0.22 kW. This results validated experimentally the ray-tracing analysis and the assumption of additivity of the individual flux outputs as well. Furthermore, a temperature analysis was conducted by measuring with a thermographic camera and irradiating a target plate with single radiation unit. The temperature level achieved after 45 minutes was up to 480 ± 7 °C onto a carbon steel plate covered with a high-temperature resistant black paint. This measurement offers valuable information about the temperatures that can be achieved with one lamp-reflector unit when a commercial thermal paint is applied over a metallic substrate. The reported outcomes provide valuable information to determine how the equipment operates and opens possibilities for the advancement of different applications for concentrating solar-thermal energy, such as solar material testing and thermochemical processes.

Chapter 4. Radiative flux modulation of the HFSS

In the present Chapter, the optical design and optimization of different shutter curtains (SCs) is conducted in order to improve the flux regulation capabilities of the developed HFSS. The optimization in design is carried out by using an excellent MC ray-tracing software, TracePro. Predictions of the flux distributions are analyzed by modifying design parameters and shapes of SCs. Furthermore, experimental flux modulations when a flat shutter is used are presented for validation. Moreover, radiative flux measurements at the focal plane and further back the focal plane are also performed in order to modify the spot size and flux level. All the experiments have been conducted by utilizing a single radiation unit for detailed analysis.

4.1 Shutter curtain for flux modulation

In solar-thermal research, solar simulators must provide adjustable radiative flux in a controlled manner and in a wide range of intensities in order to achieve low-medium-high temperature levels for transferring into different testing materials [118]. Typically, rectifiers are employed to adjust the radiative flux delivered onto the receiver. The inconvenient with rectifiers is that the output power modulation is carried out by directly adjusting the power supply of the lamps [64]. This can lead to flux oscillations and instability due to variation of the electrical input power [119]. The flux resolution quality provided by the rectifiers is also conditioned by the lamp noise threshold current (80% of the maximum current), in which the plasma generated between the electrodes produces noise. This noise can highly affect the system design. In order to have a reliable rectifier, which can provide steady-state operating conditions of the lamp, highly sophisticated electrical circuits must be taken into consideration [120,121]. This method involves more complex and costly flux control systems, in which complexity, cost and maintenance increase greatly with the number of lamps available [33].

Alternatively, a multi-lamp HFSS can also regulate the flux level by turning on and off the number of required radiation units [50]. Nevertheless, if the flux level depends on the number of lamps turned on, the resolution would be conditioned by the number of units and by the flux output level that each lamp can deliver. In this study, different SCs are designed to mechanically regulate the radiative flux delivered by the solar simulator for providing a complete controllable indoor testing environment. The SCs are implemented in order to have a wide range of radiative flux levels, and as a result, avoiding the use of rectifiers. Accordingly, with well-controlled flux capabilities, a

wide variety of solar-thermal assessments can be conducted, such as: thermal fatigue failure by cyclic thermal loads, characterization of heat transfer performance in materials, solar reactor tests for solar fuel production, testing of solar selective absorber coatings, among others [16,94,113,118].

4.2 Geometry and physical model

4.2.1 Shutter curtain designs

The proposed SCs were coupled with the multi-lamp HFSS developed and described in the previous Chapter. This HFSS, comprised of seven radiation units, is arranged in a matrix configuration as illustrated in Fig. 3.2. This arrangement was chosen taking into consideration the shutter geometry. In this study, three different curtain designs were analyzed versus the flat SC fabricated by the company, Solara Industries, which was described in section 3.5.1. This flux modulation analysis is conducted in order to determine the suitable design that can provide an efficient flux regulation with the lowest radiative losses.

The manufactured SC has been designed with a rectangular shape by aluminum profiles with cross size of 45 mm × 45 mm contained in a structure made of 50.8 mm × 50.8 mm RHS steel. This flat shutter has dimensions of 2140 mm in height and 1168 mm in length, see Fig. 4.1a. This flat SC is comprised of 16 slats that are mechanically open and closed by a servomotor. The height, length and thickness of each slat are 1200 mm, 80 mm and 3 mm, respectively. Fig. 4.1b shows the SC number 2 which is designed with three sections; two tilted lateral sections and one flat central section. The lateral sections of this SC form an angle of 20.4° in order to align the normal vectors of these lateral sections to be pointing to the outermost columns of the radiation units. The dimensions of the SC2 are a height of 2380 mm and a width of 1330 mm. Furthermore, this shutter counts with 12 slats, 4 slats per section, and the height, length and thickness of each slat are 1500 mm, 105 mm and 3 mm, respectively. The SC3 has a similar geometry as the previous one, as shown in Fig. 4.1c. The main difference from the SC2, is that, in the SC3 the number of slats implemented in the lateral sections is seven and for the central section is six. In addition, the length of the slats is also modified from 105 mm (SC2) to 80.5 mm for the curtain 3. This is done in order to determine whether the number of slats and/or the gap between them can have a significant influence on the concentrated flux level that can be obstructed. Moreover, an individual SC, designed close-coupled with each radiation unit, is analyzed for optimizing the flux modulation

and reducing radiative losses due to the obstruction of the shutter structure, see Fig. 4.1d. This SC4 allows to vary the radiative flux in an independent manner without affecting the rest of the radiation units. Table 4.1 shows the global dimensions of the proposed shutters, as well as the manufactured flat SC1.

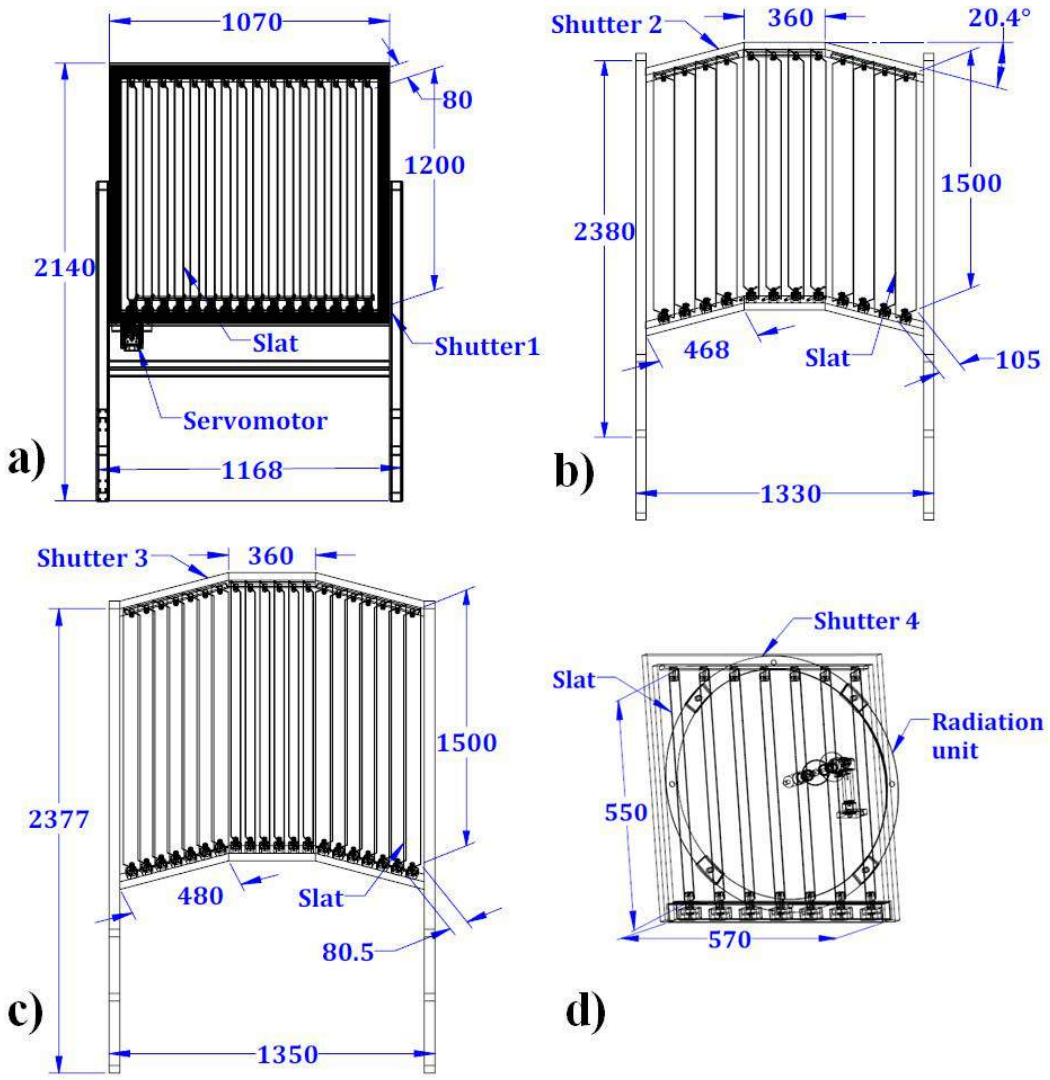

Fig. 4.1. Layouts of the 4 shutters designed to adjust the light flux delivered by the solar simulator (units in millimeters); a) SC1; b) SC2; c) SC3; d) SC4.

Table 4.1. Dimensions of the designed shutters.

Shutter	Structure (mm)		Slats (mm)		
	Height	Wide	Height	Wide	Thickness
1	2140	1168	1200	80	3
2	2380	1330	1500	105	3
3	2377	1350	1500	80.5	3
4	638	620	550	80	3

4.2.2 Flux modulation at different positions

The flux modulation analysis was also conducted by positioning the target at different planes behind the focal point of the solar simulator (away from the lamps array). Hence, the level of concentrated irradiance onto the target, as well as the flux distribution area can be theoretically modified. For carrying out this flux modulation, the target was displaced at 6 different locations from the focus f_2 to 300 mm further back over the *z* axis, in steps of 50 mm. As the target was displaced away from the focal point, the radiation units were adjusted within the model in position in order to maintain distribution of the flux spot over the target. Fig. 4.2a shows the separation between the radiation unit #5 to the unit #1 (center) of 708.5 mm when the target is at the focal plane f_2. For the case of the unit #4 (left from the central), the distance is the same as the unit #5 due to symmetry. The central lamp-reflector unit (#1) was kept fixed for all the analyzed positions of the target. The other radiation units were moved away from their initial position (pointing the focal point f_2) to 816.5 mm separated from the central unit, when the target is moved 300 mm behind the focal point, see Fig. 4.2b. To do so, the distance between the radiation unit 1 and unit 5 is increased in steps of 18 mm each time the target is relocated in steps of 50 mm further back the focal plane and so on.

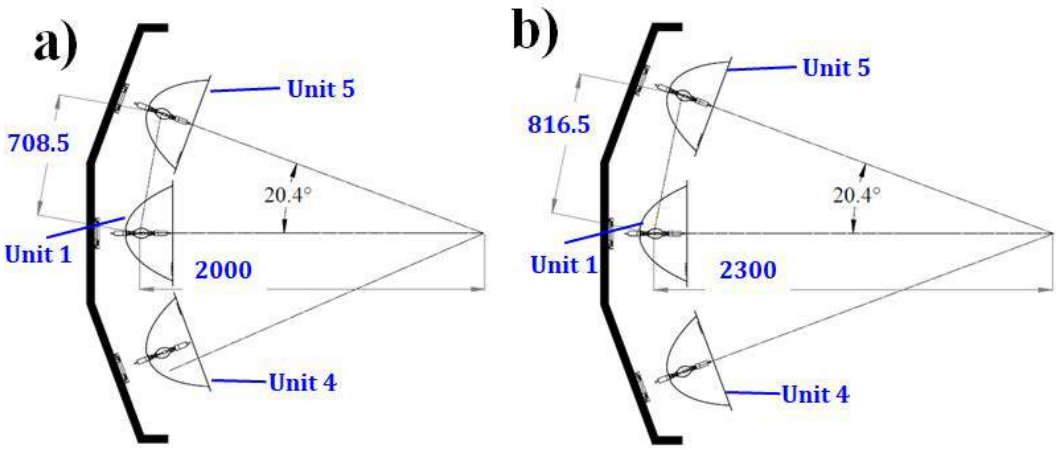

Fig. 4.2. a) starting position of radiation units #4 and #5 with respect to the unit #1 (central) when the target is located at a focal plane (2000 mm) in the model; b) separation between units when the target is displaced 300 mm further back the focal plane.

Table 4.2 depicts the distances between radiation units when the target is displaced from the focal plane. For the radiation units in the upper and lower rows (1, 2, 6 and 7), the same distances are applied due to symmetry with respect to the middle of the rows. It is worth mentioning that this

displacements of radiation units were performed only with the MCRT technique for analyzing the flux distributions and irradiance levels that could be achieved.

Table 4.2. Increments of the gap between the lamps when the target is relocated away from the focal plane.

Target displacement (mm)	0	50	100	150	200	250	300
Lamp separation (mm)	708.5	726.5	744.5	762.5	780.5	798.5	816.5

4.3 Flux modulation analysis by the MCRT method

In this study, the commercial software TracePro® (Lambda Research) was employed to assess the radiative flux output delivered by the solar simulator over the target at the focal plane and also at different planes further back. Since the SCs are complex 3D geometries for the optical analysis, TracePro becomes an excellent tool for obtaining detailed irradiance contour maps on the target for predicting the light regulation efficiency with the four designed shutters.

In order to determine the best performance that each curtain can provide, ray-tracing campaigns were carried out by using each of the designed SCs at different apertures of the slats. The complete aperture of the shutters is 0° in the angular movement of the slats, parallel to the normal of the SC (0° for fully open). The shutter aperture at 70° was identified as the maximum possible aperture that the concentrated flux can reach the receiver in this study. Therefore, radiative flux distributions were predicted on a target placed at the focal point by opening/closing the shutters from 0° to 70°.

For predicting the flux characteristics of the system, the main optical processes and properties that TracePro utilizes have been described in the previous Chapter, section 3.2. In order to conduct simulations in TracePro, the arc-emitter of the xenon lamps was modeled as a cylindrical volume source which emission is assumed diffusely and uniformly distributed with a cylinder radius of $r_{cyl} = 2.3$ mm and a length of $l_{cyl} = 5$ mm. Furthermore, the reflectance level on the concentrator surface was set to that of the standard mirror (94%). As aforementioned (Chapter 3), this reflectance level is chosen in order to determine the maximum optical performance than the system could achieve. Correspondingly, surface properties of the SC and the target were considered as perfect absorbers due to the fact that the objective is to analyze the geometrical curtain shape as an obstructing element for the light beams and estimate the total flux distribution on the target.

4.4 Experimental setup to characterize the flux adjustment

In order to acquire a detailed evaluation of the ray-tracing campaigns, radiative flux measurements with the radiation unit #1 were performed. The indirect flux mapping technique was employed through the use of a CCD camera and a diffusely reflective flat target, as described in the previous Chapter, section 3.3.1. With this technique, images of the brightness spot over the target were captured with the camera. Then, the gray-scale intensity of the pixels is related with the concentrated flux density measured with the Gardon sensor. Accordingly, the flux maps over the target are achieved [71].

Fig. 4.3 illustrates the experimental setup for measuring the irradiance distribution over the target, as well as recording pictures of the flux spot for obtaining the flux maps. The validation of optical model was performed by using the SC 1 (Fig. 4.1a). This shutter is utilized for practical purposes of flux evaluation because the central radiation unit is not significantly affected by the manner that the shutter obstructs the flux through the slats. In this form, if the flux measurements are in accordance with the predicted flux obtained by the MCRT method, then the shutter design with the best performance can be considered for fabrication. The SC 1 was positioned 1000 mm in front of the focal point. Furthermore, experiments were carried out by adjusting the shutter aperture from 0° (fully open) to 60° with steps of 5° in the angular movement of the slats. To measure the concentrated flux, a water-cooled Gardon type radiometer was employed, as shown in Fig. 4.3. As explained in the previous Chapter, this TG1000-0 sensor, manufactured, calibrated and certificated by the Vatell company, can measure heat flux densities of up to 1.08 MW/m^2 with a calibration constant of 108.2 kW/m^2/mV [109].

To reflect the concentrated irradiance, a 304.8 mm × 304.8 mm steel plate with thickness of 12.7 mm was employed as the target plate for applying the flux mapping technique. This steel plate was coated with a high-temperature tolerance white matte commercial coating (650 °C), Comex [112] for reflecting the concentrated light incident on it. Then, this plate is assumed as a diffusively reflecting flat plate and pictures of the concentrated irradiance distributed on its surface can be recorded. Furthermore, a three-axes testing bench with positioning error of ±1 mm was utilized to displace the target over the focal plane and different planes behind it (away from the lamps) for the flux modulation analysis.

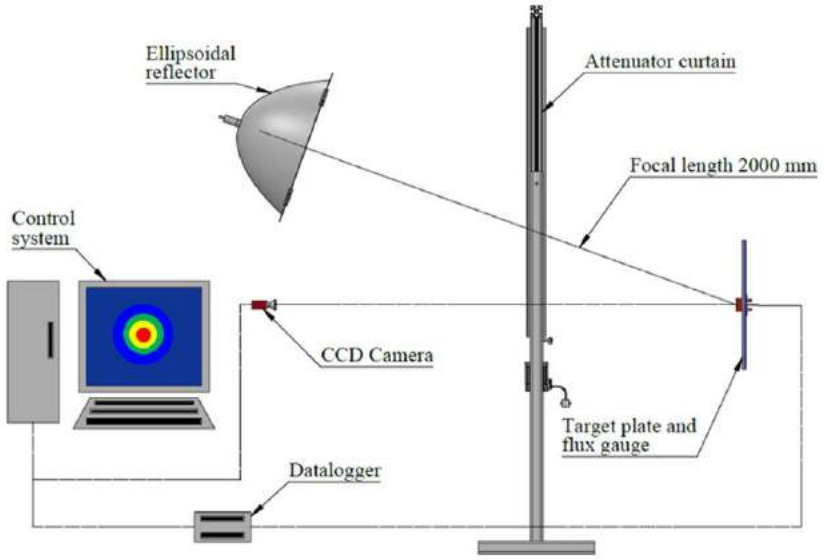

Fig. 4.3. Experimental configuration for applying the flux mapping technique and taking flux measurements with the flat SC1.

In order to take pictures of the brightness spot onto the target, the same CCD camera described in Chapter 3 (AVT-MK5054), with 1.24 Mpix, was utilized for this purpose. Furthermore, the same Varifocal Lens and density filter were also employed to diminish the bright of the flux spot and avoid saturation. The CCD settings were established in monochrome mode with an exposition time between 20-50 ms depending on the distance at which the target was relocated. Besides, for calculating the flux map, the camera was reconfigured, and the optics were adjusted at each plane where the target was positioned for avoiding distortions.

As the shutter is introduced in the setup, the CCD camera is installed at 1350 mm in front of the focal plane, at one side of the shutter, forming an angle of 50±1° with respect to the receiver's normal. Due to this, a transformation of the pixels to real coordinates in the plane are carried out by processing the images in MATLAB®. In order to relate the projected area to the target area, the approach explained in [43,74] was employed for this purpose. Additionally, when flux maps were calculated at different planes behind the focal point, the SC was removed from the experiments and the camera was installed on its original position as explained in Chapter 3, at 2120 mm in front of the target, so avoiding perspective corrections.

To implement the flux mapping technique, flux measurements were taken at the focal plane and at different planes away the focal point, in a range from 0 mm (f_2) to 300 mm further back. These

flux measurements were taken after 10 minutes in order for the lamp to attain the steady state. Furthermore, a total of 30 images per flux map were taken, averaged, and processed in MATLAB. Besides, the dark current was measured by capturing unexposed pictures and then was removed from the averaged gray-scale map. For calculating the flux maps, Eq. (3.9) and (3.10) were implemented. By obtaining the flux mapping result, the electrical-to-radiative conversion efficiency was calculated by means of Eq. (3.11).

4.5 Ray-tracing results and discussions

4.5.1 Ray-tracing analysis with the different shutter curtains

To carry out ray-tracing simulations, a ray number of $2x10^6$ per radiation unit was implemented for all simulations because this ray quantity offers good balance in simulation accuracy and computational cost, as discussed in section 3.4.1. From the simulation results, the total estimated peak flux reaches 1690 kW/m^2 and the total power of 5.8 kW over a target diameter of 120 mm when the 7 radiation units are employed without the SCs.

Fig. 4.4a shows the radiative peak flux modulation when the SCs are gradually closed from 0° (fully open) to 70° in steps of 10°. For the SC1, it can be appreciated that, compared with the peak flux estimated without the shutter, a lower peak flux of 900 kW/m^2 is obtained, presenting radiative losses due to obstruction of the structure of up to 47%. The radiative loss is the amount of delivered flux that is not intercepted by the target due to the obstruction of the shutter geometry. This level of radiative loss with the flat SC1 occurs due to the fact that the shutter slats fully open let the concentrated flux pass through them easier for the central radiation unit than the lateral units. This means, the position of the lateral radiation units with respect to the shutter's normal forms an angle which makes difficult for the light beams to pass through the slats. Accordingly, the shutter shape by which the concentrated flux is blocked is different for the outermost units as it is for the radiation unit at the center.

Unlike SC1, the other shutter designs can offer a more suitable geometry for letting the concentrated flux to pass through and to be regulated. For instance, shutters 2 and 3 count with three sections that allow the light go through the slats in the same amount of level as the central radiation unit, see Fig. 4.4b. The SC2 provides a peak flux level of up to 1520 kW/m^2 for an aperture of 0°, decreasing until 46 kW/m^2 for an aperture of 70°. Correspondingly, the SC3 offers

a peak flux of 1450 kW/m^2 for fully open of the slats and 6 kW/m^2 for an aperture of 60°. From this comparison, it can be seen that the shutter 2 offers both wider ranges and higher values of flux levels than the shutters 1 and 3. When the SC4 is implemented, a peak flux level of 1570 kW/m^2 can be achieved for an aperture of 0°, while a peak flux of 92 kW/m^2 can be reached for an aperture of 70°. From Fig. 4.4a, the flux modulation offered by shutters 2 and 4 shows a similar trend over the analyzed range, showing also slightly better results with the SC4. Consequently, the SC4 can provide the best performance in modulating the output flux level on the focal plane.

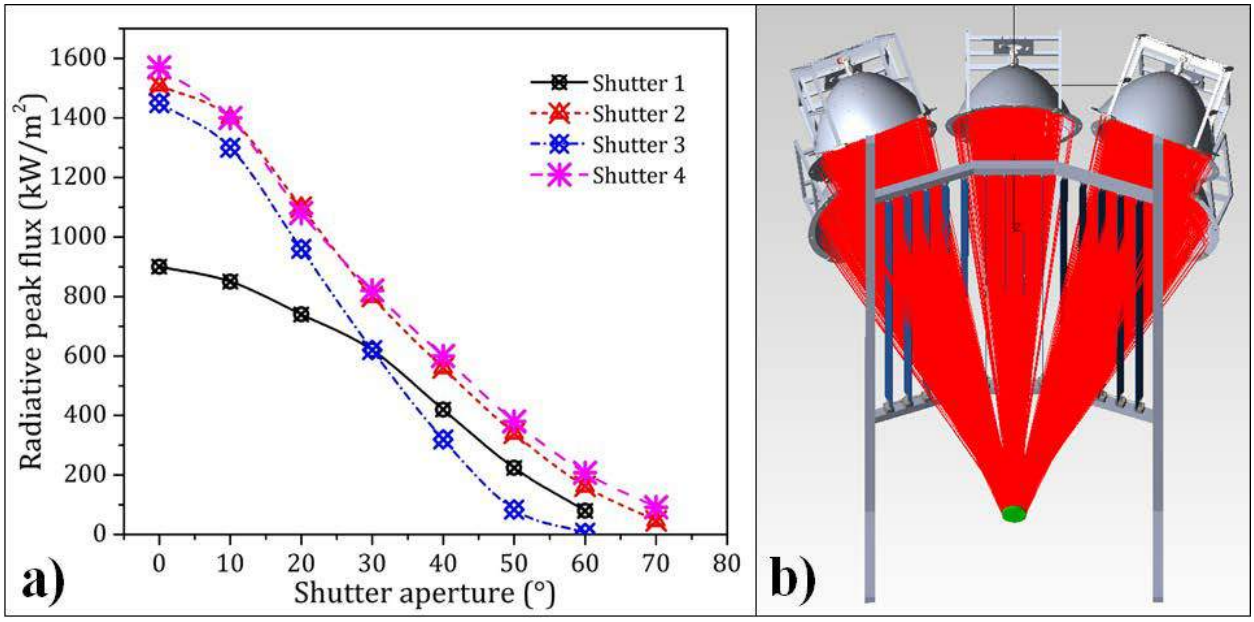

Fig. 4.4. a) Predicted radiative flux modulation as the shutter designs are gradually closed; b) model of the SC2 together with the HFSS.

Table 4.3 depicts the radiative losses estimated with the 4 analyzed cases which are derived from the structure obstruction. Cases 2 and 4 are the shutters that provide better results in both flux adjustment and low radiative losses, achieving a wider range of flux levels. The curtain with the highest efficiency is for the SC4 (individual shutter per unit). The SC4 lets pass a high level of concentrated flux, resulting in losses of only 7%. The SC2 (Fig. 4.4b) provides a quite similar performance than SC4, but involving quite less mechatronic complexity and exhibiting losses of 9%, only 2% more than the best case. Based on these results and looking for an excellent relation between the final cost and the benefit expected from the shutter, the SC number 2 is selected as the best design to regulate the radiative flux along with the designed lamp-reflector arrangement.

Compared with the manufactured flat shutter 1, the total flux modulation can be considerably improved by implementing the geometrical configuration of the shutter 2.

Table 4.3. Radiative losses of the shutters from the maximum flux available as a result of the light obstruction caused by the geometry implemented in each case.

	Shutter 1	Shutter 2	Shutter 3	Shutter 4
Radiative losses	47%	9%	14%	7%

4.5.2 Predicted flux distributions at different planes behind the focal plane

In order to analyze the flux modulation by modifying the target position at different planes behind the focal plane, MCRT simulations were performed without the use of the SCs. The target was displaced at 6 locations further back the focal point, from 0 to 300 mm behind in steps of 50 mm. As the target was relocated for radiative flux estimations in the model, the radiation units where relocated (see Table 4.2) to avoid hot-spots within the irradiance distribution onto the target. Fig. 4.5a depicts the reduction in radiative peak flux as the target is displaced further back the focal plane and Fig. 4.5b shows the predicted irradiance distribution 300 mm away from the focal point, achieving a peak flux up to 480 kW/m^2 over a target diameter of 210 mm. The predicted peak flux is regulated from 1690 to 480 kW/m^2 and the spot size is varied in diameter from 120 to 210 mm achieving an intercepted radiative power of 5.8 kW for all the analyzed cases. Therefore, by displacing the target away from the focus, a wide range of peak flux levels can be achieved, while keeping constant the intercepted power over the target for different spot diameters due to the energy conservation. Accordingly, different materials can be assessed depending on the flux requirements [56]. The decrease in peak flux between planes is not quite large owing to the fact that the tilt of the radiation units is maintained constant at 20.4° in the horizontal plane (*zx*) by readjusting the radiation units as the target is displaced, see Fig. 4.2. Otherwise, the more the divergence angle, the more the undesired flux peaks as the target is positioned away from the focus. It is worth mentioning that the adjustments in location of the radiation units do not guarantee that the flux spot can be maintained in a well-defined Gaussian distribution along the different planes at the same time. On the other hand, the relocation of the target at different planes provides the possibility to adjust the flux level and enlarge the flux spot area.

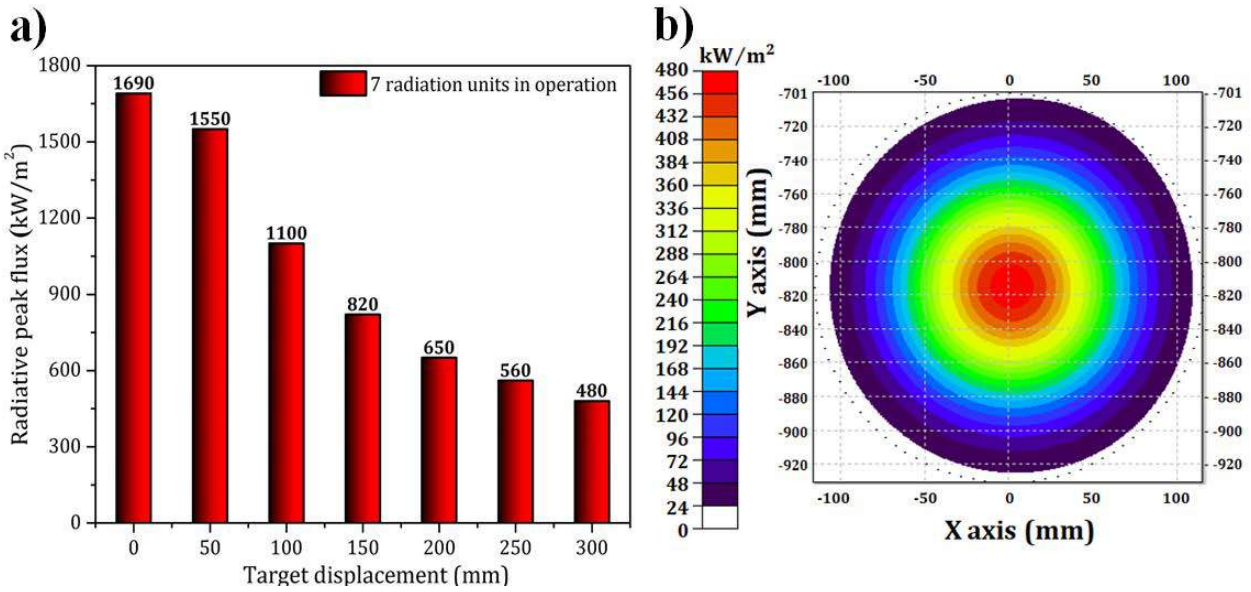

Fig. 4.5. a) Radiative flux modulation as the target is displaced away from the focal point; b) flux distribution with a predicted peak flux of 480 kW/m^2 at 300 mm away from the focal plane estimated with the 7 radiation units.

4.6 Experimental results and discussions

4.6.1 Flux modulation with a single radiation unit

To validate the MCRT model, the experimental results obtained with the central radiation unit #1 were utilized for comparison with simulations when the target is displaced further back the focal plane. Furthermore, flux measurements with a single radiation unit were compared with ray-tracing simulations when the manufactured flat shutter #1 is implemented for regulating the flux at the focal plane.

Based on the results obtained from the flux mapping technique with the central radiation unit 1, a peak flux of 210±9 kW/m^2 with an intercepted power of 740±33 W over a target diameter of 120 mm were measured (see section 3.5.2). The mean flux distributed over the target area is up to 65.4±2.8 kW/m^2 calculated from the flux mapping technique, and the electrical to radiative conversion efficiency of 32.8% was calculated with Eq. (3.11). The flux and power measured at the focal point is lower than the flux level predicted in the MCRT simulations. As explained in section 3.5.2.1, differences between simulations and experiments are mainly due to the higher reflectivity factor configured in the model (94%) in comparison with the reflectance measured on the manufactured concentrator (80%). Although the reflectance of the fabricated reflector is lower

compared with reported HFSSs (reflectance ≥90%), this level of specular reflectance is considered to be good enough, taking into account that a reflective coating layer was not applied. Hence, for carrying out an initial analysis, this concentrator is considered a suitable element to conduct concentrating flux testing.

In order to compare simulations and measurements properly, ray-tracing simulations were performed by configuring the specular reflectance equal to that measured over the surface of the fabricated concentrator. Therefore, a specular surface Almeco-Sacallm3, with 80% of specular reflectance, was configured in the settings of the software TracePro. Table 4.4 shows the comparison between the radiative peak flux predicted and measured at different planes, from 0 to 300 mm behind the focal plane. In addition, the respective flux spot diameter on the target at each analyzed plane is reported. These flux spot diameters represent the area at which the intercepted radiative power is kept constant (740 W) at all the different planes. Experimental results reveal a peak flux regulation from 210 ± 9 kW/m^2 to 95 ± 4 kW/m^2, compared with the flux estimated from 209 to 89 kW/m^2. It can be observed that both simulations and measurements exhibit a similar trend in peak flux reduction as the target is displaced further back the focal plane. Furthermore, the theoretical flux spot shows an increment in diameter between 10-15 mm among each target location along the analyzed range. Similarly, measurements show a flux spot increase of approximately 10-15 mm per target relocation, see Table 4.4. Differences in results can be related with the manual adjustment of the lamp in the focus f_1 inside the ellipsoidal reflector and can also be generated by manufacturing and mechanical installation errors of the optical system.

Despite all possible error sources, simulation results with the MCRT method are considered in good agreement with experimental results, and the relative error between simulations and flux measurements is within the repeatability of the implemented technique except for the last measurement at 300 mm behind the focal plane with 6.7% relative error.

Table 4.4. Comparison between radiative flux estimated and measured at the same reflectivity of 80%.

	Simulations		Experiments		Relative error between peak flux (%)
	Flux diameter (mm)	Flux (kW/m^2)	Flux diameter (mm)	Flux (kW/m^2)	
Focal plane	120	209	120 ± 3	210 ± 9	0.4
50 mm	130	194	130 ± 3	198 ± 9	2
100 mm	145	183	140 ± 3	175 ± 8	4.3
150 mm	155	165	148 ± 4	162 ± 7	1.8
200 mm	170	140	163 ± 4	143 ± 6	2.1
250 mm	180	115	176 ± 4	120 ± 5	4.3
300 mm	195	89	190 ± 4	95 ± 4	6.7

Fig. 4.6 depicts the modulation of the concentrated irradiance distribution delivered by a single radiation unit (central) measured in distances range from 0 (focus) to 300 mm away from the lamp array, in steps of 50 mm between measurements. These outcomes exhibited that the peak flux level can be adjusted from 210-95 $kW/m^2$and the flux spot area can be enlarged from 120-190 mm in diameter. Moreover, it can be observed that the Gaussian-like flux distribution can be kept in a wide range of distances and that local "hot-spots" are not generated. This is important in experiments where the irradiance distribution over the walls needs to be as uniform as possible, such as assessments with volumetric and cavity receivers [50]. In this context, an HFSS with adjustable flux spot can offer the versatility to carry out different researches in solar thermal and thermochemical applications where large flux spot areas and low peak flux levels are required [122].

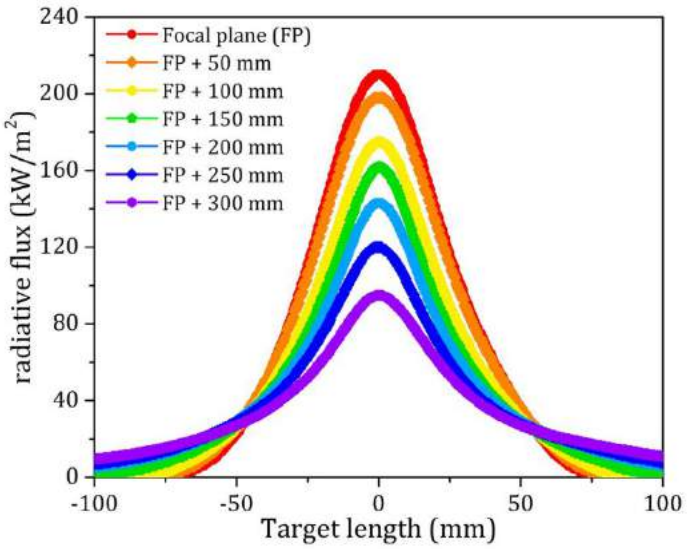

Fig. 4.6. Radiative flux modulation of the central radiation unit measured from the focal plane (FP) to 300 mm away from the lamp array.

4.6.2 Validation of the flux regulation with the shutter #1

The flat SC1 is utilized together with the central radiation unit for conducting flux modulation experiments. This SC was fabricated together with the HFSS, but its performance was not analyzed in detail because of the system complexity. Nevertheless, this element is critical and useful to determine the viability that a shutter curtain can provide for adjusting the flux level. Therefore, this flat shutter is employed for the initial analysis and for comparing measurements versus theoretical results as part of the validation. This flat SC was positioned 1000 mm in front of the

focal point and measurements were taken for an aperture range from 0° (fully open) to 60° in steps of 5° in the angular movement of the slats for each flux measurement campaign. Furthermore, in order to compare the experimental results with the predicted results from the ray-tracing analysis, a reflectivity factor of 80% was configured on the concentrator surface for simulations with TracePro. Besides, a range of apertures of the shutter from 0-60° with steps of 2° of resolution was established for the ray-tracing analysis.

Fig. 4.7 depicts the outcomes of both simulations and measurements when the flat shutter 1 is implemented to modulate the radiative flux on the target located at the focal plane. The outcomes show a monotonically reducing trend of the flux level as the shutter is gradually closed. Experimental results present a flux modulation in the range from $174.7 \pm 7.5\ \mathrm{kW/m^2}$ to $0.55 \pm 0.02\ \mathrm{kW/m^2}$ for slat apertures from 0° to 60°, respectively. Correspondingly, the predicted flux modulation obtained from the MCRT method is in the range from $178\ \mathrm{kW/m^2}$ to $0.6\ \mathrm{kW/m^2}$ for slat apertures from 0° to 54°, respectively. From this result, the relative error between simulations and measurements is about 4.8% within the analyzed range. Accordingly, the flux modulation analysis in the experimental campaign is in good agreement to simulation results.

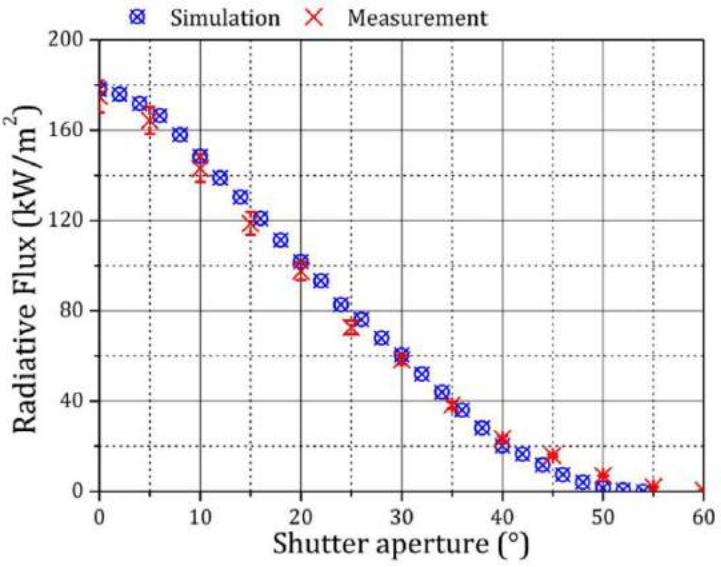

Fig. 4.7. Comparison between flux modulation measurements (red cross) and predicted radiative flux (blue circles). Measurements were taken each 5° in aperture and simulations each 2°.

From the experimental evaluation, it can be inferred that the shutter is an excellent tool to adjust the flux level without the need to displace the target receiver from the focal plane. Hence, the

mechatronic shutter becomes a competitive advantage of the system, because it provides versatility to conduct experimentation for complex photo-thermal processes where more precise heat flux levels are required [118].

In order to apply the flux mapping technique, the methodology described in section 4.4 is used together with the flux measurements taken at the focal plane described in Fig. 4.7. For this analysis, flux maps were calculated each 10° of the aperture of the manufactured shutter from 0° to 40°. Fig. 4.8 shows the flux maps over a target area of 200 mm x 200 mm. The radiative flux measurements, obtained for aperture adjustments of 0°, 10°, 20°, 30° and 40°, are up to 174.7 ± 7.7, 143.2 ± 6.3, 97.5 ± 4.3, 58.3 ± 2.7 and 23.3 ± 1.1 kW/m^2, respectively. For the same range of apertures and flux measurements, the intercepted power is calculated in 620 ± 27 W, 450 ± 19 W, 310 ± 13 W, 135 ± 6 W and 40 ± 1 W over target diameters of 115, 108, 96, 85, and 60 mm, respectively. Hence, it is observed that the radiative power can be alternatively regulated by reducing the flux spot area when the shutter is gradually closed instead of increasing the spot by displacing the target further back the focal point.

From this experimental result, it can be appreciated that the geometrical configuration of the shutter for obstructing the path of concentrated flux does not alter the flux distribution over the target in an inconvenient manner. As the shutter blocks the light beams, the distribution keeps its Gaussian-like shape without undesired hot-spots that could generate thermal loads or critical damage to solar-thermal materials under analysis [123]. Accordingly, with the experimental validation, critical information from the flat shutter #1 was obtained and reliable design parameters to manufacture a more efficient shutter for improving the system's optical performance can be effectively achieved. Therefore, the experimental results provide validation to the whole model implemented in the MCRT method with TracePro. As a result, the development of the SC2 could provide higher efficiency with lower radiative losses compared to the flat shutter #1.

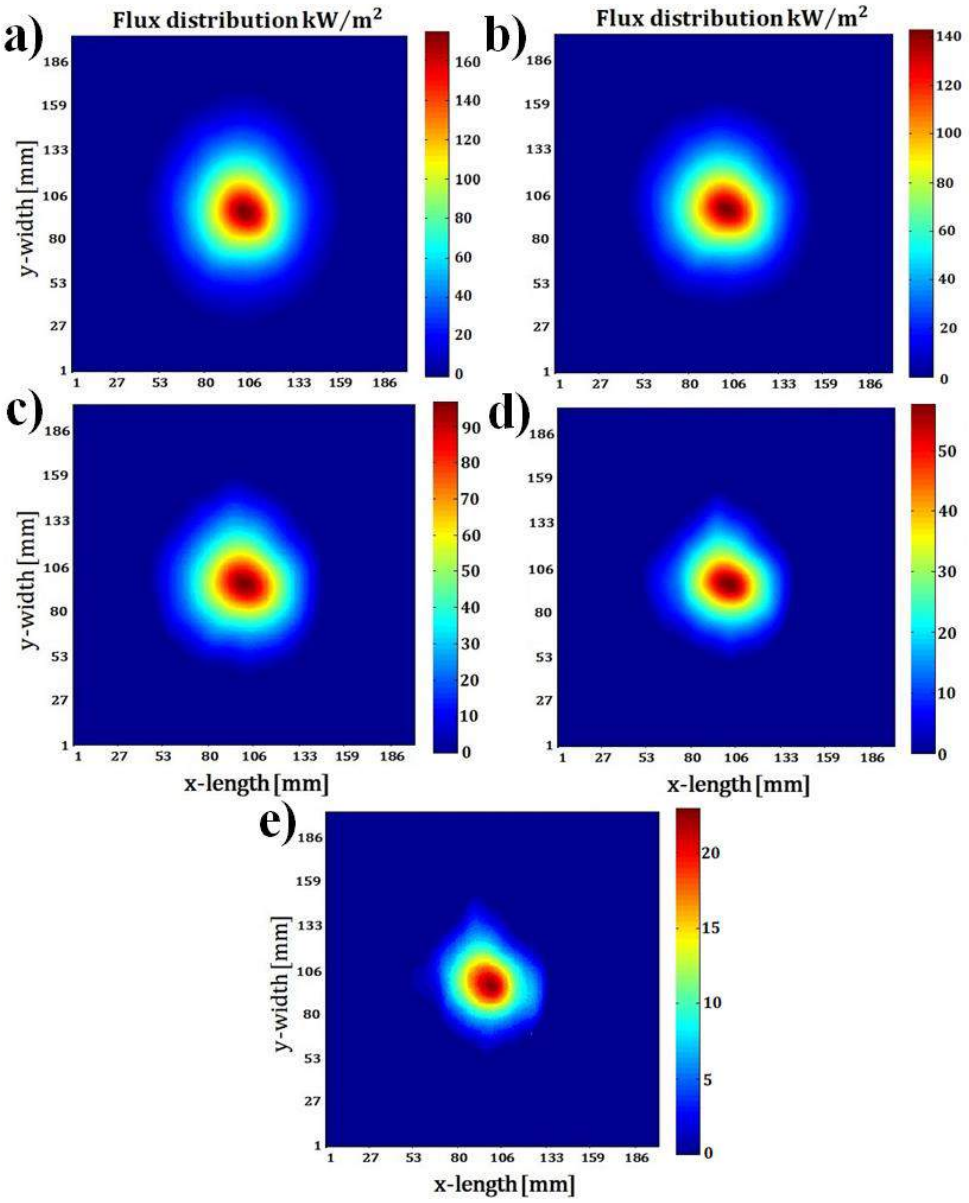

Fig. 4.8. Flux maps obtained at the focal plane when the manufactured shutter 1 is employed, using curtain apertures of: a) 0°; b) 10°, c) 20°, d) 30° and e) 40°, respectively.

4.6.3 Construction of a new shutter curtain

Based on the results obtained with the SC1, the ray-tracing analysis was validated, so the development of a shutter for improving the flux modulation was conducted. From the ray-tracing analysis, the shutter design #2 was found to have the best performance with low radiative losses of 9%. However, in order to recycle the manufactured material used in the flat shutter 1, a new SC, named #5 was designed, containing the main design parameters of both the fabricated shutter 1 and the shutter 2 (selected layout Fig. 4.1b). Fig. 4.9a shows the physical layout of the flat shutter

1 and Fig. 4.9b shows the layout of the new shutter design, presenting design parameters quite similar to those implemented in the shutter 2 such as two tilted lateral sections (20.4°) and one flat central section. Then, the normal vectors of these lateral sections can be pointing to the outer columns of the radiation units. This new curtain counts with 14 slats, 5 slats per lateral section and 4 slats in the middle section. The manufactured slats from the flat shutter 1 were implemented in this new design and the structure made of 50.8 mm × 50.8 mm RHS (Rectangular Hollow Sections) steel with epoxy paint finish was also used.

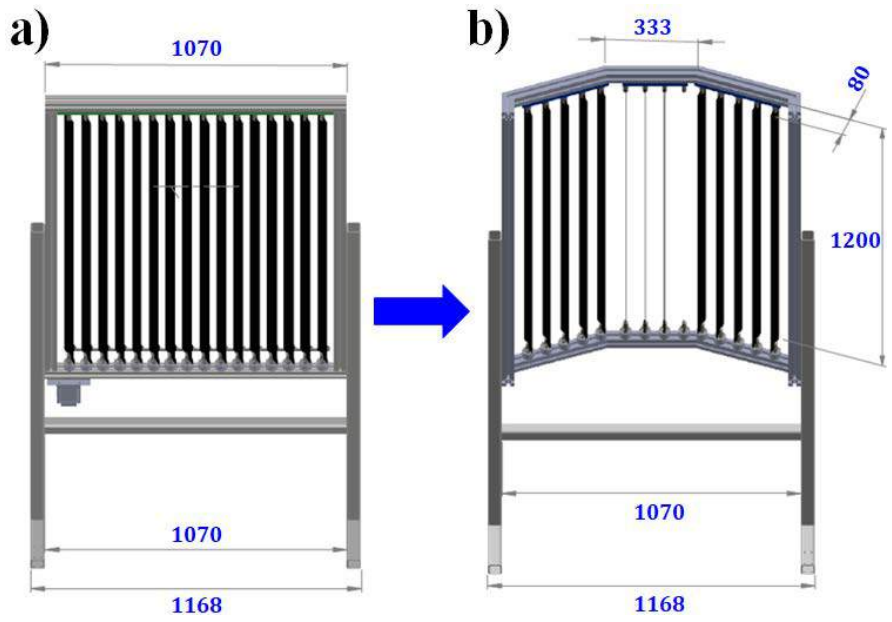

Fig. 4.9. a) Flat shutter design #1 which was manufactured; b) new shutter design #5 based on the characteristics and materials used in the flat shutter 1.

The new shutter design was analyzed through the MCRT method with the same methodology implemented in section 4.5.1. Fig. 4.10 presents the comparison between the predicted flux modulation offered by the shutter 1, shutter 2 as well as the new shutter design 5. It can be observed that the reduction in the peak flux has a similar trend between shutter 2 and the shutter 5 both having a range of shutter apertures of 0-70°. The SC5 shows a peak flux modulation from 1440 to 25 kW/m^2, presenting radiative losses of 15%, 6% higher than shutter 2. This is an important result since the fabricated SC revealed an efficiency up to 53%, and by modifying the geometrical configuration, the efficiency is improved by 32% higher. This efficiency is the ratio of the intercepted flux with the shutter to the intercepted flux without it. The experimental results obtained with the flat shutter 1 showed good agreement with simulations within the 4.8%, as

described in the previous section. Therefore, the possibility to achieve a higher flux modulation efficiency, such as that obtained with the shutter 5, can be effectively accomplished.

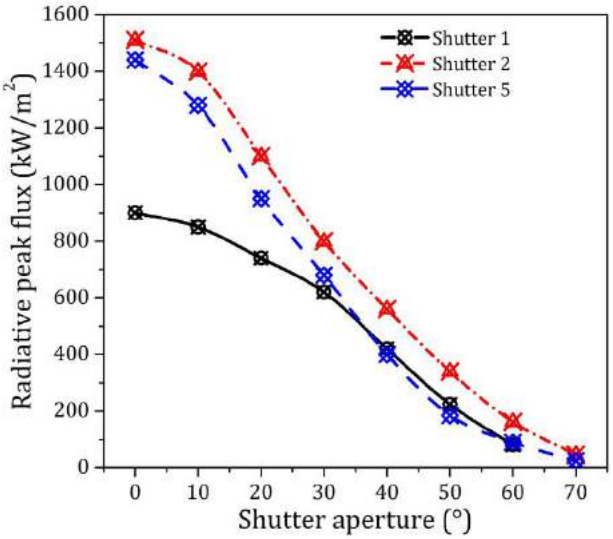

Fig. 4.10. Comparison of the theoretical flux modulation achieved with the flat shutter 1, the best shutter chosen from the ray-tracing analysis (shutter 2) and the new shutter design 5.

Fig. 4.11a shows a photograph of the SC5 developed from recycled materials previously used in the shutter 1 and Fig. 4.11b shows the front view photograph of the shutter with the servomotor installed in the central section of the curtain for opening/closing the slats. This shutter is controlled by a CR1000 data logger (Campbell Scientific), ±0.06% analog voltage accuracy, and an encoder is also used for regulating the angular position and speed movement of the slats.

At this point of the project, the new SC has not been validated for regulating the flux output due to installation details. For future work, the proper flux modulation analysis is expected to be conducted with the new shutter which is predicted to offer a more efficient flux adjustment than the flat shutter 1. Accordingly, the flux spot control capability in a mechatronic form can be highly improved for conducting solar-thermal research in low, medium and high temperature applications with this optical system.

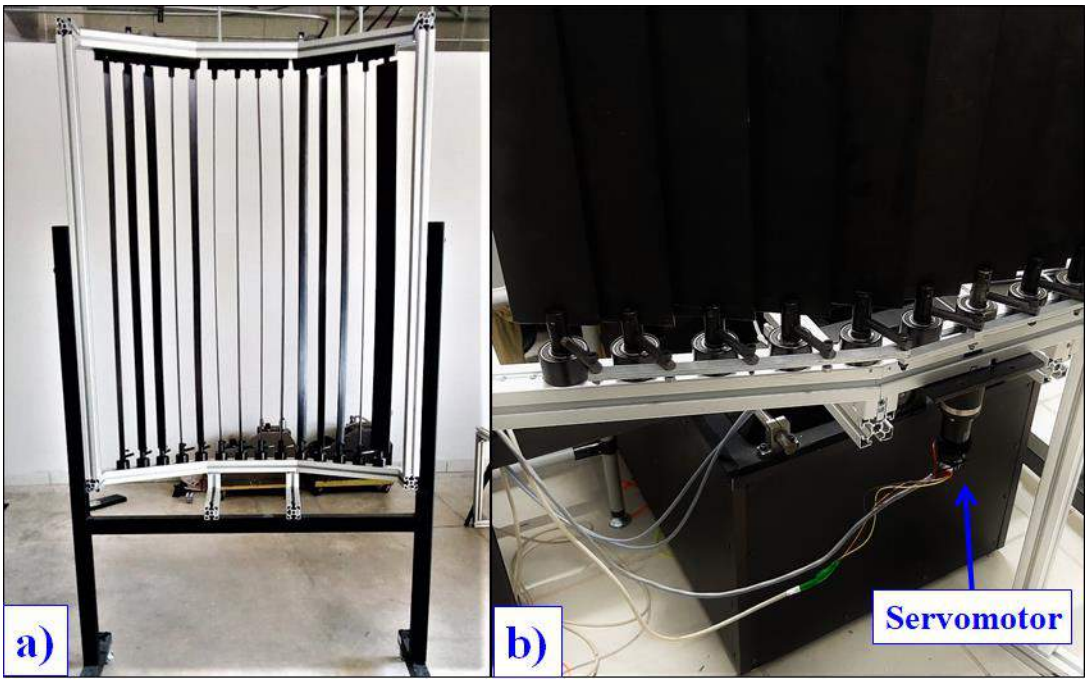

Fig. 4.11. New shutter curtain constructed from recycled materials from shutter 1: a) back view photograph; b) front view photograph with the servomotor installed in the middle of the structure.

4.7 Summary

In this Chapter, the optical optimization for improving the flux modulation capabilities of the developed HFSS has been numerically analyzed and experimentally validated. By using the software TracePro, the ray-tracing analysis was carried out by implementing three different shutter designs, as well as the manufactured flat SC. Simulation results showed that shutters #2 and #4 provided the best performances in both radiative flux modulation and low radiative losses. Based on the less mechatronic complexity and low radiative losses (9%) the SC2 was chosen as the best option for modulating the flux output of the HFSS. Furthermore, the flux modulation analysis was performed by displacing the target at different planes away from the lamp array without using the shutter. The outcomes showed a predicted peak flux modulation from 1690 to 480 kW/m^2 with a spot size modified from 120 to 210 mm in diameter achieving an intercepted radiative power of 5.8 kW for all the analyzed cases. Hence, demonstrating that the displacement of the target at different planes can provide the possibility to reduce the peak flux level, while increasing the flux spot area. Accordingly, different materials can be assessed depending on the flux requirements.

The validation of the MCRT model was carried out by employing the central radiation unit 1 for comparison with simulations when the target is displaced further back the focal plane. Results exhibited a measured peak flux varying from 210 to 95 kW/m^2, compared with the predicted flux varying from 209 to 89 kW/m^2 for the same range of target displacements. These results revealed a similar trend in peak flux reduction compared with simulations, so demonstrating good agreement between the model and measurements. Furthermore, by utilizing the flat SC, flux measurements with the central radiation unit were conducted and compared with ray-tracing simulations for the flux modulation analysis. Results depicted a monotonically reducing trend of the peak flux level as the shutter was gradually closed, presenting a flux modulation range of 174.7-0.55 kW/m^2 for measurements, and a modulation range of 178-0.6 kW/m^2 for simulations, presenting a relative error of 4.8% over the analyzed aperture ranges.

In addition, the flux map system was implemented in order to analyzed the flux distribution when the manufactured shutter is open/closed at different aperture angles of the curtain slats. From the flux maps analysis, it was observed that the geometrical configuration of the shutter did not alter the irradiance distribution onto the target in an undesired form. Consequently, the experimental validation of the MCRT model has provided critical information for improving the system's optical performance by selecting suitable design parameters to fabricate a more efficient shutter. Furthermore, a new shutter was developed based on recycled materials from the shutter 1 and design parameters from the shutter 2. For future work, the validation of the new curtain will be conducted with the whole radiation units. Based on simulation results, it is expected to achieve a more efficient flux modulation than that obtained with the shutter #1. Therefore, a wider range of controlled flux levels with a more accurate flux resolution can be obtained for carrying out different solar-thermal experiments with this facility.

Chapter 5. Development of the calorimetric test bench for solar absorber coatings assessment

The efficiency of CSP technologies depends greatly on the capability of the solar receiver to convert radiative flux into thermal power which is taken away by a heat transfer fluid (HTF). Typically, solar absorber coatings (SACs) are applied on solar receivers in order to improve the flux absorption and, as a consequence, the efficiency of the solar system. Normally, SACs based on black paints provide a low-cost commercial solution for specific requirements and for different solar-thermal applications, such as non-concentrating, line-focusing, as well as point-focusing systems [83,124-127]. Therefore, the research on the radiative-to-heat transfer efficiency, as well as the useful lifetime of SACs is of great importance for improving this technology. In order to carry out solar-thermal research with different selective and non-selective SACs, a well-controlled laboratory environment is required to accomplish this purpose.

In this Chapter, the development of a test bench, based on the calorimetric measuring principle is reported. The test bench is coupled with the HFSS developed within this project for its utilization as the radiative flux input for experimentation. An energy balance is calculated in order to evaluate experimentally the heat transfer performance of the test bench, implementing the standard coating Pyromark®2500 as the reference coating. Furthermore, calorimetric experiments are presented by using 4 different commercial SACs and a new Soot of Forest Biomass (SFB) based coating, all deposited over aluminum substrates. Hence, the heat transfer performances and thermal efficiencies of the analyzed coatings can be compared under the same operating conditions; so offering an alternative approach for the assessment of commercial and new SACs. Accordingly, the flux acceptance of suitable materials for their usage in SHIP can be effectively determined.

5.1 Materials and methods

5.1.1. Construction of the calorimetric test bench

Generally, a test bench is an instrument developed to carry out assessments under a controlled environment where new prototypes can be evaluated for specific applications [128]. In parallel, a calorimeter is a practical instrument for measuring the radiative heat flux that a solar-thermal system can collect, so determining the performances of the system under analysis [104]. Traditionally, these types of calorimeters are developed using metallic materials such as copper or

steel due to their excellent heat conduction properties and high melting points for withstanding elevated levels of concentrated solar irradiance [97,101,102].

Although, aluminum is a material widely used in CSP systems, its usage is generally limited to the frames and casings of the absorber receiver. On the other hand, investigations have been conducted on the possible applications of aluminum in solar power systems. For instance, Farzaneh et al. [129] reported an analysis of the advantages of using aluminum in solar systems such as: high resistance to corrosion in outdoor operating environments and the suitable optical properties of its anodic layer that make it a candidate material for utilizing it as a solar receiver. Furthermore, Wang et al. has reported thermal stress analyses by modeling tube receivers based on steel, copper and aluminum for PTC systems [130]. Results showed an effective stress of 67.5 MPa for steel and a maximum value of 5 MPa for copper and aluminum. Hence, for lower values of thermal conductivity such as that of steel, the effective thermal stress of the tube receiver is significantly higher. Therefore, the level of stress tolerance results quite similar for copper and aluminum, implying that aluminum can be a suitable receiver option for PTC systems. In this context, the thermal conductivity of aluminum (170 W/mK) is greater than steel (14-20 W/mK) [131]. Additionally, important advantages for using aluminum as the body of the calorimeter are: the lower cost compared to copper, the less complexity for manufacturing compared to steel, as well as its straightforward manipulation due to the light-weight. Besides, the temperature range used for evaluating the SACs in this study is between 60 °C to 500 °C, which is under the limits of the melting point of aluminum (≤660 °C). Accordingly, aluminum has been selected for constructing the calorimeter's body in this study.

Fig. 5.1a shows the mechanical design of the calorimeter which is based on AA-6061-T651 aluminum. In order to simplify the heat transfer analysis, a flat-plate geometry was chosen for designing the calorimeter, and its dimensions were selected based on the flux distribution delivered by the solar simulator presented in Chapter 3. Dimensions of the plate are a length, height and thickness of 150 mm, 150 mm and 25.4 mm, respectively. For the inlet/outlet of the HTF, channels were drilled laterally with a diameter of 17.86 mm for cooling the system homogeneously. Furthermore, a receiving faceplate was manufactured for being coupled with the calorimeter plate, having an aperture diameter of 100 mm, as shown in Fig. 5.1b. In this design, the faceplate offers the possibility to slightly focus more light flux onto the absorber element. By combining the flat-

plate calorimeter with the faceplate, coated samples can be inserted and removed as interchangeable cartridges. Additionally, rockwool, thermal conductivity of 0.07 W/mK at 300 °C, was employed for insulating the whole test bench.

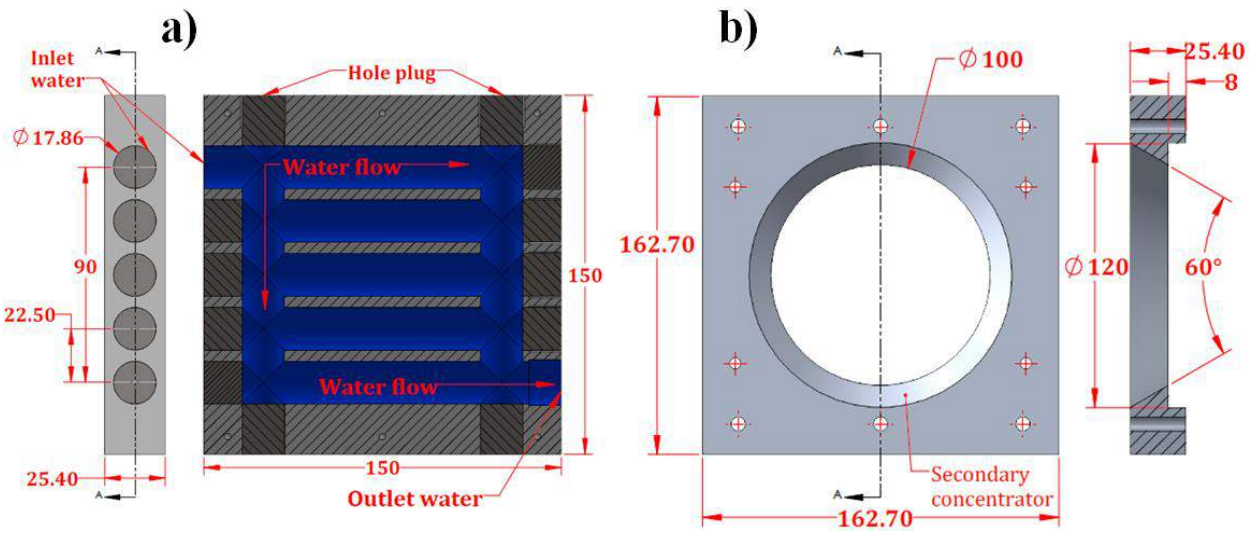

Fig. 5.1. Layouts of: a) the flat-plate calorimeter; b) faceplate designed with a conical aperture (units in millimeters).

Generally, for low temperature CSP systems, water or air are used as the HTF for taking the absorbed heat from the solar receiver. Correspondingly, at medium-to-high temperature applications, pressurized water, thermal oil, steam or compressed air are used for this purpose due to their thermo-physical properties to transport heat at high temperatures [20]. In order to simplify the mechanical design and to perform an initial analysis of the system, water was used as the HTF in this study. Fig. 5.2a depicts the layout of the test bench configuration together with the solar simulator. For this configuration, the sample under test is located in the focal plane of the HFSS. As explained in section 3.5.1, a data logger (CR1000), ±0.06% accuracy, ±3 min per year clock accuracy, was utilized for data storage of the measurement instruments such as temperatures and radiative flux. Besides, a water pump was employed for circulating the water inside the calorimeter, as shown in Fig 5.2b. A water mass flow rate of 24.63×10^{-3} kg/s was established by controlling the energy supply of the water pump and by opening/closing a valve. For measuring the mass flow rate, a flowmeter of ±3% output signal voltage accuracy was implemented, and the weighing technique was also implemented in order to verify the flow of water. By weighing the mass of water in a span of 1 minute, the added uncertainties are ±0.001 kg and ±1 s, respectively.

In order to measure the inlet and outlet water temperatures from the calorimeter, RTD PT100 sensors, with an accuracy of ±0.3 °C were implemented for this purpose. Besides, six Type-K thermocouples with ±0.75% error, were employed for measuring the raise in temperature on specific locations over the test bench and the test plates (samples). Additionally, a circulating chiller (Huber®) was connected along with an insulated thermotank (150 L) in order to maintain the working fluid in stable conditions while passing through the closed-loop circulation system.

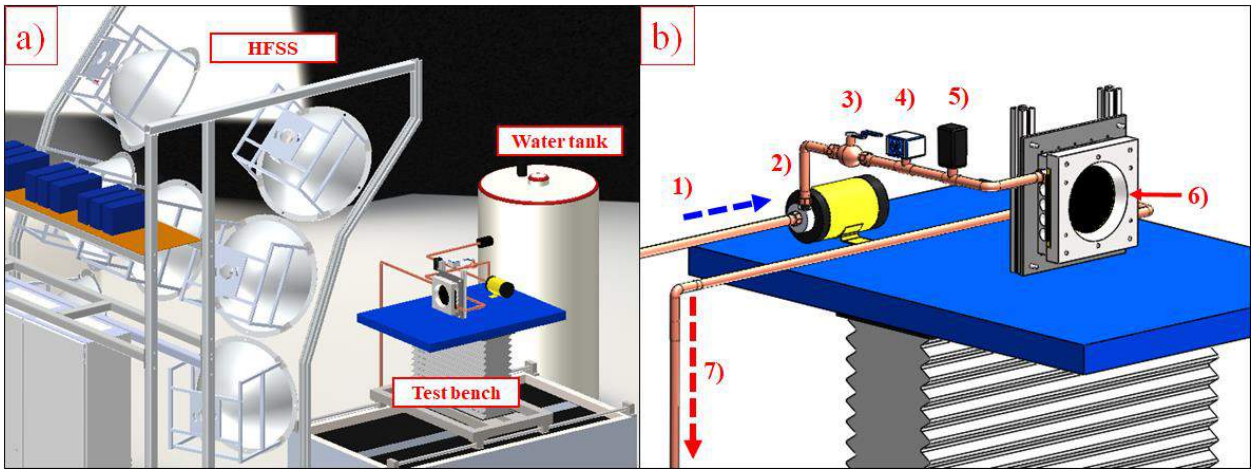

Fig. 5.2. a) Calorimetric test bench along with the solar simulator; b) components of the experimental configuration: 1) HTF inlet, 2) water pump, 3) ball valve, 4) flowmeter, 5) pressure transducer, 6) absorber receiver, 7) HTF outlet.

5.1.2 Description of the implemented SACs

In order to evaluate the performances of the proposed calorimetric test bench, a heat transfer analysis was carried out by using the standard coating Pyromark. Besides, the thermal efficiencies of different commercial SACs commonly implemented in solar-thermal systems, as well as a new absorber coating based on soot, were analyzed and compared.

Currently, the silicone-based coating Pyromark2500 is a non-selective black paint extensively employed for designing and testing CSP systems such as external receivers and cavity receivers for STP and PDC systems. This coating provides a temperature resistance of >1000 °C [14,124]. For low-medium temperature applications, the absorber coating Thurmalox250 offers a maximum operating temperature of ≤538 °C and is usually applied on metallic surfaces such as evacuated tube collectors, PTC systems, as well as flat-plate collectors (FPC) [86,126,127]. Similarly, the selective solar absorber coating (SSAC) silicone-based, Solkote is developed for CSP applications

such as PTC on metal receivers (aluminum, steel, copper), providing a temperature tolerance of up to ≤538 °C [125]. As well, this black coating offers resistance to both UV degradation and moisture. Furthermore, the high temperature resistant black paint Comex is a quick-drying silicone enamel spray coating with a maximum temperature tolerance of up to ≤650 °C [116]. Although its implementation in CSP applications has not been investigated extensively to date, its performance assessment is of interest in this study.

To provide sustainable alternatives to commercial coatings, a new non-selective SAC based on soot from forest biomass (SFB) is experimentally analyzed for determining its flux acceptance and efficiencies. This new soot-based absorber coating was provided from the collaboration with the Dr. Luis Bernardo López-Sosa, from the Universidad Intercultural indígena de Michoacán. The base of this coating, the forest biomass soot, is processed by means of mechanical grinding [88]. In order to fabricate the organic solvent, essential grapefruit rind oil is extracted by steam drag, which has been reported to act as a natural solvent for expanded polystyrene [132,133]. Accordingly, both the body and ligand of the absorber paint are based on a binder made of expanded polystyrene waste (Styrofoam), which was dissolved in grapefruit oil for producing the SFB coating mixture (soot + binder). The mixture proportion in mass between solvent and polystyrene is 3:1, according to [132]. The weight concentration between binder and soot was 60% and 40%, respectively [88]. Furthermore, the fabrication cost of this environmental friendly SAC is about 1 $USD/liter by implementing waste organic materials.

In order to obtain the required metal-coating tandem, AA-6061-T651 aluminum plates were chosen for this purpose. The dimensions of this metallic substrates are a length, height and thickness of 160 mm x 110 mm and 5 mm, respectively. With the use of an air spray gun, all the analyzed SACs were applied by spray deposition, which is a straightforward method for covering large surfaces. Fig. 5.3 shows the photographs of the 5 test plates (substrate-coating) applied at room temperature (25 °C) by the spray technique. In order to carry out the radiative-to-heat transfer efficiency comparison, the analyzed SACs were applied according to the procedures indicated by the manufactures. Such as, 1 layer of coating was applied on the aluminum substrate for Pyromark and Comex, as recommended in [124,116]. In parallel, 4 layers of the coating Solkote and 2 layers of the coating Thurmalox were deposited on their corresponding substrates in order to obtain suitable levels of absorptivity and emissivity by following the procedures recommended in [126]

and [127], respectively. For the case of the soot-based coating, the spray deposition was carried out through the procedure indicated in [88].

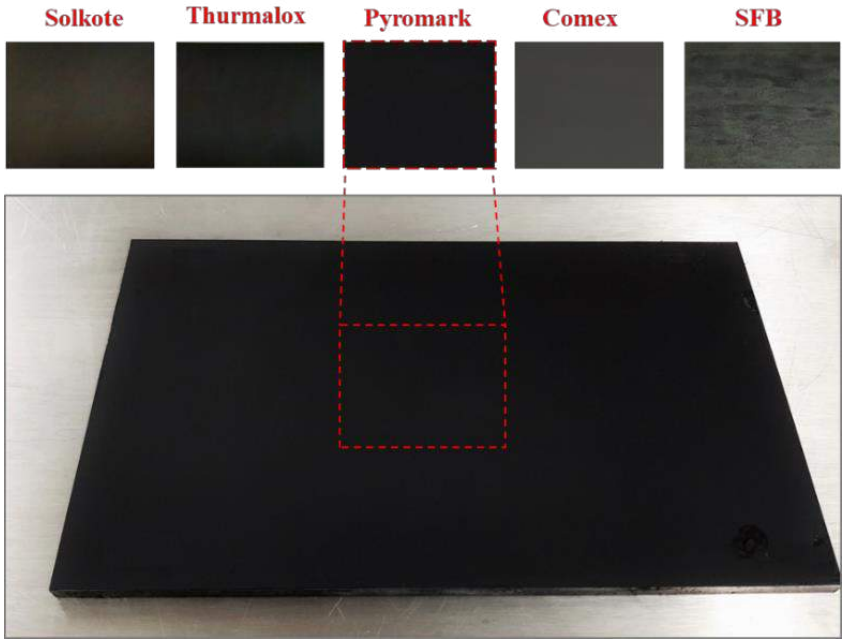

Fig. 5.3. Pictures of 5 SACs applied over aluminum substrates with the spray deposition.

The characterization of the absorber properties of SACs can be studied through the Kirchhoff's law of radiation, as mentioned in section 2.2.1. [59]. The statement of this law is that; the absorptivity and emissivity of a surface at a given temperature will be the same at thermodynamic equilibrium. For an arbitrary surface, the solar absorptivity (α) can be obtained by involving the spectral directional reflectance $\rho(\lambda, \phi)$ for opaque materials as described in Eq. (5.1).

$$\alpha = 1 - \rho(\lambda, \phi) \tag{5.1}$$

where λ represents the spectral dependence in wavelength, and ϕ represents the directional dependence of the incident radiation at a given temperature *T*. By performing the integration calculation of the spectral directional reflectance along with the spectral solar terrestrial irradiance $S(\lambda)$ within the spectral range λ_1-λ_2, the solar absorptance can be estimated with Eq. (5.2) [82].

$$\alpha_{abs} = \frac{\int_{\lambda 1}^{\lambda 2} S(\lambda)[1 - \rho(\lambda, \phi)]d\lambda}{\int_{\lambda 1}^{\lambda 2} S(\lambda)d\lambda} \tag{5.2}$$

As aforementioned, for an arbitrary opaque surface, the emissivity (ε) can be considered the same as the absorptivity at a given temperature, $\varepsilon = 1 - \rho(\lambda, \phi, T)$. Therefore, the total thermal emittance $\varepsilon(T)$ can be calculated by using the spectral solar reflectance data together with a suitably scaled black body spectrum given by Eq. (5.3).

$$\varepsilon(T) = \frac{\int_0^\infty \{[1 - \rho(\lambda, T)]B(\lambda, T)\} d\lambda}{\sigma T^4} \tag{5.3}$$

From this equation, σ represents the Stefan-Boltzmann constant; $B(\lambda, T)$ represents the black body spectrum of a given surface, which is described by Eq. (5.4) with $C_1$and C_2 being the first and second constants of Planck, respectively [59].

$$B(\lambda, T) = \frac{C_1}{\lambda^5 [e^{\left(\frac{C_2}{\lambda T}\right)} - 1]} \tag{5.4}$$

In order to measure the spectral hemispherical reflectance of the absorber coatings, a double beam Cary 5000 UV-Vis-NIR spectrophotometer, with an integrating sphere for specular and diffuse reflectance, was employed for this purpose. Then, the absorptance was obtained according to the standard method described in [134] by using the solar terrestrial spectrum with an air mass of 1.5 ASTM G173-03 in a range from λ_1 = 0.3 μm to λ_2 = 2.5 μm. Fig. 5.4a shows the spectral directional absorptance obtained with the coatings under analysis applied over aluminum substrates. From Fig. 5.4a, it can be seen that the non-selective coatings, Pyromark and SFB exhibit a higher absorption behavior in the solar spectral region, with slightly higher values for the SFB coating between 1.7-2.5 μm. The great absorptivity level in the SFB coating is attributed to the graphitic structures based on carbon nanoparticles previously found in this material through X-ray diffraction [88]. By Raman spectroscopy, previous researches have detected the presence of the G, D and 2D bands in the SFB coating which are related to the sp^2-sp^3 bonds, a characteristic mixture in carbon nanostructures [88,135]. Accordingly, the higher absorptivity is attributed to the carbon components found in the forest biomass soot, which provide to this material important light flux absorption capabilities. In contrast, the lowest spectral absorptance was achieved for the Comex coating with a monotonically reduction from 0.7-2.5 μm.

Furthermore, measurements of the spectral hemispherical reflectance of the SFB and Comex coatings in a range from 2.5-17 μm were provided by the Dr. Luis Bernardo López-Sosa, from the Universidad Intercultural indígena de Michoacán, based on a collaboration related to this study. These measurements were obtained with a Perkin Elmer Frontier FTIR spectrophotometer. Fig.

5.4b depicts the spectral emissivity of Comex and SFB coatings, observing that the emissivity increases in both cases at wavelengths higher than 6 µm. By calculating the integral of the spectral reflectance weighted against the black body radiation function at 200 °C (Eq. 5.3), the total thermal emittance is obtained in 0.92 and 0.86 for the SFB and Comex coatings, respectively. Currently, the Optical Research Center (CIO) counts with a Cary 670 FTIR spectrophotometer, but the equipment was not available during the development of this study. Therefore, the thermal emittance from Pyromark was obtained from previous published works [83], and for the cases of Thurmalox and Solkote the emittance was obtained from the manufacturer for a surface temperature of ≤400 °C and ≤260 °C, respectively.

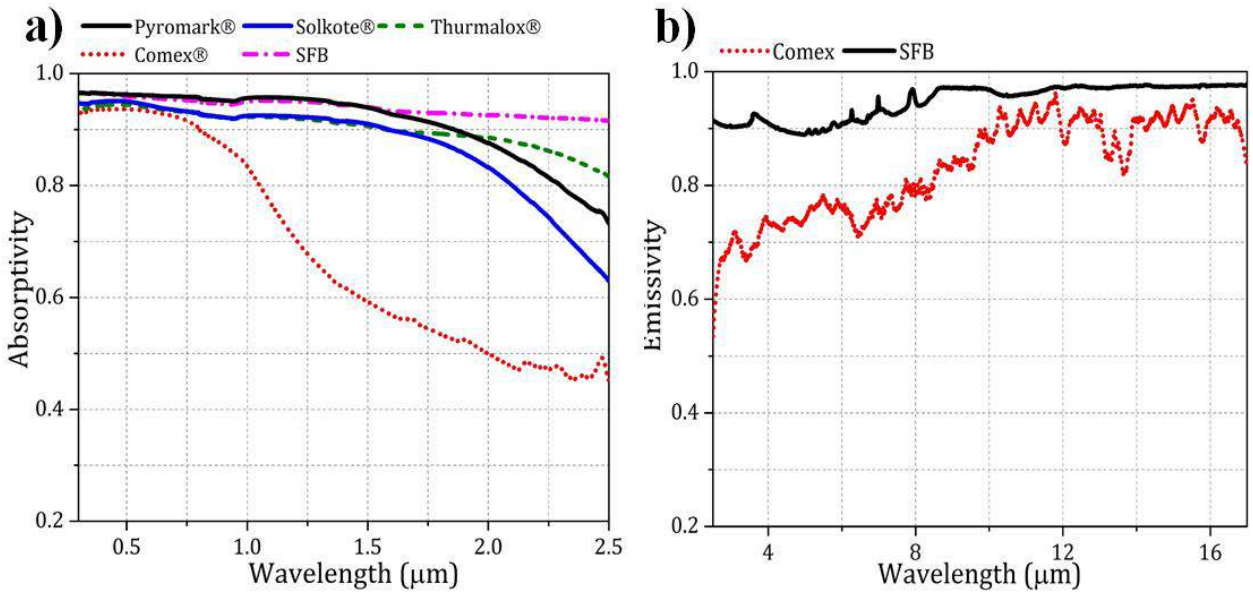

Fig. 5.4. a) Absorptivity values of the implemented SACs; b) emissivity of the coatings Comex and SFB.

Table 5.1 shows the optical properties of the solar absorber coatings under study. It can be observed that Solkote is the only selective coating with an emissivity of 0.27 at a temperature surface of 400 °C. Moreover, the SFB coating has the lowest temperature tolerance with ≤300 °C based on the reported by López-Sosa et al. [88]. Based on this, the heat transfer analysis and comparison are carried out by setting two radiative input powers in order to achieve temperature levels of ≤300 °C and >400 °C. Therefore, the absorption efficiency comparison of the commercial coatings, as well as the maximum performances of the SFB coating can be analyzed in a complete manner.

Table 5.1. Optical properties of the absorber coatings under study.

SACs	Absorptance (±0.1%)	Thermal Emittance (±0.1%)	Temperature tolerance (°C)	References
Pyromark®2500	0.95	0.85 (400 °C)	1000	[83]
Solkote®	0.93	0.27 (400 °C)	538	[125]
Thurmalox®250	0.93	0.50 (260 °C)	538	[126,127]
Comex®	0.84	0.86 (400 °C)	650	[116]
SFB	0.95	0.92 (100 °C)	300	[88]

Generally, evacuated tube receivers such as steel pipes or glass to metal welds in vacuum atmospheres are not implemented for low-medium temperature PTC technologies [136]. In this context, previous researches have demonstrated that evacuated tubes in PTC systems exhibited the frequent issue of vacuum loss, affecting the final system's efficiency [137]. Therefore, the assessment of solar receivers under an open environment is a relevant aspect for improving the performances of such systems. Correspondingly, evacuated environments are usually omitted at the receiver block of LFC technologies, so simplifying the design of the system [20]. Currently, one of the principal challenges in the development of SACs for CSP technologies is their efficiency enhancement under harsh environments (oxidation) [14]. Therefore, the solar-thermal research of SACs under an open environment is highly relevant, so an evacuated atmosphere for the calorimetric test bench is not employed in this study.

It is important to mention that the analyzed absorber coatings are fabricated by manufacturers for their employment in different solar-thermal applications at different operating conditions such as: oxidation environments, temperature and concentrated flux level. Therefore, the presented thermal efficiency comparison is not aimed to qualify the analyzed coatings, but to assess their performances with the aid of the calorimetric test bench. In this form, optical-thermal performances of different coatings, used for different applications, can be contrasted under the same operating conditions, and variations in efficiencies depending on individual qualities can be analyzed. As a result, the absorption performance offered by new SACs, such as the SFB coating, can be compared with commercial coatings and evaluated.

5.3 Heat transfer quantification

5.3.1 High flux solar simulator

The developed HFSS, integrated by seven 2.5 kW_e xenon arc lamps, is utilized as the flux input for the calorimetric experiments. The xenon lamps based HFSS offers artificial concentrated irradiation with a black-body spectrum (6000 K) quite similar to the terrestrial sunlight (5777 K) with an air mass of 1.5 [30,49]. Besides, solar-thermal and thermochemical research have been carried out by implementing such high-discharge arc lamps (2.5 kW_e) [50,57]. Additionally, solar simulators with similar artificial sunlight have been used for the comparison of different solar receivers [138].

To characterize the flux distribution delivered by the HFSS, the water-cooled Gardon type radiometer TG1000-0 was employed for this purpose. As explained in section 3.3, the sensor scale factor of ±3% provided by Vatell is considered accurate enough for concentrated flux measurements in this study based on the experimental validations published in the literature [72,111]. A characterization campaign was conducted with this Gardon gauge by measuring the heat flux onto the focal plane in a circular area of 100 mm in diameter in steps of 5 mm taking into consideration the faceplate of the calorimeter, see Fig. 5.1b. In order to calculate the input power $Q_{in}(R)$ incident on the target surface with radius *R*, the Eq. (5.5) was utilized for this purpose [139].

$$Q_{in}(R) = 2\pi \int_0^R q_{(r)} r dr \tag{5.5}$$

Where $q_{(r)}$ is the mean radiative flux over the target area and Q_{in} is the input power used for performing the calorimetric experiments. For this analysis, the flux mapping technique is not considered for characterizing the intercepted power over the target. The main reason is due to the high uncertainties that can be generated by the secondary concentrator of the test bench, taking into consideration that this indirect technique is used with a diffusely reflective flat target plate along with the CCD camera.

In order to carry out the test bench performance evaluation and the thermal efficiency comparison, the radiative input power Q_{in} was established in 2 different levels: low flux level and high flux

level. Accordingly, the thermal efficiency comparison of the analyzed SACs at low-medium and medium-high temperature ranges can be conducted.

5.3.2 Quantification of the energy balance

Fig. 5.5 depicts the layout of the calorimeter together with the test plate for the heat transfer assessment. The calorimetric test bench was equipped with six thermocouples type K (TC-K), ±0.75% uncertainty, which are shown with red dots from 1 to 6 in Fig. 5.5. In order to measure the receiver surface temperature, 3 TC-K were installed on the back surface of the testing plate (substrate-coating) locating them evenly from the center (0 mm in diameter) to 50 mm away. Furthermore, a 382×288 pixel resolution thermographic camera (OPT-PI400) was implemented for measuring the temperature distribution on the front side of the testing plate. The IR camera was previously calibrated adjusting the emissivity of the material under test. Moreover, measurements were previously taken on different samples with the calibrated TC-K and served as a reference to adjust the configuration of the camera, giving an uncertainty of 1.5%. Additionally, 3 TC-K were located on the front part of the test plate (red dot #4), on the faceplate (red dot #5) and over the calorimeter marked with the red dot #6 as shown in Fig. 5.5.

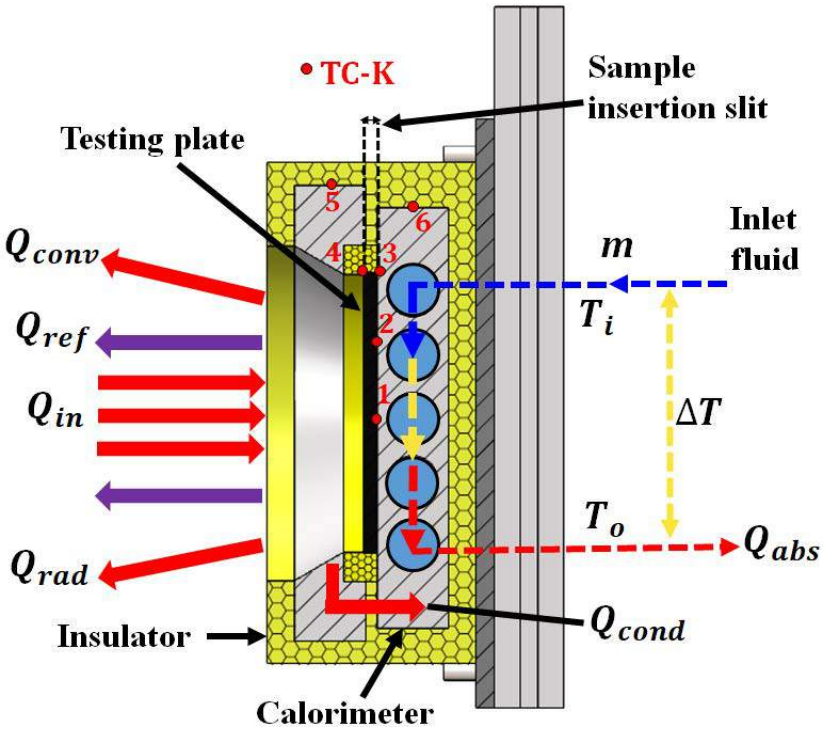

Fig. 5.5. Schematic layout of the calorimeter along with the testing plate for the analysis of the heat transfer process. Thermocouples (TC-K) are represented with red dots and numbers.

To quantify the thermal power transferred to the HTF (Q_{abs}), the proper energy balance of the working fluid was conducted by implementing the Eq. (5.6).

$$Q_{abs} = mC_{pw}(T_o - T_i) \tag{5.6}$$

where m is the mass flow rate of the HTF; C_{pw} is the specific heat capacity of water; T_i and T_o are the inlet and outlet water temperatures, respectively. The thermal efficiency η_{abs} can be defined as the ratio of the thermal power absorbed by the working fluid Q_{abs} to the radiative input power over the target Q_{in}, as described by the Eq. (5.7). This equation was utilized for quantifying the thermal efficiency η_{abs} of the different SACs under analysis.

$$\eta_{abs} = \frac{Q_{abs}}{Q_{in}} \tag{5.7}$$

Furthermore, thermal losses were assessed in order to evaluate the radiative-to-heat transfer performance of the test bench. The thermal losses can be assessed by an energy balance taking into consideration the input power Q_{in} on the absorber element of the test bench. As the thermal losses Q_{loss} involve the reflection (Q_{ref}), conduction (Q_{cond}), convection (Q_{conv}) and re-radiation (Q_{rad}) of the incident power, they can be simplified by $Q_{loss} = Q_{ref} + Q_{cond} + Q_{conv} + Q_{rad}$ [14]. Hence, the energy balance for thermal losses can be described along with the energy transferred to the working fluid Q_{abs} and the coating absorptivity α_{abs}, as shown in Eq. (5.8) [140].

$$Q_{loss} = \alpha_{abs} Q_{in} - Q_{abs} \tag{5.8}$$

The figure of merit of the coating efficiency is also employed to evaluate the SAC performance, which is based on the total energy absorbed by the coating to the total energy absorbed by an ideal selective coating ($\alpha_{ideal} = 1;\ \varepsilon_{ideal} = 0$) and is described by Eq. (5.9) [94, 141, 142].

$$\eta_{coating} = \frac{\alpha_{abs}\bar{q} - \varepsilon\sigma {T_s}^4}{\alpha_{ideal}\bar{q} - \varepsilon_{ideal}\sigma {T_s}^4} = \frac{\alpha_{abs}\bar{q} - \varepsilon\sigma {T_s}^4}{\bar{q}} \tag{5.9}$$

Based on this metric, the impact that each coating can have on the system can be analyzed by implementing optical-thermal parameters involved in the performance of each coating under test, such as; absorptivity α_{abs}, emissivity ε, coating temperature T_s and mean flux incident on the test plate $\bar{q}$. Furthermore, the maximum efficiency of the test bench can be calculated based on the efficiency of a Carnot heat engine operating between a high temperature and a low temperature level, which is described as follows [143]:

$$\eta_{max} = \eta_{carnot} = 1 - \frac{T_a}{T_s} \tag{5.10}$$

where η_{max} is the maximum efficiency of the test bench and T_a is the room temperature. Furthermore, an uncertainty analysis was conducted by taking into consideration the main error sources in the energy balance calculation [115]. Hence, the error propagation assessment was carried out, being the water mass (kg), time (s) and the temperature difference (°C) the principal contributions to the heat transfer uncertainty of the test bench.

5.4 Results and discussions

5.4.1 Performance evaluation of the test bench

In order to evaluate the heat transfer performance provided by the test bench, calorimetric experiments were carried out by applying the commercial coating Pyromark2500 on the absorber receiver. Fig. 5.6a depicts the picture of the AA-6061-T651 based test bench under installation. Furthermore, a proper radiative input power was established for conducting experiments at low-medium temperature levels with the aid of the shutter curtain. It is worth mentioning that the shutter was adjusted arbitrarily for obtaining the required flux levels without performing a deep analysis with the shutter, as described in section 4.6. Fig. 5.6b shows the concentrated flux spot incident on the analyzed test plate inserted into the test bench. It can be observed a rounded flux spot over the center of the receiver.

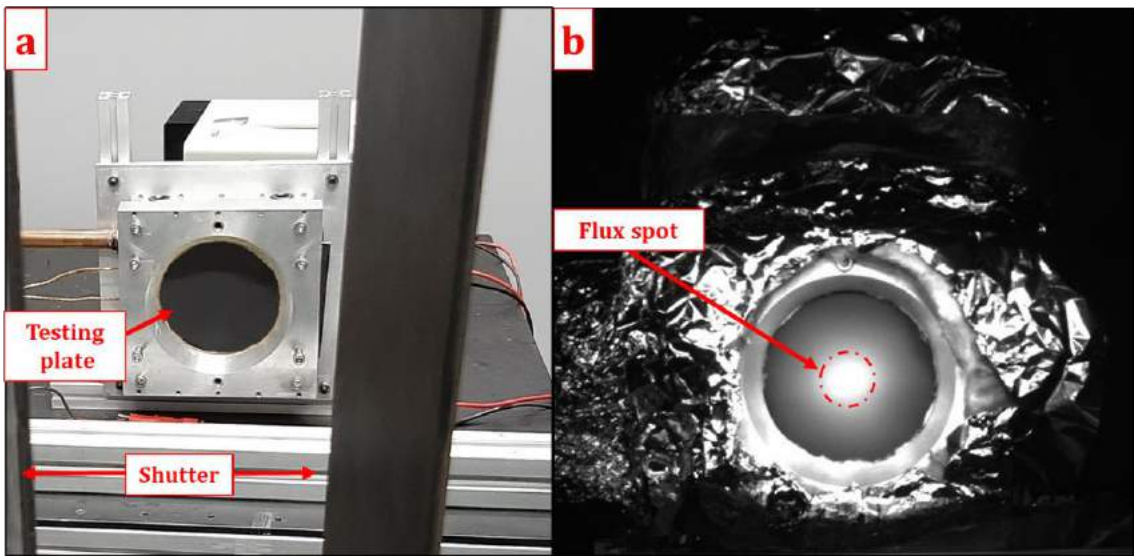

Fig. 5.6. a) Installation of the test bench for SACs assessments; b) concentrated flux spot on the analyzed test plate coated with Pyromark.

To carry out the thermal efficiency comparison with different commercial coatings, a peak temperature of approximately 500 °C was considered. Correspondingly, a low peak temperature for the assessment of the SFB coating was also used (≤300 °C). To do so, two different peak flux levels were adjusted. Fig. 5.7a shows the mean flux profile, called low concentrating flux level (LCFL) which corresponds to a radiative peak of up to 100±3 kW/m^2 with a mean radiative flux of 38.58±1.15 kW/m^2 and a radiative input power of 303±9 W within a target diameter of 100 mm. In order to obtain a higher concentrated irradiation for reaching higher temperatures, a second case called high concentrating flux level (HCFL) was adjusted for this purpose. Fig. 5.7b shows the mean radiative flux of the HCFL, having a radiative peak of up to 415±12 kW/m^2 with a mean flux of 157±5 kW/m^2 and an input power Q_{in} of 1238±37 W onto a target diameter of 100 mm.

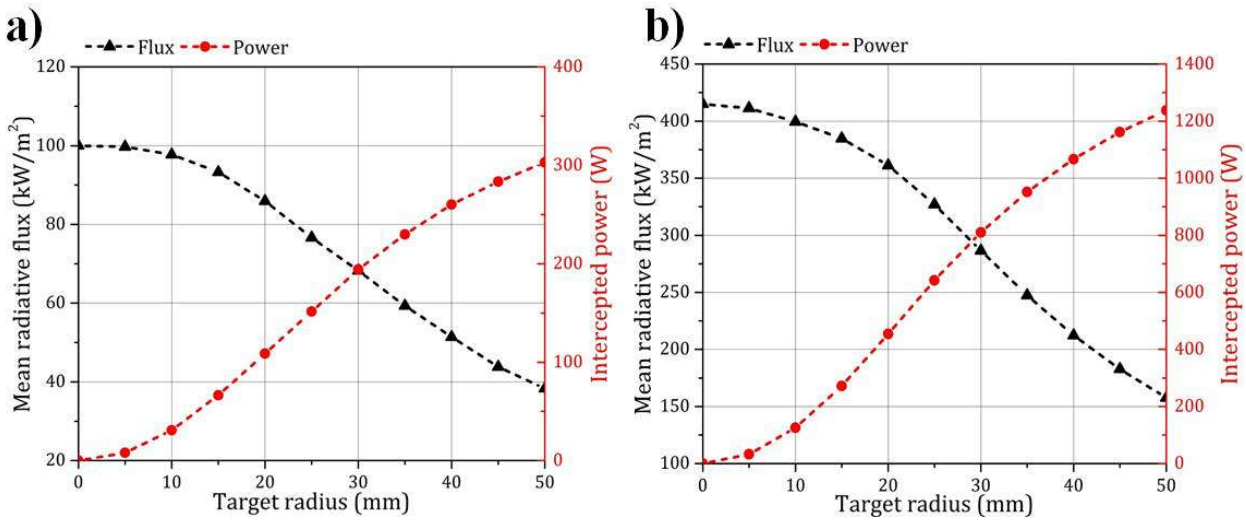

Fig. 5.7. a) Mean flux distribution and radiative input power at LCFL; b) mean flux distribution and radiative input power at HCFL.

This two flux levels were first used for analyzing the performances of the test bench when the Pyromark coating is implemented. Therefore, a sensitivity heat transfer analysis was carried out by using 4 different mass flow rates with each of the radiative flux levels. Fig. 5.8 shows the thermal efficiencies and temperature differences ($T_o - T_i$) as a function of the mass flow rate. Fig. 5.8a shows that, for a mass flow greater than 24.63x10^{-3} kg/s, the thermal efficiency begins to saturate between 91-92.5%, while at flow levels less than 24.63x10^{-3} kg/s the efficiencies drop between 85.6-90%. In contrast, as the mass flow rate increases, the temperature difference (ΔT) decreases. This is due to the fact that at low flow rates, the working fluid is limited in removing

heat from the test plate, which implies not only an increase in the system's temperature, but also in thermal losses; for a mass flow rate of $15x10^{-3}$ kg/s the temperature of the calorimeter (TC#6, see Fig. 5.5) was 34 °C, while at $28x10^{-3}$ kg/s TC#6 was 23 °C, almost room temperature (20 °C). Similarly, Fig. 5.8b shows the behavior of ΔT and thermal efficiency as a function of mass flow rate. Hence, it is observed that for flow rates greater than $24x10^{-3}$ kg/s the efficiencies begin to saturate between 88-90% for temperature differences between 9-11 °C, respectively. For this case of HCFL, the temperature of the calorimeter was up to 58 °C at a mass flow rate of $28x10^{-3}$ kg/s and 78 °C for a flow rate of $15x10^{-3}$ kg/s. The implemented mass flow rates were $15x10^{-3}$±0.24 $x10^{-3}$ kg/s, $20x10^{-3}$±0.32 $x10^{-3}$ kg/s, $24.63x10^{-3}$±0.39 $x10^{-3}$ kg/s and $28.7x10^{-3}$±0.45 $x10^{-3}$ kg/s obtaining thermal efficiencies of 85.66±3.1%, 89.51±3.3, 91.74±3.8% and 92.5±4.2%, respectively for a LCFL, and 75.96±2.73%, 84.41±3.14%, 88.69±3.41% and 90±3.5%, respectively for a HCFL. Although a high temperature difference is useful in reducing the uncertainty level (in particular for LCFL), higher mass flow rates provide higher efficiencies, as well as contribute to keep the receiver well cooled avoiding damage to the coating and possible delamination. Therefore, a mass flow rate of $24.63x10^{-3}$ kg/s is considered a reliable value to carry out the experiments with the test bench.

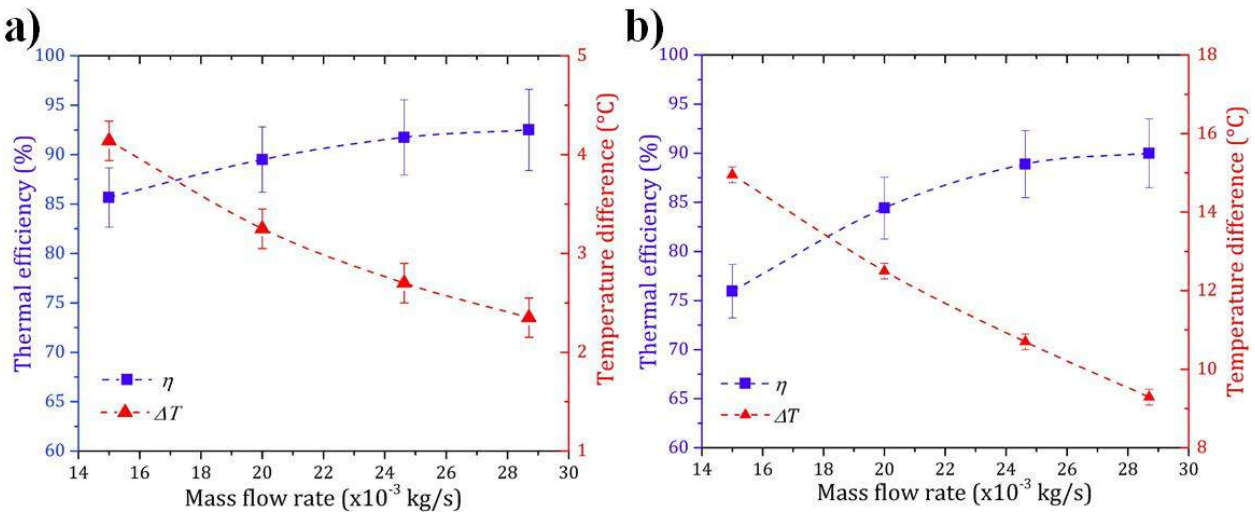

Fig. 5.8. Thermal efficiencies and temperature differences of the test bench as a function of the mass flow rate for: a) LCFL; b) HCFL.

Subsequently, to corroborate that the peak flux incident on the coated test plate is in accordance with the required temperature level, measurements were taken with the thermographic camera as

well as with the thermocouples located on the back side of the test plate, as explained in section 5.3.2. Furthermore, temperature experiments were carried out with and without cooling the test plate with the working fluid for determining the maximum temperature generated by the peak flux levels. Fig. 5.9a shows the temperature distribution measured with the thermocouples without applying a mass flow rate (0 kg/s) depicted with the red rhombi. As well, this graph shows the temperature distribution when a mass flow rate of $24.63 \text{x} 10^{-3} \pm 0.39 \text{ x} 10^{-3}$ kg/s is applied (blue circles). It can be clearly observed the decrease in temperature level produced by the cooling effect of the HTF, so guaranteeing the test bench design viability. This result shows a reduction in peak temperature from 178 ± 3 °C to 116.4 ± 2 °C with mass flow rate from 0 kg/s to $24.63 \text{x} 10^{-3}$ kg/s, selected mass flow rate from the sensitivity heat transfer analysis.

Fig. 5.9b shows the temperature measured with the thermographic camera taking only into consideration the average temperature inside the white circle named *test plate* which corresponds to the irradiated area of interest of 100 mm in diameter. Subsequently, by applying a HCFL, a maximum temperature of 519 ± 10 °C was achieved without applying a mass flow rate, as shown in Fig. 5.9c with red rhombi. Correspondingly, Fig. 5.9c shows the temperature distribution profile (blue circles) achieving a maximum temperature of up to 252 ± 5 °C by implementing a water mass flow rate of $24.6 \text{x} 10^{-3}$ kg/s. Additionally, Fig. 5.9d shows the average temperature taken with the thermographic camera when the selected mass flow rate is applied. Although the temperature on the test plate is significant, the boiling point of the water is not surpassed. The main reason is that the recirculation of the water, the insulated water reservoir with capacity of 150 L, as well as the circulating chiller, and the control on the volumetric flow (L/min), avoid the phase change of water. Additionally, the temperature level on the calorimeter measured with the thermocouple #6 (see Fig. 5.5) does not reach water's boiling point, neither at LCFL (27°C on calorimeter) nor at HCFL (66 °C on calorimeter).

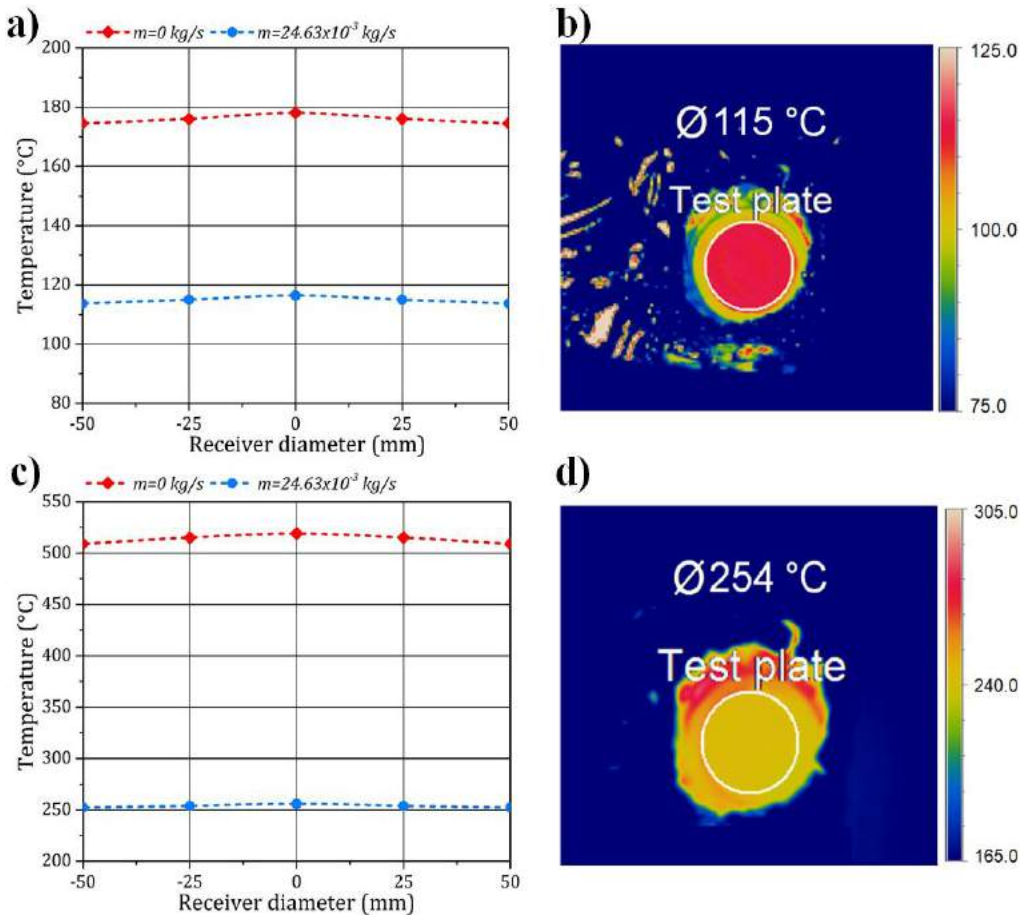

Fig. 5.9. a) Temperature distributions at the back surface of the coated test plate for LCFL; b) average temperature over the test plate for a LCFL taken with the IR camera; c) temperature distributions at the back surface of the coated test plate for HCFL; d) average temperature over the test plate for a HCFL taken with the IR camera.

To calculate the energy balance (Eq. (5.6)), the temperature difference between both inlet T_i and outlet T_o water temperatures at the calorimeter were measured for this purpose. Fig. 5.10a depicts the temperature profiles of T_i and T_o, their temperature difference ΔT and the volumetric flow of 1.49 L/min (24.63×10^{-3} kg/s) when the Pyromark coating is implemented. For a LCFL, the inlet and outlet water temperatures and the temperature difference were up to 20.1 ± 0.15 °C, 22.8 ± 0.15 °C and 2.7 ± 0.2 °C, respectively. From this graph, it can be observed the rising in temperature T_o as the heat from the input power is transferred to the HTF in a span of 5400 s (1.5 hrs.). Correspondingly, Fig. 5.10b shows the trend of the inlet and outlet water temperature, as well as the temperature difference ΔT for the case of HCFL, having values of 20.21 ± 0.15 °C, 30.91 ± 0.15 °C and 10.7 ± 0.2 °C, respectively. It can be noticed that the maximum achieved temperature

difference ΔT occurs at approximately 1000 s (16 min) until stabilizing at 30 minutes. Furthermore, during the experimental analysis, T_i and T_o achieved temperature levels between 20 °C to 31 °C, so thermo-physical properties of the water such as water density ρ_w and specific heat capacity C_{pw} were averaged at 997 kg/m^3 and 4180 J/kg °c for the energy balance.

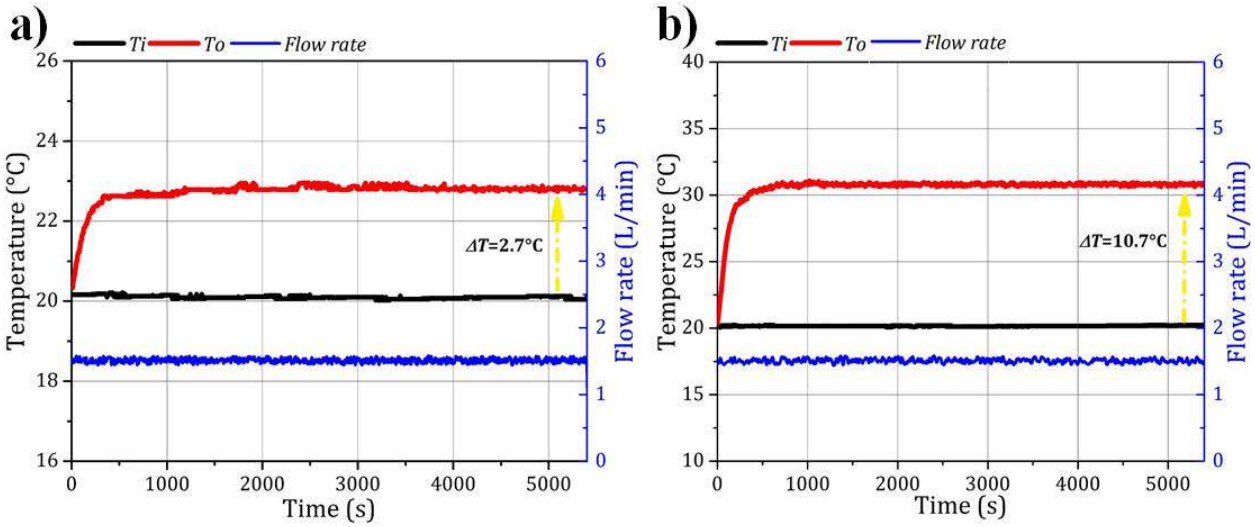

Fig. 5.10. Water temperature profiles of: T_i, T_o,and the volumetric flow of 1.48 L/min ($24.6x10^{-3}$ kg/s) when the Pyromark coating is implemented. a) at LCFL; b) at HCFL.

Fig. 5.11 shows the trend of the heat transferred to the working fluid as the input power is absorbed and converted into useful work Q_{abs}. The temperature reached on the receiver surface is about 115±2 °C for the case of the LCFL, see Fig. 5.9b. Based on the energy balance, the absorbed thermal power from the test plate is up to 277.97±14 W when a radiative input power of 303±9 W is applied. Therefore, the thermal efficiency η_{abs} is quantified in 91.74±3.8% which can be observed in Fig. 5.11a with a similar trend of the absorbed power due to the proportionality in Eq. (5.7). Fig. 5.11b shows the growth trend of the thermal power converted into useful work, which is calculated in a maximum value of 1098.6±26 W for the HCFL, reaching a temperature over the test plate of about 254±4 °C (see Fig. 5.9d) by implementing a radiative input power Q_{in} of 1238±37 W. Accordingly, a thermal efficiency of 88.69±3.41% is quantified, resulting in an efficiency reduction of 3.3% when compared with the thermal efficiency obtained at LCFL (within the uncertainty level). This slight reduction in efficiency is thought to happen due to the increment in thermal losses as the temperature over both the receiver surface and the test bench rise, which

generates the reduction of heat transferred to the working fluid based on the thermal balance described in Eq. (5.8).

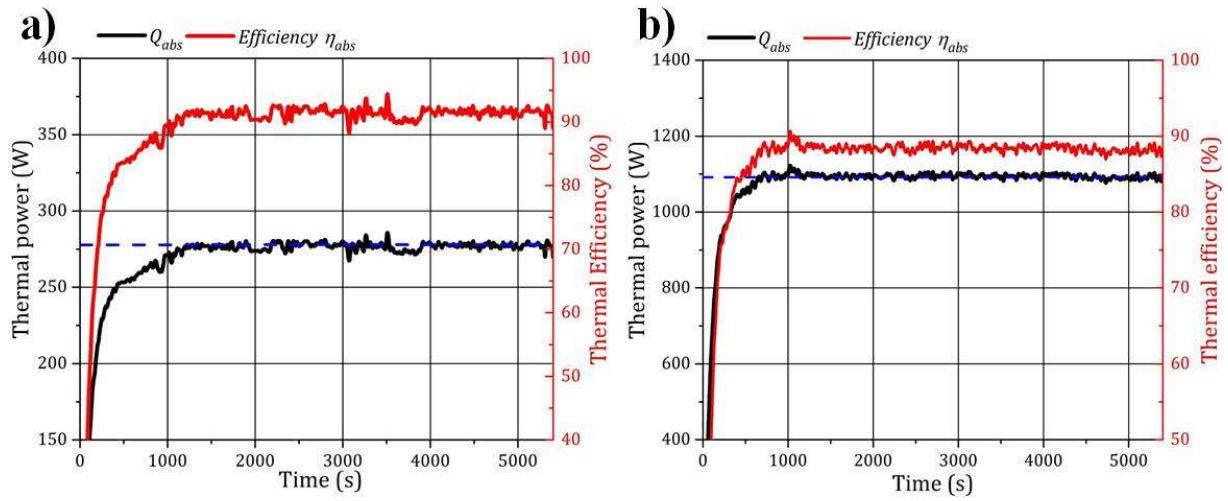

Fig. 5.11. Transferred thermal power and thermal efficiency as the input power is absorbed by the test plate covered with Pyromark: a) at LCFL; b) at HCFL.

In order to evaluate the test bench performance when the thermal losses increase, four different radiative input powers were established at 303±9 W, 750.97±22 W, 1238±37 W and 1690±50 W, while maintaining the mass flow rate constant at 24.63x10^{-3} kg/s. From Fig. 5.12a, it can be observed the increase in thermal losses as the absorber receiver heats up, presenting a curve with exponential growth. For each implemented flux level, overall thermal losses were quantified with Eq. (5.8) and were plotted versus the temperature difference between the absorber surface temperature T_s and the room temperature T_a once the experiments reached the steady state (1.5 hrs.). Accordingly, the overall thermal losses were calculated in 12.9±1 W, 44.63±3 W, 90.88±4 W and 155.4±6.1 W, increasing as the temperature difference ($T_s - T_a$) increased. From this result, a third degree polynomial curve fit was performed, obtaining an R^2 of 0.9982, as shown in Fig. 5.12a. In parallel, as the thermal losses rise with the increment of the temperature over the test plate, the heat transfer performance is affected by a drop in thermal efficiency. Fig. 5.12b shows the drop in thermal efficiency for the 4 different input power levels, obtaining efficiencies of up to 91.74±3.8%, 90±3.2%, 88.69±3.41% and 86.8±2.8%, respectively. This reduction in absorption efficiency presents a linear trend with an R^2 of 0.98853. The principal factor for the drop in efficiency is because the working fluid removes heat from the receiver with a constant mass flow rate for all the different levels of input power, making difficult to cool the receiver at higher peak

flux levels. This limitation of cooling the receiver properly generates a rise in temperature not only on the test plate, but also into the test bench, which increase the overall thermal losses. It is worth mentioning that the thermal losses reported in Fig. 5.12a are evaluated for all the calorimetric test bench, not only for the implemented coating. On the other hand, the heat losses exhibited by the test bench can be reduced by properly adjust the mass flow rate of the HTF, which will be discussed in the next sections.

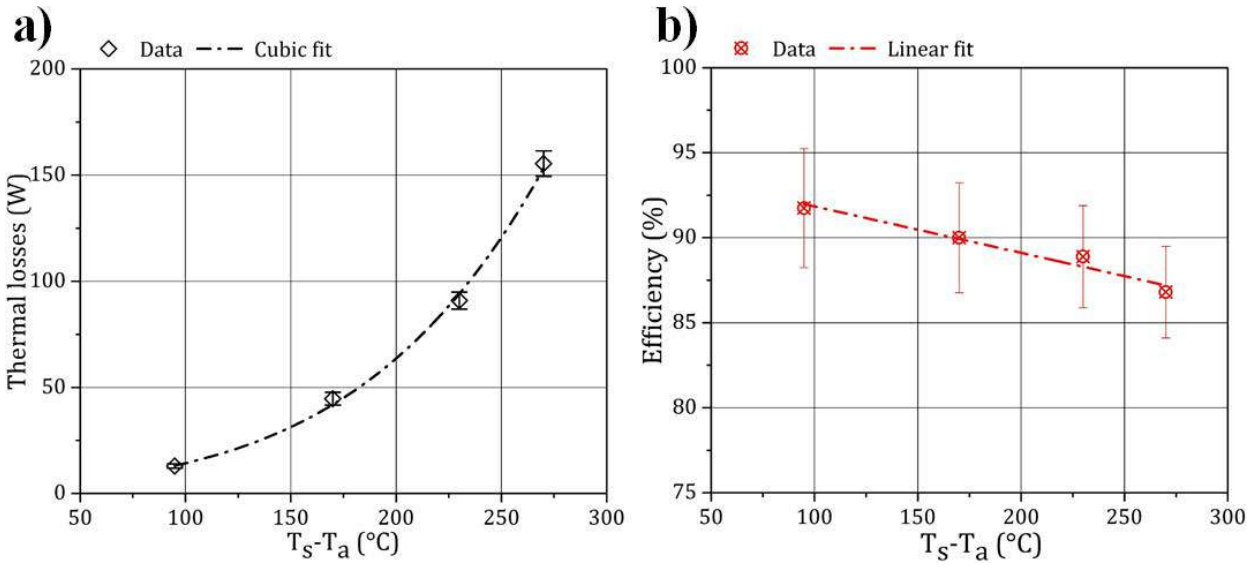

Fig. 5.12. a) Overall thermal losses of the test bench as the test plate is heated up; b) thermal efficiency trend of the test bench as a function of $(T_s - T_a)$.

The coating efficiency of Pyromark for a LCFL and HCFL was quantified with the figure of merit (Eq. (5.9)) obtaining values of 92.3±2.7% and 92.6±2.7%, respectively. It can be observed that the efficiencies in both cases are practically the same, with an increase of 0.3% for HCFL. On the one hand, this effect could be happening due to the fact that the coating efficiency responses better at higher flux levels when the operating temperature is in the range implemented in this study [83]. On the other hand, the solar absorptance is being considered the same throughout the experimental campaign, see Table 5.1. In order to analyze the solar absorptance of the coating after being irradiated with a HCFL, measurements with the spectrophotometer were conducted for this purpose. Fig. 5.13 illustrates the comparison of the spectral absorptivity of the Pyromark coating before and after the experimental campaign with a HCFL. It can be clearly observed a reduction of absorptivity in the range of 300-1750 nm, while an increase is noticed between 1750-2500 nm. By using Eq. (5.2), the solar absorptance weighted against the standard AM1.5 is calculated,

obtaining a value of 0.94±0.001, presenting a reduction of 1.22% after irradiation. Spectral measurements of different samples irradiated with a LCFL did not show a significant change on the solar absorptance. Therefore, values of solar absorptance of 0.9517±0.001 and 0.94±0.001 were used for calculating the coating efficiency for LCFL and HCFL, obtaining values of 92.3±2.7% and 91.6±2.7%, respectively, with a reduction of 0.758%.

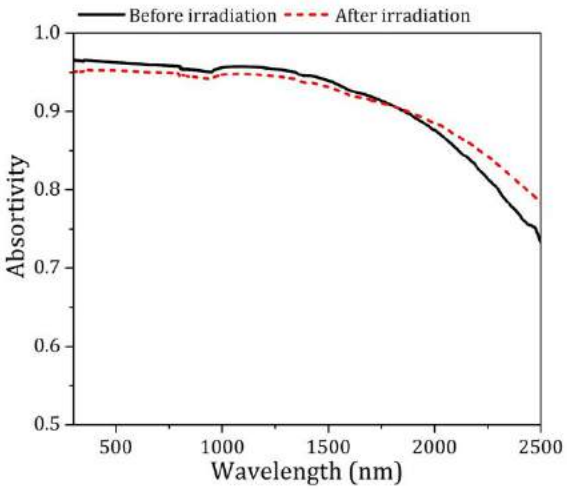

Fig. 5.13. Comparison of the spectral absorptivity of Pyromark before and after being irradiated.

Furthermore, it can be noticed that the coating efficiency is higher than the thermal efficiency obtained with Eq. (5.7). This is mainly due to fact that the high radiative flux $\bar{q}$ and the high absorptance level of the coating have more impact than the energy losses at these temperature levels between 100-250 °C, as explained by Cindrella et al. [141]. For the case of LCFL, the expected efficiency of 92.3±2.7% (coating efficiency) is reduced to 91.74±3.8% (thermal efficiency), only 0.6% less, which is within the uncertainty range of the measurements. For the case of HCFL, the expected efficiency is reduced by 3.17%, which is explained by the heat losses analysis presented in Fig. 5.12. Heat losses are mainly due to conduction into the mass of the testing system since the mass flow rate is kept constant.

With regard to the maximum efficiency of the test bench, the efficiency of a Carnot heat engine is evaluated with Eq. (5.10). From this evaluation, the Carnot efficiency of the test bench for a LCFL is up to 24.48±0.24%, while for a HCFL the efficiency is 43.45±0.43%. Then, it can be observed that the Carnot efficiency is mainly influence by higher temperatures reached on the receiver surface; as the receiver temperature T_s increases, the system's Carnot efficiency increases as well.

However, as the temperature on the test plate rises, the energy losses of the coating would also rise due to dependence with temperature to the fourth power $T_s{}^4$, see Eq. (5.9). Therefore, the system will have a limit temperature at which the maximum efficiency would begin to decrease [144]; but this effect was not observed in the temperature range implemented in this study. Based on the heat transfer evaluation of the test bench, a good performance is observed for carrying out the thermal efficiency comparison with different SACs at the proposed heat flux levels. Table 5.2 depicts the global parameters quantified for the performance evaluation of the test bench when the Pyromark coating is applied for the analysis.

Table 5.2. Global parameters of the test bench evaluation with the use of the coating Pyromark.

Parameter	Value at LCFL	Value at HCFL
$\boldsymbol{m}$	24.63x10^{-3} ±0.39 x10^{-3} kg/s	24.63x10^{-3} ±0.39 x10^{-3} kg/s
$\boldsymbol{T_i}$	20.1±0.15 °C	20.21±0.15 °C
$\boldsymbol{T_o}$	22.8±0.15 °C	30.91±0.15 °C
$\boldsymbol{T_s}$	115±2 °C	254±5 °C
$\boldsymbol{C_{pw}}$	4180 J/kg°C	4180 J/kg°C
$\boldsymbol{\rho_w}$	997 kg/m^3	997 kg/m^3
$\boldsymbol{Q_{in}}$	303±9 W	1238±37 W
$\boldsymbol{Q_{abs}}$	277.97±14 W	1098±26 W
$\boldsymbol{Q_{loss}}$	12.9±1 W	90.88±4 W
$\boldsymbol{\eta_{abs}}$	91.74±3.8%	88.69±3.41%
$\boldsymbol{\eta_{coating}}$	92.3±2.7%	91.6±2.7%
$\boldsymbol{\eta_{Carnot}}$	24.48±0.2%	43.45±0.4%

5.4.2 Heat transfer performance and efficiency comparison with different SACs

With the use of the four different commercial SACs, in addition to the soot-based coating (SFB) described in section 5.2.2, the comparison of the absorbed thermal power performance and thermal efficiency was conducted with the aid of the test bench. To carry out the radiative-to-heat transfer analysis, the experiments were performed by using the characterized flux levels of LCFL and HCFL described in Table 5.2, as well as a mass flow of 24.63x10^{-3} ±0.39x10^{-3} kg/s. Additionally, an uncoated plate (only aluminum) was utilized for analyzing the thermal efficiency of the substrate when an absorber coating is not applied.

Temperature differences measured with the different SACs are shown in the Fig. 5.14a presenting a quite similar growth trend, except for the uncoated aluminum plate. From this graph, the absorber coating with the highest temperature difference was the Pyromark coating, achieving a temperature

difference ΔT of 2.7±0.2 °C. Correspondingly, the temperature differences measured with the other SACs were 2.6±0.2 °C, 2.52±0.2 °C, 2.49±0.2 °C and 2.45±0.2 °C for SFB, Thurmalox250, Solkote and Comex, respectively. For the case of the uncoated substrate, the temperature gradient ΔT was only of 1±0.2 °C, which is an expected outcome due to the fact that the reflectivity factor of the aluminum surface generates a higher energy losses. Based on these results, it can be observed a quite narrow range of temperature differences between 2.7 to 2.45 °C for the coatings under test at the LCFL. Fig. 5.14b shows the absorbed thermal power profiles quantified with the different samples under analysis. It can be clearly observed that the thermal power profiles present a similar trend as the respective temperature difference trends because the thermal power Q_{abs} is directly proportional to the ΔT and to the mass flow rate, see Eq. (5.6). The absorber coating with the highest heat transfer performance was Pyromark with a transferred thermal power of 277.97±14 W, followed by SFB, Thurmalox, Solkote, Comex and aluminum with 267.67±13 W, 259.88±13 W, 256.35±13 W, 252.23±13 W and 102.95±5 W, respectively. From this graph, the SFB coating exhibited an excellent heat transfer performance at this flux level, with an absorbed power of 267.67±13 W, higher than most of the commercial coatings and only 3.7% less than the Pyromark performance, which is within the uncertainty range of the energy balance. By comparing the heat transfer performance of the analyzed absorber coatings, it can be observed a quite similar behavior with a difference in percentage between the highest and the lowest absorbed power of 9.2%. As a result at this LCFL, it could be inferred that; the higher the solar absorptance the better the efficiency, neglecting the thermal emittance [141].

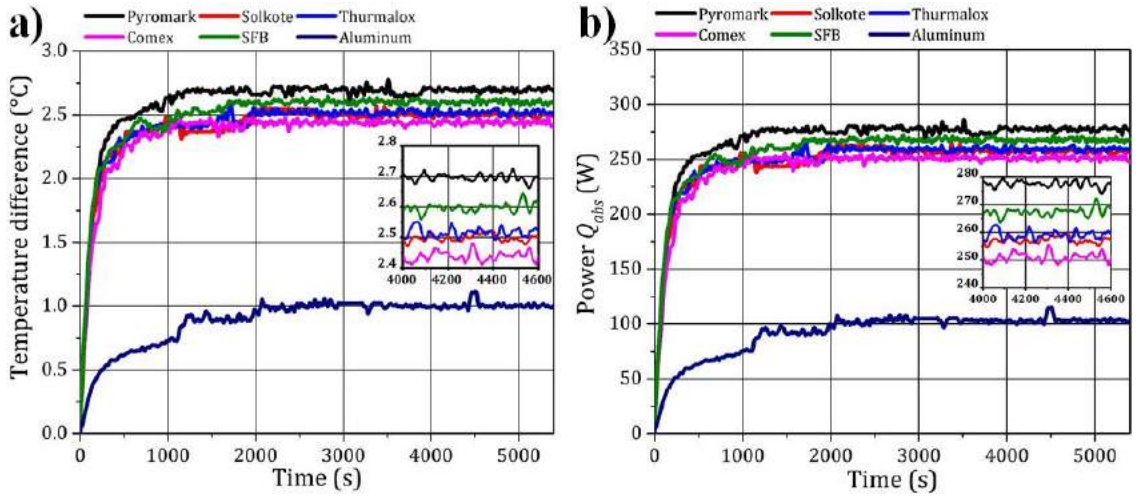

Fig. 5.14. a) Temperature difference ΔT evaluated for the 6 samples at LCFL; b) thermal power profiles Q_{abs} at LCFL.

Fig. 5.15a shows the temperature difference comparison of the different samples under test, achieving a maximum temperature difference of 10.7±0.2 °C with the Pyromark coating at HCFL. The temperature differences ΔT obtained at this flux level were 10±0.2 °C, 9.7±0.2 °C, 8.9±0.2 °C, 8.75±0.2 °C and 3±0.2 °C for the coatings Thurmalox, Solkote, Comex, SFB and the uncoated substrate, respectively. In contrast with the ΔT obtained for the LCFL, the temperature gradients exhibited a slightly wider range between coatings. From Fig. 5.15a it can be seen that the SFB coating achieved an excellent thermal performance similar to the implemented commercial coatings. Nevertheless, it was observed that the SFB coating started to present delamination problems after the test plate reached a surface temperature of 180 °C, achieving a maximum useful work of 900.84±25 W, as depicted in Fig. 5.15b. This coating detachment could be produced not only by the lower thermal tolerance compared to the commercial coatings, but also by the degradation of the coating's binder, which occurs while the test plate is being irradiated [145]. Furthermore, this result implies that the maximum temperature resistance of the SFB coating could be determined at ≤150 °C. Therefore, it could be inferred that this coating could have a great potential in solar-thermal applications at low-medium temperature level (60-150 °C) such as: flat plate collectors, CPC systems and small-scale PTC [27]. The useful work absorbed by the samples under test, as depicted in Fig. 5.15b, are; 1098.6±25.2 W, 1029.53±25.73 W, 998.64±25.96 W, 916.28±25.2 W, 900.84±25 W and 298±19 W, for the coatings Pyromark, Thurmalox, Solkote, Comex, SFB and the aluminum plate, respectively. From this result, the commercial coatings Pyromark and Thurmalox were the coatings with better performances, presenting a difference in collected power of 6.3% between them. In spite of having the lower thermal emittance (0.27), the Solkote coating presented a lower efficiency than Pyromark and Thurmalox. This is mainly due to the fact that its solar absorptance is 0.92, 2.1% less than Pyromark, and this is the critical parameter for achieving a higher efficiency, as aforementioned. Based on this, the performances of the Comex coating can be explained by the lower absorptance level of 0.85. Although having similar absorptivity (~0.92) and Solkote less emissivity (0.27), Thurmalox achieved a better performance. In this context, critical parameters during the application procedure of the SACs can have a significant impact on the final performance such as: the coating thickness, easy adhesion to the substrate, the excellent acrylic base and the high temperature resistance of each coating. Moreover, for high oxidation environments at high heat flux levels, the improvement of the thermal efficiency with the aid of a selective coating has been reported to be of ~0.8% for an emissivity range of 0.9

to 0.5 [25]. Therefore, it could be inferred that external elements involved during experimentation, as well as the relationship between absorptivity and emissivity with respect to the optical-thermal performance, could be analyzed indirectly with the calorimetric approach reported in this study.

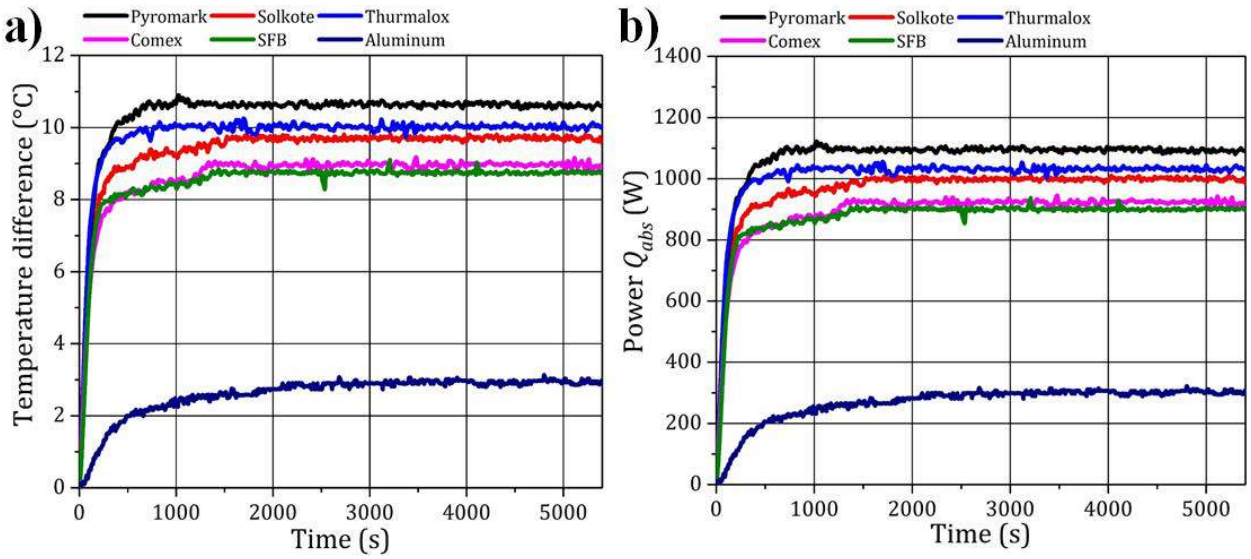

Fig. 5.15. a) Temperature difference ΔT evaluated for the 6 samples at HCFL; b) thermal power profiles Q_{abs} at HCFL.

In order to evaluate the optical properties of each coating before and after being irradiated with a HCFL, absorptivity measurements were taken and compared. Fig. 5.16 shows the change in spectral absorptivity that the coatings experience before (denoted with 1) and after (denoted with 2) the experimental campaign. It can be observed that the coating Solkote reduces its absorptivity level between 700 to 1500 nm while Thurmalox keeps unchanged throughout the wavelength range. This could explain the better performance obtained from Fig. 5.15. Furthermore, the Comex coating seems to improve slightly the spectral absorptance between 300 to 700 nm. Previous studies have reported that improvements in optical efficiencies of SACs can occur during experimentation due to a curing phenomenon on the coating that emerges at certain levels of irradiance and temperature [94]. Therefore, the change in absorptivity level of Comex could be explained due to a better adhesion to the substrate during the experimentation process at high flux levels. By calculating the solar absorptance, the change experienced by each coating was 1.22% (reduction) for Pyromark, 0.28% (reduction) for Solkote, 0.03% (reduction) for Thurmalox, 0.247% (increase) for Comex and 0.28% (reduction) for SFB.

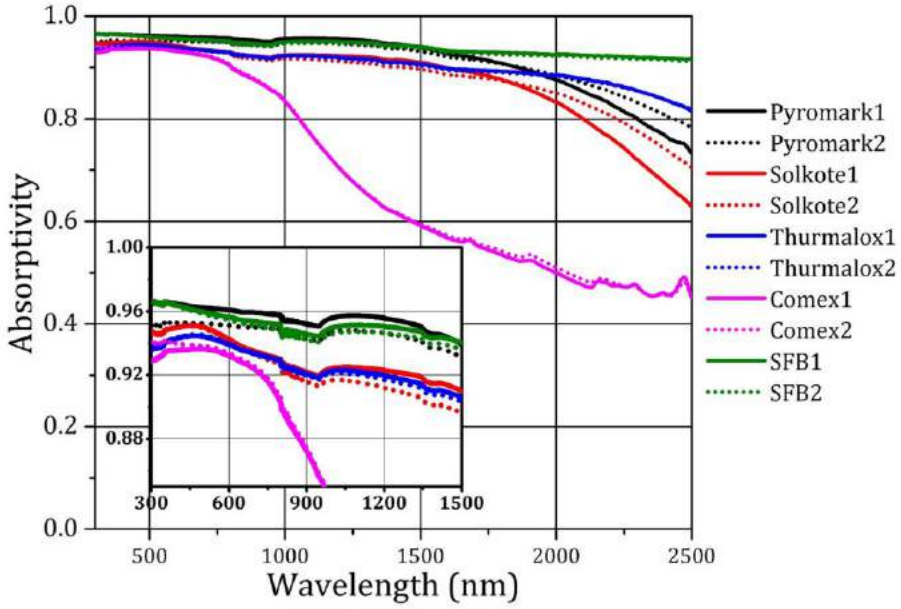

Fig. 5.16. Comparison of the spectral absorptivity of the SACs before (1) and after (2) being irradiated with a HCFL.

For LCFL, the maximum thermal efficiencies η_{abs} of the analyzed coatings were calculated with the aid of Eq. (5.7) and results are shown in Fig. 5.17a along with the corresponding temperature differences. From Fig. 5.17a, it can be observed that Pyromark achieves the highest thermal efficiency compared with the other SACs, reaching 91.74$\pm$3.8% of efficiency. Regarding the other samples under test, the calculated efficiencies were up to 88.33$\pm$4%, 85.77$\pm$4.1%, 84.6$\pm$4.1%, 83.24$\pm$4.1%, and 33.97$\pm$1.7% for SFB, Thurmalox, Solkote, Comex and the uncoated substrate, respectively. From Fig. 5.17a, it can be clearly observed that the most significant parameter for the achieved thermal efficiency is the temperature difference obtained with each coating. Therefore, for the same experimental conditions of flux and mass flow rate, the higher the temperature ΔT, the better the thermal efficiency η_{abs}. Correspondingly, the maximum thermal efficiencies reached with a HCFL were compared and are depicted together with the respective temperature difference in Fig. 5.17b. Similar to the LCFL, the Pyromark coating achieved higher thermal efficiency than the other commercial coatings under the experimental conditions presented in this study. Accordingly, the thermal efficiencies obtained with the samples under analysis are 88.69$\pm$3.41%, 83.16$\pm$3.24%, 80.61$\pm$3.14%, 74$\pm$2.96%, 72.69$\pm$2.9% and 24.1$\pm$1.6%, corresponding to the coatings Pyromark, Thurmalox, Solkote, Comex, SBF and the aluminum

plate. In contrast with the LCFL, the thermal efficiencies decreased significantly between 4% to 12% less when a HCFL was applied. This efficiency reduction could be occurring due to an ineffective capability of the working fluid to remove heat from the absorber receiver as the absorber is heated up when going from a LCFL to a HCFL, while maintaining constant the mass flow rate. Hence, higher thermal losses can be generated, reducing the heat transfer performance, as well as the thermal efficiency. On the one hand, by rising the mass flow rate, the cooling effect on the calorimeter can be improved, reducing the overall thermal losses, enhancing the heat transfer performance (see Fig. 5.8) as well as, protecting the tandem substrate-coating from degradation. On the other hand, the operating conditions for the calorimetric experiments have the same impact for all of the samples under analysis. Hence, under the same controlled conditions such as flux and mass flow rate, the thermal losses will affect each sample depending on their individual characteristics and performances. Therefore, a direct coating comparison about the flux acceptance and performances, under the operating conditions presented in this study, can be assessed. As aforementioned, the analyzed commercial coatings are fabricated by manufacturers as a solution for specific solar-thermal applications. Consequently, the performances achieved with each sample are only parameters to identify the possible efficiency achievable when a specific commercial coating is used under the operating conditions presented here for an open environment.

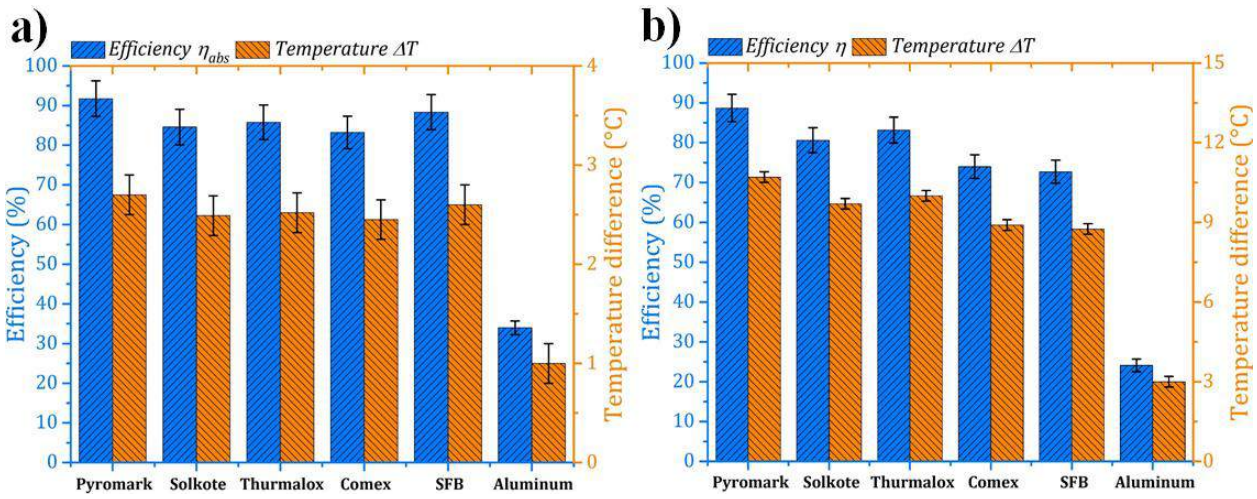

Fig. 5.17. Thermal efficiency comparison between the analyzed SACs and the uncoated substrate: a) at LCFL; b) at HCFL.

Table 5.3 shows the results obtained from the heat transfer performance comparison and thermal efficiency by using the LCFL and HCFL. From Table 5.3, it can be noticed that the efficiencies

$\eta_{coating}$ for all the analyzed coatings present slight reductions from the low flux level to the high flux level. Furthermore, it can be observed that the coating efficiencies $\eta_{coating}$ reached higher levels than those obtained for the thermal efficiency η_{abs} at HCFL, because the heat transfer process of the working fluid is not involved in the quantification of $\eta_{coating}$. Therefore, the main source of thermal losses at high flux level can be attributed to the conduction losses through the test bench structure, which involves the working fluid and the thermal efficiency.

Table 5.3. Results obtained from the thermal efficiency comparison with the analyzed SACs.

SAC	Value at LCFL				Value at HCFL			
	ΔT (°C)	Q_{abs} (W)	η_{abs} (%)	$\eta_{coating}$ (%)	ΔT (°C)	Q_{abs} (W)	η_{abs} (%)	$\eta_{coating}$ (%)
Pyromark	2.7±0.2	277.97±14	91.74±3.8	92.3±2.7	10.7±0.2	1098±26	88.69±3.4	91.6±2.7
Solkote	2.49±0.2	256.35±13	84.6±4.1	91.8±2.7	9.7±0.2	998.6±26	80.61±3.14	91.4±2.7
Thurmalox	2.52±0.2	259.88±14	85.77±4.1	91.2±2.7	10±0.2	1029.5±25	83.16±3.24	91.6±2.7
Comex	2.45±0.2	252.23±13	83.24±4.1	82.3±2.6	8.9±0.2	916.28±25	74±2.96	83.2±2.5
SFB	2.6±0.2	267.67±13	88.33±4	92.3±2.7	8.75±0.2	900.84±25	72.69±2.9	92.9±2.7

From these results, it can be noticed that the Comex coating has exhibited a great heat transfer performance in both LCFL and HCFL when compared to the other commercial coatings. Based on its easy application, low-cost and thermal efficiency, the Comex coating could be an interesting and practical solution in CSP applications when requiring re-coating the metal-based solar receiver. In the case of the experimental SFB coating, its heat transfer performance is considered acceptable on the basis that, for LCFL its thermal efficiency was only 3.7% less than Pyromark (the highest efficiency). Even though the test plate suffered from delamination, for HCFL the SFB's thermal efficiency achieved up to 72.69%, only 9.5% less than Solkote. Moreover, the soot-based coating can provide a sustainable strategy for the reutilization of solid combustion waste, in addition to its low-cost, easy fabrication and application. Therefore, the SFB coating could represent a promising alternative for its utilization in SHIP applications at low-to-medium temperature levels of about ≤150 °C. Nonetheless, before the SFB could be integrated on the market as an SAC alternative, further research is required for improving critical properties of this coating such as; temperature tolerance, hardness and adhesion, as well as optical-thermal properties.

5.5 Summary

In the present Chapter, the development of a calorimetric test bench for the flux absorption assessment of SACs has been reported and experimentally evaluated. The test bench was designed based on a flat calorimeter made of aluminum for reducing complexity in both manufacturing and heat transfer quantification. The test bench was coupled with the developed HFSS for achieving a well-controlled laboratory environment for conducting calorimetric experiments. Subsequently, two different heat flux input levels, called LCFL and HCFL, were established with the solar simulator at LCFL= 100 ± 3 kW/m^2 and HCFL= 415 ± 12 kW/m^2. To evaluate the heat transfer performance of the test bench, the standard coating Pyromark was employed for this purpose, obtaining a thermal efficiency of 91.74% for the LCFL and an 88.69% for the HCFL. Furthermore, an experimental campaign was carried out by adjusting the flux delivered by the solar simulator at 4 different levels. By increasing the concentrated peak flux and keeping the mass flow rate at the same level, the thermal losses of the calorimetric test bench were analyzed, observing a reduction in thermal efficiency as the temperature over the test plate (substrate-coating) increased. This experimental conditions provided the possibility to analyze performances and efficiencies of the different SACs due to the fact that the maximum efficiency is achieved based on the individual qualities of each coating.

For the thermal efficiency comparison, the Pyromark coating resulted in the highest thermal performance, which can be inferred due to its high temperature resistance (1000 °C) and high solar absorptance. Furthermore, it was observed that the coating Comex presented quite similar performance than the commercial coatings Thurmalox and Solkote, even when this coating is not widely known as an absorber coating for low-medium temperature CSP applications. From this experimental campaign, it was stated that the analyzed coatings have been fabricated by the manufacturer for specific purposes, and this comparison is only for the evaluation of their particular qualities under specific conditions presented in this study. Additionally, the thermal efficiency comparison was carried out in order to analyze the performances and flux acceptance of the new SFB coating, a byproduct of combustion waste. The SFB coating exhibited a reasonable good performance compared with the commercial coatings, making it a promising coating for its possible use in industrial process heating operations at low-medium temperature levels, possibly

in the range of 50-150 °C. However, further research is required for enhancing the quality of this experimental absorber coating.

Chapter 6. Conclusions and future work

6.1 High flux solar simulator

In this doctoral study, the development of a 7 (x2.5 kW_e) xenon lamps based high-flux solar simulator has been theoretically analyzed by using the MCRT technique. Furthermore, the solar simulator characterization has been experimentally conducted by implementing the indirect flux mapping technique. From the prediction of the flux characteristics, the solar simulator reached a source-to-target radiative transfer efficiency of 42%, which was found to be the maximum level for the selected focal distance of 2000 mm. Furthermore, the theoretical electrical-to-radiative conversion efficiency was predicted in 34.5% for a target diameter of 120 mm. The validation of the ray-tracing model was conducted by the flux mapping technique, achieving a measured total peak flux of 1327 ± 58 kW/m^2, presenting excellent agreement with simulations, with a relative error of 1.5%. Moreover, the intercepted radiative power, measured on a circular spot distribution of 120 mm, was up to 5.11 ± 0.22 kW, corresponding to 3% of relative error with the simulation results. Additionally, the images obtained with the thermographic camera provided important information in terms of the temperature that a single radiation unit can achieve when using a high temperature commercial coating.

The development of the solar simulator has been described taking into detail geometrical parameters for the proper optical design. This makes it a unique facility in its type, particularly in Latin America. Furthermore, the optical design procedure can provide guidance for constructing new solar simulators by properly modeling the lamp-reflector array based on specific design requirements. Based on the research conducted in this doctoral thesis, the heat flux capabilities of the developed solar simulator make it a valuable technology for researching solar-thermal and thermochemical processes in a well-controlled indoor environment. Therefore, the construction of the HFSS opens up the possibility to carry out new and innovative research about the effects that high concentrated flux levels can have on various solar components, both those existing on the market and those developed within the research center.

6.2 Shutter curtain for flux modulation

In order to modulate effectively the radiative flux output of the HFSS, an optical optimization through the use of the MCRT technique has been conducted and experimentally validated. First, 4 different SCs were proposed in order to accomplished this assignment. Theoretical results revealed

a radiative loss level of 47% when the manufactured flat SC was implemented for modulation, whilst levels of 9%, 14% an 7% were predicted with shutter designs #2, #3 and #4, respectively. From this ray-tracing analysis, the SC4 achieved the best performance in flux regulation, followed by the shutter #2. Although shutter 4 presented a better flux regulation, the shutter #2 provided a less mechatronic complexity for both designing and manufacturing, making it a suitable shutter alternative for regulating the radiative flux with lower energy losses. Furthermore, it was shown that the concentrated irradiance can be adjusted by modifying the position of the target further back the focal point. The effect that relocating the target can offer is to modify the peak flux and the flux spot diameter while keeping constant the intercepted power, providing the possibility to carry out different solar-thermal applications where large receiver areas at a lower peak flux levels are required.

From the experimental campaign with the flat shutter, it was demonstrated an excellent agreement between the ray-tracing analysis and the flux modulation measurements with a single lamp-reflector unit. For instance, the relative error was found within the 4.3% for most of the studied cases. Based on this numerical analysis and experimental validation, the SC can be considered a competitive tool for achieving a wide range of flux levels at high resolution, while operating the light sources in a continuous and stable manner. Additionally, the validation of the ray-tracing model provided substantial results that contributed with the fabrication of an efficient shutter curtain called SC5. Therefore, by effectively adjusting the delivered concentrated irradiance, a wide variety of solar-thermal research can be carried out for applications at low, medium and high temperature levels.

6.3 Calorimetric test bench

In this doctoral research, the development and evaluation of a test bench for the analysis of different solar absorber coatings has been carried out. The performance evaluation of the test bench was conducted by applying the standard coating Pyromark over an aluminum substrate. A sensitivity analysis of the heat transfer performance as a function of the mass flow rate was carried out. From this sensitivity analysis it was observed that by increasing the mass flow rate the thermal efficiencies are increased, while the temperature differences are reduced due to the cooling effect. Though the efficiencies are improved with greater velocities of flow rates, the reduction in the temperature differences involves a rise in the overall uncertainty. By establishing a constant mass

flow rate, the outcomes showed an absorbed thermal power of 277.97±14 W for an input power of 303±9 W, obtaining a thermal efficiency of 91.74%. Correspondingly, for an input power of 1238±37 W the absorbed power was up to 1098±26 W, with an efficiency of 88.69%. For the performance comparison, 5 different absorber coatings were assessed by implementing a low and high concentrating flux levels, as well as maintaining the selected mass flow rate. For a low flux level, thermal efficiencies were in a very narrow range between 83%-91%, while for a high flux the efficiencies were between 72%-88%. The outcomes also showed that for both low and high concentrating flux levels, the commercial coatings Pyromark and Thurmalox exhibited the higher thermal efficiencies, respectively.

Based on the experimental results, it was demonstrated the possibility to evaluate and compare the performances that different commercial and new absorber coatings can provide. From the experimental outcomes, it was observed that for a low concentrating flux level, the efficiencies are quite similar, inferring that the selection of a SAC can be conditioned by different criteria than a lower thermal emittance or a higher absorptance such as availability, lower cost, non-polluting. Furthermore, it was shown that either with a higher solar absorptance or a lower thermal emittance, the light flux absorption and final efficiency can be affected by other parameters such as the maximum temperature resistance, a better adhesion to the substrate, or a curing reaction during experimentation.

Regarding the SFB coating, experimental results demonstrated the great heat transfer performance that this potential coating have at low concentrating flux level, presenting a thermal efficiency of only 3.7% less than Pyromark. Although the SFB coating presented a delamination issue at a temperature of about 180 °C, this coating showed great qualities in transferring heat to the working fluid. Therefore, and based on its low cost and simple preparation method, the SFB coating could be a promising solar absorber in industrial process heating operations at temperature levels below 150 °C, but further research is required for improving critical properties of this coating.

Finally, this investigation demonstrates that the proposed test bench can be a potential tool for the analysis of solar-thermal materials such as new candidate absorber coatings, metallic substrates for solar receivers and thermal barrier coatings, because it has the versatility to replace the absorber receiver as an interchangeable cartridge. Therefore, the implementation of the test bench along with the solar simulator provide not only a well-controlled solar laboratory, but also an alternative

method for the assessment of solar-thermal technologies, offering the possibility to make further progresses in this research field.

6.4 Future work

In this doctoral thesis, the development of a solar laboratory for well-controlled indoor assessments with different solar-thermal materials was carried out. However, being a multidisciplinary study, certain aspects in the development and/or improvement of the indoor lab facility were not completely covered. In this context, the following points should be addressed as a future work:

- In order to maximize the source to target transfer efficiency, the ellipsoidal reflectors of the solar simulator should be coated with a highly reflective layer that can provide reflectance levels of about >90%. Otherwise, the reflectivity value of the concentrators should be enhanced by improving the polishing technique. If the polishing technique of the reflector is enhanced, its efficiency can be increased considerably, attaining levels of radiative flux closer to that of the theoretical results.

- The indirect flux mapping technique is an excellent approach for obtaining spatial information about the irradiance distribution over the target. However, for avoiding spectral dependences and obtaining information of the transient operation and the intercepted thermal power in terms of heat transfer analysis, the development of a flat-plate copper based calorimeter should be considered as future work. With the combination of both techniques, highly accurate flux measurements could be achieved.

- An important step towards a wide range of radiative flux levels should be the characterization of the flux modulation with the fabricated SC5 for all the lamps in operation.

- Regarding the calorimetric test bench, more high temperature resistant materials such as copper, stainless steel or austenitic alloys can be implemented as the substrate of absorber coatings in order to analyze the radiative-to-heat transfer efficiencies compared with the results obtained for aluminum.

- One of current challenges in CSP applications is the improvement in service life of solar materials. In order to assess the evolution of the optical-thermal properties of absorber coatings and thermal barrier coatings, the future work should include a degradation analysis

by performing accelerated aging cycles with the solar simulator, reaching temperatures of up to 700 °C.

- In parallel with the thermal fatigue failure conducted with the solar simulator, a degradation analysis performed with an accelerated aging chamber could be considered in order to compared the different effects on the absorber coatings when different factors such as dust, moisture, oxidation and vacuum atmospheres are included.

Publications

[1] **Martínez-Manuel L**, Peña-Cruz MI, Villa-Medina M, Ojeda-Bernal C, Prado-Zermeño M, Prado-Zermeño I, Pineda-Arellano CA, Carrillo JG, Salgado-Tránsito I, Martell-Chavez F. A 17.5 kW el high flux solar simulator with controllable flux-spot capabilities: Design and validation study. *Solar Energy* 170 (2018): 807-819.

[2] **Martínez-Manuel L**, Peña-Cruz MI, Pineda-Arellano CA, Carrillo-Baeza JG, May-Arrioja DA. Optical improvement for modulating a high flux solar simulator designed for solar thermal and thermochemical research. *Applied optics*, 58(10), (2019), 2605-2615.

[3] **Martínez-Manuel L**, Wang W, Laumert B, Peña-Cruz MI. Numerical analysis on the optical geometrical optimization for an axial type impinging solar receiver. *Energy*, (2020), 119293.

[4] **Martínez-Manuel L**, Wang W., Peña-Cruz, MI. Optimization of the radiative flux uniformity of a modular solar simulator to improve solar technology qualification testing. Manuscript submitted to *Sustainable Energy Technologies and Assessments*. Manuscript number: SETA-D-20-00895.

[5] **Martínez-Manuel L**, González-Canché NG, López-Sosa LB, Carrillo JG, Wang W, Pineda-Arellano CA, Peña-Cruz, MI. Development of a calorimetric test bench for the assessment of solar absorber coatings under real operating conditions. *Under preparation*.

Solar Energy 170 (2018) 807–819

Contents lists available at ScienceDirect

Solar Energy

journal homepage: www.elsevier.com/locate/solener

A 17.5 kW_{el} high flux solar simulator with controllable flux-spot capabilities: Design and validation study

L. Martínez-Manuel[a], M.I. Peña-Cruz[b,*], M. Villa-Medina[c], C. Ojeda-Bernal[c], M. Prado-Zermeño[c], I. Prado-Zermeño[c], C.A. Pineda-Arellano[b], J.G. Carrillo[d], I. Salgado-Tránsito[b], F. Martell-Chavez[a]

[a] Centro de Investigaciones en Óptica, A.C. Unidad Aguascalientes, Prol. Constitución 607, Fracc. Reserva Loma Bonita, CP 20200, Aguascalientes, Aguascalientes, México
[b] CONACYT – Centro de Investigaciones en Óptica, A.C. Unidad Aguascalientes, Prol. Constitución 607, Fracc. Reserva Loma Bonita, CP 20200 Aguascalientes, Aguascalientes, Mexico
[c] Solara Industries, José Ma. Morelos y Pavón 302, Salto de Ojocaliente, CP 20341 Aguascalientes, Ags, Mexico
[d] Centro de Investigación Científica de Yucatán, Unidad de Materiales, Calle 43 No. 130 x 32 y 34, Chuburná de Hidalgo, CP 97205 Mérida, Yucatán, Mexico

ARTICLE INFO

Keywords:
Solar simulation
Concentrated solar energy
Optical characterization
Radiation assessment

ABSTRACT

A new High Flux Solar Simulator (HFSS) has been designed and built for the research of medium/ high-temperature solar material testing and solar thermochemical processes in Mexico. The HFSS was designed using seven 2.5 kW_{el} Xenon short arc lamps, each close-coupled to a 2 m focal length truncated ellipsoidal specular reflector made of polished aluminum. A Monte Carlo (MC) ray tracing technique was employed to design the shape of the ellipsoidal reflectors. The estimated radiative flux obtained with the MC ray-tracing was 1700 kW m^{-2} peak flux for all the seven lamps in a flux spot of 100 mm in diameter. A peak flux of 267 kW m^{-2} was obtained for a single lamp-reflector unit. The design, dimensions and material specifications are presented. The control system is composed of an attenuator curtain and a servo-controlled dynamic test bench that allows variation of the spot size and irradiance incident in the focal plane. A study to compare the theoretical design and the real ellipsoidal reflector surface was conducted with the use of the photogrammetry technique. This was done in order to know if differences in the theoretical flux compared to that of the measured flux come from defects in manufacturing of the reflector. A data acquisition module and an artificial vision system provide information and allow for a monitoring flux spot. Obtaining an experimental peak flux of 194 kW m^{-2} and a flux spot diameter of 120 mm per lamp, the results were consistent with the desired design. In addition, in order to quantify the risk of our own installation and implement a safety protocol, an experimental campaign of ultraviolet radiation monitoring was conducted; the assessment of ultraviolet radiation shows that the recommended dose per 8 h is exceeded in a few seconds when close to the focal plane (−0.2 m). In this paper, due to extension, preliminary design, construction, and validation of the HFSS are presented.

1. Introduction

Concentrating Solar Power (CSP) systems use mirrors and lenses to concentrate and focus sunlight onto a receiver. The concentrated sunlight produces thermal energy that can be used in a wide variety of applications: e.g. solar heat applications for industrial processes, electricity generation or thermochemical processes, among others (Wieckert et al., 2002; Kräupl and Steinfled, 2002). CSP plants are an attractive alternative to traditional fossil fuel power plants; being an environmentally benign source of energy, they do not emit pollutants and do not consume other fuels besides sunlight.

CSP systems also have the great advantage of power "dispatchability", by means of thermal energy storage technology. Thermal Storage (TES) allows for the ability to vary energy production in periods of high volume and convert it into electricity when it is required. Due to the available energy storage, these plants can operate in cloudy weather and after sunset, providing a constant energy reserve and a more stable service (Denholm and Mehos, 2015). Another challenge to overcome in CSP technology is the receiver lifespan and performance. The solar receivers work in an environment of high-energy flux with huge thermal stress. Due to this thermal stress, the development of new high-temperature resistant, high-optical absorptivity and long life service materials are mandatory to achieve the success of this technology. Another trendy application of CSP technology is the production of alternative fuels through the use of a high temperature solar chemical reactor, also known as solar fuels.

* Corresponding author.
E-mail address: mipec@cio.mx (M.I. Peña-Cruz).

https://doi.org/10.1016/j.solener.2018.05.088
Received 6 March 2018; Received in revised form 26 May 2018; Accepted 28 May 2018
0038-092X/

Research Article Vol. 58, No. 10 / 1 April 2019 / Applied Optics 2605

applied optics

Optical improvement for modulating a high flux solar simulator designed for solar thermal and thermochemical research

Leopoldo Martínez-Manuel,[1] Manuel I. Peña-Cruz,[2,*] Carlos A. Pineda-Arellano,[2] J. Gonzalo Carrillo-Baeza,[3] and Daniel A. May-Arrioja[1]

[1]Centro de Investigaciones en Optica, A.C. Unidad Aguascalientes, Prol. Constitución 607, Fracc. Reserva Loma Bonita, CP 20200, Aguascalientes, Aguascalientes, Mexico
[2]CONACYT—Centro de Investigaciones en Optica, A.C. Unidad Aguascalientes, Prol. Constitución 607, Fracc. Reserva Loma Bonita, CP 20200 Aguascalientes, Aguascalientes, Mexico
[3]Centro de Investigación Científica de Yucatán, Unidad de Materiales, Calle 43 No. 130 x 32 y 34, Chuburná de Hidalgo, CP 97205 Mérida, Yucatán, Mexico
*Corresponding author: mipec@cio.mx

Received 6 February 2019; revised 11 March 2019; accepted 11 March 2019; posted 12 March 2019 (Doc. ID 359695); published 29 March 2019

This study presents the optical improvement of a high flux solar simulator (HFSS) with controllable flux-spot capabilities developed for researching solar thermal and thermochemical processes. The HFSS is comprised of seven 2.5 kW_{el} Xenon arc lamps coupled with ellipsoidal reflectors, a servo-controlled attenuator curtain, and three-axes linear test bench. Different attenuators were designed and tested in order to identify the best curtain geometry to improve the HFSS modulation with the lowest possible radiative losses. The optical design improvement was performed with the aid of TracePro, a Monte Carlo ray-tracing software. From simulation results, radiative peak flux from 1700 to 480 kWm^{-2} from the focal plane to 300 mm further back was estimated without curtains. By using the attenuators, flux levels from 1570 to 92 kWm^{-2} at the focal plane were also estimated. An experimental validation was achieved with a single lamp-reflector unit obtaining peak flux distributions from 200 ± 20 kWm^{-2} to 97 ± 9.7 kWm^{-2} from the focal plane to 300 mm behind. Flux modulation from 170 to 1.5 kWm^{-2} was also measured at the focal plane using a servo-controlled curtain from fully-open slats (0°) to partially closed (60°). With this attenuator, introduced as the shutter of the system, the use of several lamps or electronic rectifiers is avoided and the radiative flux is modulated with high resolution in an optomechatronical form.

https://doi.org/10.1364/AO.58.002605

1. INTRODUCTION

With the fast development of civilization, energy requirements to subsist have also increased. This has led to the excessive use of fossil fuels (oil, natural gas, coal) and consequently the gradual depletion of the ozone layer [1]. Due to this, scientists all over the world have been researching and developing technology to obtain energy from non-conventional sources like the sun [2]. With the rising price and environmental issues of fossil fuels, renewable energies have the assignment of providing clean and cost competitive energy to avoid the dependency on fossil hydrocarbon resources in the future [3]. One of the most promising technologies for the exploitation of the solar resource is concentrating solar power (CSP). This technology is based on integrated optical arrays of reflective materials, geometrically disposed for redirecting solar radiation into a smaller area; this, in order to increase the energy density of the sun and to generate a higher level of heat flux. With this environmentally friendly technology, energy is obtained to produce thermal power (electricity) and solar fuels [4]. CSP systems can incorporate technologies for thermal energy storage and backup systems [5]. These technologies provide a stable energy supply contributing for better results in energy demands, even during night and cloudy days [6,7]. This overcomes problems of hourly dependence and weather conditions, improving the plant efficiency factor.

CSP systems can be classified in the following: parabolic trough collector [8], linear Fresnel collector [9], parabolic dish collector [10], and central receiver [3,11]. All those systems own a receiver element where the solar radiation is concentrated, used to produce superheated steam, hot air [12], or to heat a work fluid like oil or molten salts [13].

Solar receivers can be catalogued as external receivers, where the absorber surface more or less equals the aperture surface, and cavity receivers, where the aperture is not identical to

1559-128X/19/102605-11 Journal © 2019 Optical Society of America

Energy 216 (2021) 119293

Contents lists available at ScienceDirect

Energy

journal homepage: www.elsevier.com/locate/energy

Numerical analysis on the optical geometrical optimization for an axial type impinging solar receiver

Leopoldo Martínez-Manuel [a], Wujun Wang [b, *], Björn Laumert [b], Manuel I. Peña-Cruz [c]

[a] Centro de Investigaciones en Óptica, A.C. Unidad Aguascalientes, Prol. Constitución 607, Fracc. Reserva Loma Bonita, CP 20200, Aguascalientes, Mexico
[b] Department of Energy Technology, KTH Royal Institute of Technology, Brinellvägen 68, 100 44, Stockholm, Sweden
[c] CONACYT - Centro de Investigaciones en Óptica, A.C. Unidad Aguascalientes, Prol. Constitución 607, Fracc. Reserva Loma Bonita, CP 20200, Aguascalientes, Mexico

ARTICLE INFO

Article history:
Received 6 August 2020
Received in revised form
14 October 2020
Accepted 9 November 2020
Available online 12 November 2020

Keywords:
Ray tracing analysis
Solar dish brayton
Impinging receiver
Cavity optimization
Concentrating solar power

ABSTRACT

Solar cavity receivers are key components in point-focus concentrating solar power technologies due to their benefits of high efficiency and operating temperature. Accordingly, the enhancement of the optical performance can yield to significant improvements in the whole thermal power system. In this study, a geometrical optimization of an axial type impinging receiver for a solar dish Brayton system was analytically accomplished through Monte Carlo ray tracing method. By modeling a reference cylindrical cavity, optical surface properties and geometrical parameters were analyzed by dividing the cavity into three zones: front wall, middle wall and back wall. Simulation results show that the light flux peaking on the cylindrical wall can be significantly reduced when the cavity front wall is modified by changing the inclination angle; the light flux distribution over the absorber surface can be flattened by increasing the cavity radius; the irradiance distribution over the absorber can be efficiently adjusted by modifying the cavity back wall. After the cavity geometry optimization, the optical efficiency of the receiver can be enhanced by 3.34%, the material volume can be reduced by 20.1% and the peak flux on the cavity wall can be reduced by 38.6%, from 30 to 18.4 kW/m^2.

Credit author statement

Leopoldo Martínez-Manuel, Methodology, Investigation, Writing - original draft, Visualization. Wujun Wang, Conceptualization, Investigation, Writing - review & editing, Supervision. Björn Laumert, Writing - review & editing, Funding acquisition, Supervision. Manuel I. Peña-Cruz, Writing - review & editing, Funding acquisition, Supervision.

1. Introduction

Concentrating solar power (CSP) is an attractive renewable technology and an important solution in the energy transition scenario that has been widely researched and promoted due to its benefits of abundance source and non-polluting characteristics [1,2].

One of the most efficient CSP systems is the solar parabolic dish, owing to its high concentration ratios (~2000); and two-axes tracking systems which can minimize the cosine losses [3,4]. A solar dish system can be applied as a heat source for decentralized power generation by integrating with thermodynamic cycles such as Brayton cycle [5], Stirling cycle [6], Rankine cycle [7,8] or combined Brayton-Rankine cycle [9]. Furthermore, modern hybrid dish Brayton systems, which can be driven by both solar energy and renewable fuel, are considered to be able to offer low cost, high efficiency rates and stable power output despite the unstable solar resource [10].

In order to improve the performances of the dish Brayton cycle, analytical and thermodynamic models have been carried out, reporting that solar conversion efficiencies can reach 21% for purely solar input systems [11], and 30% for hybrid systems [10]. These studies are conducted for systems with cavity receivers by assuming uniformly distributed absorber temperature approximately in the range of 900–1200 K. The results show that one of the key parameters in determining the receiver thermal performances is the heat transfer efficiency at the solar absorber [10–12]. Considering that these cavity receivers are the photo-thermal conversion components in the dish Bryton systems, their optical

* Corresponding author.
E-mail address: wujun@kth.se (W. Wang).

https://doi.org/10.1016/j.energy.2020.119293
0360-5442/

Sustainable Energy Technologies and Assessments

Optimization of the radiative flux uniformity of a modular solar simulator to improve solar technology qualification testing

--Manuscript Draft--

Manuscript Number:	SETA-D-20-00895R1
Article Type:	Full Length Article
Keywords:	Monte Carlo ray-tracing analysis; solar simulator; radiative flux distribution; uniformity
Corresponding Author:	Manuel I. Peña-Cruz, PhD CONACYT - Centro de Investigaciones en Optica, A.C. - Unidad Aguascalientes Aguascalientes, MEXICO
First Author:	Leopoldo Martínez-Manuel, MSc
Order of Authors:	Leopoldo Martínez-Manuel, MSc
	Wujun Wang, PhD
	Manuel I. Peña-Cruz, PhD
Abstract:	Solar simulators are key facilities for conducting solar research and certification tests under a well-controlled environment. This study presents the optical design optimization of a modular low flux solar simulator to improve solar technology qualification testing. The optical system was designed as a multi-lamp array of 26 subunits. Each subunit consists of a 575 We metal halide lamp and a parabolic reflector. The Monte Carlo ray tracing technique was used for analyzing the optical performances of the proposed design. Reflector design parameters were analyzed in detail for optimizing the uniformity of the flux distribution on the target. Results show that an average flux of 1198 W/m2 over a target area of 2000 mm×1000 mm, with a conversion efficiency of 25.7% and a sustained non-uniformity of only 1.4% was numerically achieved, predicting a Class A solar simulator for large target areas. A shutter curtain was modeled and introduced between the light source and the target for flux regulation, achieving average flux levels ranging from 1162 to 105 W/m2 with a resolution of approximately 100 W/m2. The modular nature of this design has the great advantage that it could be easily scaled according to the test requirements of potential solar systems.
Suggested Reviewers:	Aggelos Zacharopoulos, PhD Researcher a.zacharopoulos@ulster.ac.uk Solar thermal and PV application expert.
	Daniel Setrak Sowmy, PhD Researcher, Universidade de Sao Paulo Escola Politecnica danielsowmy@hotmail.com Solar simulator expert.
	Wojciech Lipinski, PhD Researcher, Australian National University wojciech.lipinski@anu.edu.au Optical devices and solar simulator expert.
Opposed Reviewers:	
Response to Reviewers:	Dear Reviewers, The authors wish to thank you for your helpful and constructive comments, which contributed greatly to improving the final version of the document. All responses are written in blue in the "response to reviewers" document. Changes in the manuscript have been marked in yellow. Sincerely, Ph. D., Manuel I. Peña-Cruz. CONACYT - Centro de Investigaciones en Óptica, A.C., Unidad Aguascalientes. Prolongación Constitución No. 607. Fracc. Reserva Loma Bonita C.P 20200.

DEVELOPMENT OF A CALORIMETRIC TEST BENCH FOR THE ASSESSMENT OF SOLAR ABSORBER COATINGS UNDER REAL OPERATING CONDITIONS

Leopoldo Martínez-Manuel[1], Nancy G. González-Canché[1], Luis B. López-Sosa[2], Jose G. Carrillo[3], Wujun Wang[4], Carlos A. Pineda-Arellano[5] and Manuel I. Peña-Cruz,[5,*]

[1] *Centro de Investigaciones en Optica, A.C. Unidad Aguascalientes, Prol. Constitución 607, Fracc. Reserva Loma Bonita, CP 20200, Aguascalientes, Aguascalientes, México*

[2] *Posgrado en ingeniería para la Sostenibilidad Energética, Universidad Intercultural Indígena de Michoacán. Carretera Pátzcuaro-Huecorio Km 3, Pátzcuaro Michoacán. C. P. 61614*

[3] *Centro de Investigación Científica de Yucatán, Unidad de Materiales, Calle 43 No. 130, Chuburná de Hidalgo, CP 97205 Mérida, Yucatán, Mexico*

[4] *Department of Energy Technology, KTH-Royal Institute of Technology, 100 44, Stockholm, Sweden*

[5] *CONACYT – Centro de Investigaciones en Optica, A.C. Unidad Aguascalientes, Prol. Constitución 607, Fracc. Reserva Loma Bonita, CP 20200 Aguascalientes, Aguascalientes, México.*

* *Corresponding author: mipec@cio.mx.*

Abstract

Solar Absorber Coatings (SACs) have been widely used for improving thermal efficiencies of solar receivers. Traditionally, these SACs have been investigated using heat treatments to test their optical-thermal properties; However, tests under concentrated flux conditions are still required. In this work, a calorimetric test bench was developed for the assessment of the flux absorption efficiency of different SACs under different levels of concentrated irradiance. The calorimetric test bench design provides the versatility to insert coated test plates as interchangeable cartridges. A High Flux Solar Simulator (HFSS) is used as the source of concentrated irradiance, providing a well-controlled laboratory environment. The test bench evaluation was conducted by quantifying the energy balance using the standard coating Pyromark®2500. Then, the heat transfer performance of 5 different SACs was assessed by replacing the absorber element of the calorimeter with: 1) Pyromark®2500, 2) Solkote®, 3) Thurmalox®250, 4) Comex® and 5) a new Soot from Forest Biomass (SFB) based coating. From the analysis, it was found that at low flux levels, all the coatings presented thermal efficiencies slightly close to each other, ranging from 91.74% to 83.24%; while at high flux levels, the efficiencies ranged from 88.69% to 72.69%, with Pyromark®2500 being the most efficient in both cases. Based on the versatility to replace the absorber element for evaluation and comparison, it is possible to conclude that the developed test bench provides a valuable tool to analyze the behavior of existing SACs under controlled flux conditions, as well as to determine the flux acceptance of new prototypes of SACs.

Keywords: Solar Absorber Coating; Calorimeter; High Flux Solar Simulator; Soot of Forest Biomass; Concentrating Solar Power.

Nomenclature

Acronyms

CPC	Compound Parabolic Collector
CSP	Concentrating Solar Power
HFSS	High Flux Solar Simulator
LFC	Linear Fresnel Collector
PTC	Parabolic Trough Collector
SFB	Soot of Biomass Forest
SAC	Solar Absorber Coating

Latin Characters

C_{pw}	Specific heat capacity of water, J/kgK
m	Mass flow rate, kg/s
Q_{abs}	Absorbed thermal power, W
Q_{in}	Incident thermal power, W
Q_{loss}	Total heat losses, W
q	Average flux distribution, W/m^2
R	Target radius, mm
S	Spectral solar irradiance, W/m^2
T_a	Ambient temperature, °C
T_i	Inlet water temperature, °C
T_o	Outlet water temperature, °C
T_s	Receiver surface temperature, °C

Greek characters

α_{abs}	Absorptivity
ΔT	Temperature difference in calorimeter, °C
ε	Emissivity
η_{abs}	Thermal absorption efficiency
$\eta_{coating}$	Coating efficiency

References

[1] Panwar NL, Kaushik SC, Surendra Kothari. Role of renewable energy sources in environmental protection: A review. Renewable and Sustainable Energy Reviews 15.3, 1513-1524, (2011).

[2] Shahzad U. The Need for Renewable Energy Sources. International Journal of Information Technology and Electrical Engineering, 4, 16-19, (2015).

[3] Khatib, Hisham. IEA world energy outlook 2011—a comment. Energy policy 48 (2012): 737-743.

[4] Shigetomi Y, Matsumoto KI, Ogawa Y, Shiraki H, Yamamoto Y, Ochi Y, Ehara T. Driving forces underlying sub-national carbon dioxide emissions within the household sector and implications for the Paris Agreement targets in Japan. Applied Energy, 228, 2321-2332, (2018).

[5] Miyamoto M, Takeuchi K. Climate agreement and technology diffusion: Impact of the Kyoto Protocol on international patent applications for renewable energy technologies. Energy Policy, 129, 1331-1338, (2019).

[6] Thirugnanasambandam M, Iniyan S, Goic R. A review of solar thermal technologies. Renewable and sustainable energy reviews, 14(1), 312-322, (2010).

[7] Kalogirou SA. Solar thermal collectors and applications. Progress in energy and combustion science, 30(3), 231-295, (2004).

[8] Duffie JA, Beckman WA. (2013). Solar engineering of thermal processes, fourth edition.

[9] Achkari O, El Fadar A. Latest developments on TES and CSP technologies–Energy and environmental issues, applications and research trends. Applied Thermal Engineering, 167, 114806, (2020).

[10] Zhang HL, Baeyens J, Degrève J, Cacères G. Concentrated solar power plants: review and design methodology. Renew. Sustain. Energy Rev. 22, 466–481, (2013).

[11] Kuravi S, Trahan J, Goswami DY, Rahman MM, Stefanakos EK. Thermal energy storage technologies and systems for concentrating solar power plants. Prog. Energy Combust. Sci. 39, 285–319, (2013).

[12] International renewable energy agency IRENA, Renewable Power Generation Costs in 2019. URL: https://www.irena.org/publications/2020/Jun/Renewable-Power-Costs-in-2019.

[13] Islam MT, Huda N, Abdullah AB, Saidur R. A comprehensive review of state-of-the-art concentrating solar power (CSP) technologies: Current status and research trends. Renewable and Sustainable Energy Reviews, 91, 987-1018, (2018).

[14] López-Herraiz M, Fernández AB, Martinez N, Gallas M. Effect of the optical properties of the coating of a concentrated solar power central receiver on its thermal efficiency. Solar Energy Materials and Solar Cells, 159, (2017), 66-72.

[15] Boubault A, Claudet B, Faugeroux O, Olalde G, Serra JJ. A numerical thermal approach to study the accelerated aging of a solar absorber material. Solar Energy 86, 3153–3167 (2012).

[16] Kuhn P, Hunt A. A new solar simulator to study high temperature solid-state reactions with highly concentrated radiation. Sol. Energy Mater. 24 (1–4), 742–750, (1991).

[17] Laaber D, Von Storch H, Wieghardt K, Fock H, Sattler C, Pitz-Pahl R. One year with synlight–Review of operating experience. In AIP Conference Proceedings (Vol. 2126, No. 1, p. 170007). AIP Publishing LLC, (2019).

[18] Vannoni C, Battisti R, Drigo S. Potential for Solar Heat in Industrial Processes. IEA SHC Task 33 (2008).

[19] Kumar L, Hasanuzzaman M, Rahim NA. Global advancement of solar thermal energy technologies for industrial process heat and its future prospects: A review. Energy Conversion and Management, 195, 885-908, (2019).

[20] Pulido-Iparraguirre D, Valenzuela L, Serrano-Aguilera JJ, Fernández-García A. Optimized design of a linear Fresnel reflector for solar process heat applications. Renewable Energy, 131, 1089-1106, (2019).

[21] Farjana SH, Huda N, Mahmud MP, Saidur R. Solar process heat in industrial systems–A global review. Renewable and Sustainable Energy Reviews, 82, 2270-2286, (2018).

[22] Zhang D, Mu S, Chan CC, Zhou GY. Optimization of renewable energy penetration in regional energy system. Energy Procedia, (2018), 152, 922-927.

[23] Jiang L, Widyolar B, Winston R. Characterization of novel mid-temperature CPC solar thermal collectors. Energy Procedia, 70, (2015), 65-70.

[24] Nandal V, Kumar R, Singh SK. Barriers identification and analysis of solar power implementation in Indian thermal power plants: An Interpretative Structural Modeling approach. Renewable and Sustainable Energy Reviews, 114, 109330, (2019).

[25] Abikoye B, Čuček L, Isafiade AJ, Kravanja Z. Integrated design for direct and indirect solar thermal utilization in low temperature industrial operations. Energy, 182, 381-396, (2019).

[26] Heffron R, Körner MF, Wagner J, Weibelzahl M, Fridgen G. Industrial demand-side flexibility: A key element of a just energy transition and industrial development. Applied Energy, 269, 115026, (2020).

[27] Tzuc OM, Bassam A, Ricalde LJ, Jaramillo OA, Flota-Bañuelos M, Soberanis MA. Environmental-economic optimization for implementation of parabolic collectors in the industrial process heat generation: Case study of Mexico. Journal of Cleaner Production, 242, (2019), 118538.

[28] Alhaj M, Mabrouk A, Al-Ghamdi SG. Energy efficient multieffect distillation powered by a solar linear Fresnel collector. Energy Convers. Manage. 171, 576–586 (2018).

[29] Petrasch J, Coray P, Meier A, Brack M, Haeberling P, Wuillemin D, Steinfeld A. A novel 50kW 11,000 suns high-flux solar simulator based on an array of xenon arc lamps, (2007).

[30] Gallo A, Marzo A, Fuentealba E, Alonso E. High flux solar simulators for concentrated solar thermal research: A review. Renew. Sustain. Energy Rev. 77, (2017), 1385–1402.

[31] Hollingsworth RT. A survey of large space chambers. 1963.

[32] Wang W, Laumert B. Simulate a ‘Sun’ for Solar Research: A literature review of solar simulator technology. Stockholm, Sweden, (2014).

[33] Tawfik M, Tonnellier X, Sansom C. Light source selection for a solar simulator for thermal applications: A review. Renewable and Sustainable Energy Reviews, 90, 802-813, (2018).

[34] Siddiqui R, Kumar R, Jha GK, Gowri G, Morampudi M, Rajput P, Lata S, Agariya S, Dubey B, Nanda G, Raghava SS. Comparison of different technologies for solar PV (Photovoltaic)

outdoor performance using indoor accelerated aging tests for long term reliability. Energy, 107, 550-561, (2016).

[35] Domínguez C, Antón I, Sala G. Solar simulator for concentrator photovoltaic systems. Optics express, 16(19), 14894-14901, (2008).

[36] Paul DI, Smyth M, Zacharopoulos A, Mondol J. The design, fabrication and indoor experimental characterisation of an isolated cell photovoltaic module. Solar Energy, 88, 1-12, (2013).

[37] Solanki SC, Dubey S, Tiwari A. Indoor simulation and testing of photovoltaic thermal (PV/T) air collectors. Applied energy, 86(11), 2421-2428, (2009).

[38] Kenny SP, Davidson JH. Design of a multiple-lamp largescale solar simulator," J. Solar Energy Eng. 116, 200–205, (1994).

[39] Zacharopoulos A, Mondol JD, Smyth M, Hyde T, O'Brien V. State of the art solar simulator with flexible mounting. In ISES Solar World Congress (pp. 854-863), (2009).

[40] Sowmy DS, Ara PJS, Prado RT. Uncertainties associated with solar collector efficiency test using an artificial solar simulator. Renewable Energy, 108, 644-651, (2017).

[41] Hirsch D, Zedtwitz PV, Osinga T, Kinamore J, Steinfeld A. A new 75 kW high-flux solar simulator for high-temperature thermal and thermochemical research. J. Sol. Energy Eng. 125 (1), 117–120, (2003).

[42] Zahedi A. Review of modelling details in relation to low-concentration solar concentrating photovoltaic. Renewable and Sustainable Energy Reviews, 15(3), 1609-1614, (2011).

[43] Sarwar J, Georgakis G, LaChance R, Ozalp N. Description and characterization of an adjustable flux solar simulator for solar thermal, thermochemical and photovoltaic applications. Solar Energy, 100, 179-194, (2014).

[44] Pravettoni M, Galleano R, Dunlop ED, Kenny RP. Characterization of a pulsed solar simulator for concentrator photovoltaic cell calibration. Measurement science and technology, 21(11), 115901, (2010).

[45] Nakakura M, Ohtake M, Matsubara K, Yoshida K, Cho HS, Kodama T, Gokon N. Development of a receiver evaluation system using 30 kWth point concentration solar simulator. Energy Procedia, 69, 497-505, (2015).

[46] Li J, Gonzalez-Aguilar J, Romero M. Line-concentrating flux analysis of 42kWe high-flux solar simulator. Energy procedia, 69, 132-137, (2015).

[47] Okuhara Y, Kuroyama T, Tsutsui T, Noritake K, Aoshima T. A solar simulator for the measurement of heat collection efficiency of parabolic trough receivers. Energy Procedia, 69, 1911-1920, (2015).

[48] Alxneit I, Dibowski G. R12. 5 Solar Simulator Evaluation Report-Project SFERA. vol. Project SF, 1-36, (2011).

[49] Bader R, Haussener S, Lipiński W. Optical design of multisource high-flux solar simulators. J. Sol. Energy Eng. 137 (2) 021012_1-021012_9, (2015).

[50] Levêque G, Bader R, Lipiński W, Haussener S. Experimental and numerical characterization of a new 45 kW el multisource high-flux solar simulator. Opt. Express 24 (22), (2016), 1360–1373.

[51] Esen V, Sağlam Ş, Oral B. Light sources of solar simulators for photovoltaic devices: A review. Renewable and Sustainable Energy Reviews, 77, 1240-1250, (2017).

[52] Tawfik M, Tonnellier X, Sansom C. Light source selection for a solar simulator for thermal applications: A review. Renewable and Sustainable Energy Reviews, 90, 802-813, (2018).

[52] Ekman BM, Brooks G, Rhamdhani, MA. Development of high flux solar simulator for solar thermal research. Sol Energy Mater Sol Cells, 141:436–46, (2015).

[53] Dong X, Sun Z, Nathan GJ, Ashman PJ, Gu D. Time-resolved spectra of solar simulators employing metal halide and xenon arc lamps. Solar Energy, 115, 613-620, (2015).

[54] Siegel NP, Roba JP. Design, Modeling, and Characterization of a 10 kWe Metal Halide High Flux Solar Simulator. Journal of Solar Energy Engineering, 140(4), (2018).

[55] Meng Q, Wang Y, Zhang L. Irradiance characteristics and optimization design of a large-scale solar simulator. Solar Energy, 85(9), 1758-1767, (2011).

[56] Wang W, Aichmayer L, Garrido J, Laumert B. Development of a Fresnel lens based high-flux solar simulator. Sol. Energy 144, 436–444, (2017).

[57] Li L, Wang B, Pottas J, Lipiński W. Design of a compound parabolic concentrator for a multi-source high-flux solar simulator. Solar Energy, 183, 805-811, (2019).

[58] Song J, Wang J, Niu Y, Wang W, Tong K, Yu H, Yang Y. Flexible high flux solar simulator based on optical fiber bundles. Solar Energy, 193, 576-583, (2019).

[59] Modest MF, Radiative heat transfer (Academic press, 2013).

[60] Delatorre J, Baud G, Bézian JJ, Blanco S, Caliot C, Cornet JF, Coustet C, Dauchet J, El Hafi M, Eymet V, Fournier R, Gautrais J, Gourmel O, Joseph D, Meilhac N, Pajot A, Paulin M, Perez P, Piaud B, Roger M, Rolland J, Veynandt F, Weitz S. Monte Carlo advances and concentrated solar applications. Solar Energy, 103, 653-681, (2014).

[61] Steinfeld A. Exchange factor between two spheres placed at the foci of a specularly reflecting ellipsoidal cavity. Int. Commun. Heat Mass Transfer 18 (1), 19–26, (1991).

[62] Petrasch JR. A free and open source Monte Carlo ray tracing program for concentrating solar energy research. In Energy Sustainability (Vol. 43956, pp. 125-132), (2010).

[63] Krueger KR, Davidson JH, Lipiński W. Design of a new 45 kWe high-flux solar simulator for high-temperature solar thermal and thermochemical research. Journal of solar energy engineering, 133(1), (2011).

[64] Xu J, Tang C, Cheng Y, Li Z, Cao H, Yu X, Li Y, Wang Y. Design, construction, and characterization of an adjustable 70 kW high-flux solar simulator. Journal of solar energy engineering, 138(4), (2016).

[65] Xiao J, Wei X, Gilaber RN, Zhang Y, Li Z. Design and characterization of a high-flux non-coaxial concentrating solar simulator. Applied Thermal Engineering, 145, 201-211, (2018).

[66] Röger M, Herrmann P, Ulmer S, Ebert M, Prahl C, Göhring F. Techniques to measure solar flux density distribution on large-scale receivers. Journal of Solar Energy Engineering, 136(3), (2014).

[67] Ballestrín J, Rodríguez-Alonso M, Rodriguez J, Canadas I, Barbero FJ, Langley LW, Barnes A. Calibration of high-heat-flux sensors in a solar furnace. Metrologia, 43(6), 495, (2006).

[68] Zhu Q, Xuan Y, Liu X, Yang L, Lian W, Zhang J. A 130 kWe solar simulator with tunable ultra-high flux and characterization using direct multiple lamps mapping. Applied Energy, 270, 115165, (2020).

[69] Dai S, Chang Z, Ma T, Wang L, Li X. Experimental study on flux mapping for a novel 84 kWe high flux solar simulator. Applied Thermal Engineering, 162, 114319, (2019).

[70] Ho CK, Khalsa SS. A photographic flux mapping method for concentrating solar collectors and receivers. Journal of solar energy engineering, 134(4), (2012).

[71] Xiao J, Yang H, Wei X, Li Z. A novel flux mapping system for high-flux solar simulators based on the indirect method. Solar Energy, 179, 89-98, (2019).

[72] Abuseada M, Ophoff C, Ozalp N. Characterization of a new 10 kWe high flux solar simulator via indirect radiation mapping technique. Journal of Solar Energy Engineering, 141(2), (2019).

[73] Codd DS, Carlson A, Rees J, Slocum AH. A low cost high flux solar simulator. Sol. Energy 84 (12), 2202–2212, (2010).

[74] Gill R, Bush E, Haueter P, Loutzenhiser P. Characterization of a 6 kW high-flux solar simulator with an array of xenon arc lamps capable of concentrations of nearly 5000 suns. Rev. Sci. Instrum. 86 (12) 125107_1-125107_8, (2015).

[75] Pozzobon V, Salvador S. High heat flux mapping using infrared images processed by inverse methods: an application to solar concentrating systems. Solar Energy, 117, 29-35, (2015).

[76] Galiullin T, Gobereit B, Naumenko D, Buck R, Amsbeck L, Neises-von Puttkamer M, Quadakkers WJ. High temperature oxidation and erosion of candidate materials for particle receivers of concentrated solar power tower systems. Solar Energy, 188, 883-889, (2019).

[77] Kalogirou SA. Solar energy engineering: processes and systems. Academic Press. 2013.

[78] Kennedy E. Review of mid to high temperature solar selective absorber materials, NREL/TP-520-31267, Golden, CO: National Renewable Energy Laboratory (2002).

[79] Zhang K, Hao L, Du M, Mi J, Wang JN, Meng JP. A review on thermal stability and high temperature induced ageing mechanisms of solar absorber coatings. Renewable and Sustainable Energy Reviews, 67, 1282-1299, (2017).

[80] Xu K, Du M, Hao L, Mi J, Yu Q, Li S. A review of high-temperature selective absorbing coatings for solar thermal applications. Journal of Materiomics, 6(1), 167-182, (2020).

[81] TiNOX®. http://www.almecogroup.com/

[82] Tesfamicael T. Characterization of selective solar absorbers. PhD, Uppsala University, Uppsala, Sweden, 2000.

[83] Ho CK, Mahoney AR, Ambrosini A, Bencomo M, Hall A, Lambert TN. Characterization of Pyromark 2500 paint for high-temperature solar receivers. Journal of Solar Energy Engineering, 136(1) (2014).

[84] Karami M, Akhavan MA, Bahabadi S, Delfani, Ghozatloo A. A new application of carbon nanotubes nanofluid as working fluid of low-temperature direct absorption solar collector. Solar Energy Materials and Solar Cells 121, (2014): 114-118.

[85] Jamil MM, Sidik NAC, Umar US, Hamisu MT, Sa'ad A. Carbon Nanotube for Solar Energy Applications: A Review. Journal of Advanced Research in Fluid Mechanics and Thermal Sciences, 56, 233-247, (2019).

[86] Alami AH, Aokal K. Enhancement of spectral absorption of solar thermal collectors by bulk graphene addition via high-pressure graphite blasting. Energy conversion and management, 156, (2018), 757-764.

[87] López-Sosa LB, González-Avilés M, Hernández-Ramírez M, Medina-Flores A, Santos-Ramos I, Zárate-Medina J. Electron microscopy characterization of forest biomass soot as solar energy absorption material. Microscopy and Microanalysis, 25(S2), 2234-2235, (2019).

[88] López-Sosa LB, González-Avilés M, Hernández-Ramírez LM, Medina-Flores A, López-Luke T, Bravo-Sánchez M, Zárate-Medina J. Ecological solar absorber coating: A proposal for the use of residual biomass and recycled materials for energy conversion. Solar Energy, 202, (2020), 238-248.

[89] Abdelkader TK, Zhang Y, Gaballah ES, Wang S, Wan Q, Fan Q. Energy and exergy analysis of a flat-plate solar air heater coated with carbon nanotubes and cupric oxide nanoparticles embedded in black paint. Journal of Cleaner Production, 250, (2019), 119501.

[90] Zheng L, Zhou F, Zhou Z, Song X, Dong G, Wang M, Diao X. Angular solar absorptance and thermal stability of Mo–SiO2 double cermet solar selective absorber coating. Solar Energy 115 (2015): 341-346.

[91] Al-Rjoub A, Rebouta L, Costa P, Vieira LG. Multi-layer solar selective absorber coatings based on W/WSiAlNx/WSiAlOyNx/SiAlOx for high temperature applications. Solar Energy Materials and Solar Cells 186 (2018): 300-308.

[92] Gao XH, Guo ZM, Geng QF, Ma PJ, Liu G. Structure, optical properties and thermal stability of TiC-based tandem spectrally selective solar absorber coating. Solar Energy Materials and Solar Cells 157 (2016): 543-549.

[93] Wang XJ, Jiang LJ, Du M, Hao L, Liu XP, Yu QH. The degradation of solar thermal absorption coatings. Energy Procedia, 49, (2014), 1747-1755.

[94] Reoyo-Prats R, Plaza AC, Faugeroux O, Claudet B, Soum-Glaude A, Hildebrandt C, Binyamin C, Agüero A, Meißner T. Accelerated aging of absorber coatings for CSP receivers under real high solar flux–evolution of their optical properties. Solar Energy Materials and Solar Cells, 193, (2019), 92-100.

[95] Boubault A, Ho CK, Hall A, Lambert TN, Ambrosini A. Durability of solar absorber coatings and their cost-effectiveness. Solar Energy Materials and Solar Cells, 166, 176-184, (2017).

[96] López-Martín R, Valenzuela L. Optical efficiency measurement of solar receiver tubes: a testbed and case studies. Case Stud. Therm. Eng. 12, 414–422 (2018).

[97] Estrada CA, Jaramillo OA, Acosta R, Arancibia-Bulnes CA. Heat transfer analysis in a calorimeter for concentrated solar radiation measurements. Solar energy 81.10 (2007): 1306-1313.

[98] Cobble MH. Heat exchangers for solar concentrators. Solar Energy, 7(1), (1963), 18-21.

[99] Cobble MH. Circular flat plate heat exchanger for solar concentrator. Solar Energy, 6(4), (1962), 164-167.

[100] Groer U, Neumann A. Development and test of a high flux calorimeter at DLR Cologne. Le Journal de Physique IV 9.PR3 (1999): Pr3-643.

[101] Pérez-Rábago CA, Marcos MJ, Romero M, Estrada CA. Heat transfer in a conical cavity calorimeter for measuring thermal power of a point focus concentrator. Solar Energy, 80(11), (2006), 1434-1442.

[102] Jaramillo OA, Perez-Rabago, CA, Arancibia-Bulnes CA, Estrada CA. A flat-plate calorimeter for concentrated solar flux evaluation. Renewable Energy, 33(10), (2008), 2322-2328.

[103] Kretzschmar H, Gauche P, Mouzouris M. Development of a flat-plate calorimeter for a small-scale heliostat field. SolarPaces, Marrakech, Morocco (2012): 11-14.

[104] Verma RN, Kumar R, Dixit A, Chandra L. A low temperature water-cooled radiation calorimeter for estimation of concentrated solar irradiance. Solar Energy 167 (2018): 194-209.

[105] Jafrancesco D, Cardoso JP, Mutuberria A, Leonardi E, Les I, Sansoni P, Francini F, Fontani D. Optical simulation of a central receiver system: Comparison of different software tools. Renewable and Sustainable Energy Reviews, 94, 792-803, (2018).

[106] Lambda Research Corporation, TracePro User's Manual: https://www.lambdares.com/wp-content/uploads/TraceProDownload/TracePro_User_Manual.pdf.

[107] Klette R, Kozera R, Schlüns K. Reflectance-Based Shape Recovery. in Handbook of Computer Vision and Applications, B. Jähne, H. Haußecker and P. Geißler editors, vol. 2 (Signal processing and Pattern Recognition), ch. 19, Acad. Press, San Diego, (1999).

[108] Krueger KR. Design and Characterization of a Concentrating Solar Simulator. University of Minnesota. 2012.

[109] Heat flux Gardon type radiometer: http://www.vatell.com/node/4

[110] Ballestrin J, Ulmer S, Morales A, Barnes A, Langley LW, Rodrıguez M. Systematic error in the measurement of very high solar irradiance. Solar energy materials and solar cells, 80(3), (2003), 375-381.

[111] Guillot E, Alxneit I, Ballestrin J, Sans JL, Willsh C. Comparison of 3 heat flux gauges and a water calorimeter for concentrated solar irradiance measurement. Energy Procedia, 49, (2014), 2090-2099.

[112] "Commercial white matte paint," https://www.comex.com.mx/getattachment/94344e52-eb00-47ca-bae9-b688a25dbae2/.aspx/.

[113] Abuseada, M. An Experimental and Numerical Study on the Heat Transfer Driven Dynamics and Control of Transient Variations in a Solar Reactor. 2019.

[114] Ulmer S, Reinalter W, Heller P, Lüpfert E, Martínez D. Beam characterization and improvement with a flux mapping system for dish concentrators. J. Sol. Energy Eng., 124(2), 182-188, (2002).

[115] Hughes I, Hase T. Measurements and their uncertainties: a practical guide to modern error analysis. Oxford University Press (2010).

[116] Commercial black paint Comex, https://www.comex.com.mx/getattachment/94344e52-eb00-47ca-bae9-b688a25dbae2/.aspx/.

[117] Xenon-acr lamp: http://www.centurylamp.net.cn/company_profile.html.

[118] Sarwar J, Shrouf T, Kakosimos KE. Characterization of thermal performance and optical properties of a material under concentrated radiation using a high flux solar simulator. In AIP Conference Proceedings (Vol. 1850, No. 1, p. 160025). AIP Publishing LLC, (2017).

[119] Cermax, "Xenon lamp engineering guide," http://www.excelitas.com/Downloads/Cermax_Eng_Guide.pdf.

[120] Chang YN, Yang TH, Chan SY, Cheng HL. Design of electronic ballast for short-arc xenon lamps. In 2012 IEEE International Symposium on Industrial Electronics (pp. 309-314). IEEE, (2012).

[121] Chan SY, Yang TH, Chang YN. Design of electronic ballast for short-arc xenon lamp with interleaved half-wave rectifier. IEEE Transactions on Power Electronics, 31(7), 5102-5112, (2015).

[122] Gokon N, Takahashi S, Yamamoto H, Kodama T. Thermochemical two-step water-splitting reactor with internally circulating fluidized bed for thermal reduction of ferrite particles. International Journal of Hydrogen Energy, 33(9), 2189-2199, (2008).

[123] Simon M, Meyer EL. Detection and analysis of hot-spot formation in solar cells. Solar Energy Materials and Solar Cells, 94(2), 106-113, (2010).

[124] Ho CK, Mahoney AR, Ambrosini A, Bencomo M, Hall A, Lambert TN. Characterization of Pyromark 2500 for high-temperature solar receivers. In Energy Sustainability (Vol. 44816, pp. 509-518). American Society of Mechanical Engineers. Vol. 44816 (2012), pp. 509-518.

[125] Selective coating Solkote: https://www.solec.org/solkote/solkote-technical-specifications/

[126] Andemeskel A, Suriwong T, Wamae W. Effects of Aluminum Fin Thickness Coated with a Solar Paint on the Thermal Performance of Evacuated Tube Collector. Energy Procedia, 138, (2017), 429-434.

[127] Thurmalox250: http://www.dampney.com/Product-Line/AT/View/PID/2/Thurmalox-250

[128] Sanchez M, Mateu E, Perez D, García P, Villuendas F, Heras C, Alonso R. Optical and thermal characterization of solar receivers for parabolic trough collectors. In Advances in Science and Technology (Vol. 74, pp. 313-319). Trans Tech Publications Ltd, (2010).

[129] Farzaneh A, Mohammadi M, Ahmad Z, Ahmad I. Aluminium Alloys in Solar Power–Benefits and Limitations. INTECH Open Access Publisher; 2013.

[130] Wang F, Shuai Y, Yuan Y, Liu B. Effects of material selection on the thermal stresses of tube receiver under concentrated solar irradiation. Materials & Design, 33, (2012), 284-291.

[131] ASM International. Handbook Committee (Ed.). Properties and selection: nonferrous alloys and special-purpose materials (Vol. 2). Asm Intl. (1990).

[132] Rivera DL, Montoya PR, Zapata MAT, Ordóñez KV, Castrillón LJR, Salazar YV, Carmona MER. Tratamiento de residuos de poliestireno expandido utilizando solventes verdes. Revista Investigaciones Aplicadas 8 (1), (2014), 1–9.

[133] Jimenez-Francisco M, Caamal-Canche JA, Carrillo JG, Cruz-Estrada RH. Performance assessment of a composite material based on kraft paper and a resin formulated with expanded

polystyrene waste: a case study from Mexico. Journal of Polymers and the Environment, 26(4), (2018), 1573-1580.

[134] Standard Tables for Reference Solar Spectral Irradiances: Direct Normal and Hemispherical on 37° Tilted Surface. Designation: G 173 – 03.

[135] Bond TC, Bergstrom RW. Light absorption by carbonaceous particles: An investigative review. Aerosol science and technology, 40(1), (2006), 27-67.

[136] Lovegrove K, Stein W. Concentrating solar power technology: principles, developments and applications. Elsevier, 2012.

[137] Liu J, Lei D, Li Q. Vacuum lifetime and residual gas analysis of parabolic trough receiver. Renewable energy, 86, (2016), 949-954.

[138] Moss RW, Henshall P, Arya F, Shire GSF, Hyde T, Eames PC. Performance and operational effectiveness of evacuated flat plate solar collectors compared with conventional thermal, PVT and PV panels. Applied energy, 216, 588-601, (2018).

[139] Garrido J, Aichmayer L, Wang W, Laumert B. Characterization of the KTH high-flux solar simulator combining three measurement methods. Energy, 141, (2017), 2091-2099.

[140] Bellos E, Mathioulakis E, Tzivanidis C, Belessiotis V, Antonopoulos KA. Experimental and numerical investigation of a linear Fresnel solar collector with flat plate receiver. Energy Conversion and Management, 130, (2016), 44-59.

[141] Cindrella L. The real utility ranges of the solar selective coatings. Solar Energy Materials and Solar Cells, 91(20), 1898-1901, (2007).

[142] Ambrosini A, Boubault A, Ho CK, Banh L, Lewis JR. Influence of application parameters on stability of Pyromark® 2500 receiver coatings. In AIP Conference Proceedings (Vol. 2126, No. 1, p. 030002). AIP Publishing LLC, (2019).

[143] Steinfeld A, Palumbo R. Solar thermochemical process technology. Encyclopedia of physical science and technology, 15(1), 237-56, (2001).

[144] Fletcher EA. Solarthermal processing: a review. J. Sol. Energy Eng., 123(2), 63-74, (2001).

[145] Yousif E, Haddad R. Photodegradation and photostabilization of polymers, especially polystyrene. SpringerPlus, 2(1), (2013), 398.